The effect of grain boundaries on the fracture toughness of hard coatings

Zur Erlangung des akademischen Grades einer

DOKTORIN DER INGENIEURWISSENSCHAFTEN (Dr.-Ing.)

von der KIT-Fakultät für Maschinenbau des

Karlsruher Instituts für Technologie (KIT)

angenommene

DISSERTATION

von

M.Eng. Yinxia Zhang
aus Anhui, China

Tag der mündlichen Prüfung:	30. März 2026
Referent:	Prof. Christoph Kirchlechner
Korreferentin:	Prof. Nina Schalk

Affidavit

I, Yinxia Zhang,

declare that I have written this thesis myself,

i.e. without the help of 3rd parties and without using any sources or aids other than those indicated.

I have indicated all passages taken from other sources,

including artificial intelligence, either in word or meaning.

This also applies to all illustrations.

Date: 30.03.2026

Name: Yinxia Zhang

Abstract

Hard coatings are widely used under mechanical and thermal loading, where their fracture toughness is crucial for reliable performance. Grain boundaries (GBs) formed during deposition often act as preferred sites for crack initiation and propagation, making their influence on fracture toughness a key factor in coating reliability. To systematically quantify this effect, further development of *in situ* bridge notch micro-cantilever fracture testing is required.

First, a micro-cantilever with a very thin bridge notch was prepared by focused ion beam (FIB) on two coatings. A rigid loading setup with high resolution and an *in situ* scanning electron microscope (SEM) were employed to observe the bridge failure, which is widely assumed and predicted by the finite element method (FEM), and to determine whether FIB-induced artifacts were mitigated by promoting the formation of a sharp natural crack after bridge failure.

Based on this developed methodology, the influence of GBs on the fracture toughness of nitride hard coatings was systematically investigated under various conditions, including the presence and orientation of GBs at ambient temperature as well as the role of GBs at elevated temperatures. First, to explore the impact of GB presence, a tailored hard coating was prepared, comprising a columnar-grained layer with GBs and an epitaxial layer without GBs. Second, to study the effect of GB orientation, micro-cantilevers were prepared from columnar-grained nitride coatings with notches oriented parallel or perpendicular to the growth direction of the coating. Third, the role of GBs at elevated temperatures was investigated by testing a series of bridge notch micro-cantilevers *in situ* SEM between 25 °C and 600 °C. Furthermore, the effects of the annealing state of the coating and the Ga ions induced by FIB on fracture toughness were studied by post-mortem analysis.

The *in situ* SEM indenter with high stiffness and low-load noise enabled the first experimental observation of bridge notch failure and crack arrest occurring before the fatal fracture of the newly formed through-thickness main notch. As a result, up to three corresponding fracture toughness values could be obtained from a single test, significantly reducing data scatter. For the observation of bridge failure before the final fracture, an optimal bridge geometry was recommended.

This systematic investigation demonstrated that GBs significantly influence the fracture toughness of hard coatings at both ambient and elevated temperatures. The presence of GB leads to a significant reduction in fracture toughness, with a decrease of approximately 30% when comparing columnar-grained to epitaxial microstructures. In addition, GB orientation influences the fracture behavior. When the load was applied perpendicularly to the growth direction of the columnar grains, a continuous crack deflection was observed, increasing in fracture toughness by about 8%, compared with the parallel test. At elevated temperatures, the fracture toughness decreased with increasing temperature. The greater the number of coating surfaces exposed to vacuum, the greater the reduction in fracture toughness, whereas Ga ions introduced during FIB milling exhibited a negligible effect after annealing. GBs are known to act as diffusion pathways that promote oxidation and void formation, which reduce the effective load-bearing area and introduce stress concentrations, thereby decreasing the fracture toughness of annealed coatings.

Kurzfassung

Hartstoffschichten werden häufig unter mechanischer und thermischer Belastung eingesetzt, wo ihre Bruchzähigkeit für eine zuverlässige Leistung entscheidend ist. Während der Abscheidung gebildete Korngrenzen (KG) sind oft bevorzugte Stellen für Rissbildung und -ausbreitung, wodurch sie ein Schlüsselfaktor für die Zuverlässigkeit sind. Um diesen Effekt systematisch zu quantifizieren, ist eine Weiterentwicklung der *in situ* Brückenkerb-Mikrokantilever-Bruchprüfung erforderlich.*

Eine starre Belastungsanordnung mit hoher Auflösung und ein *in situ* Rasterelektronenmikroskop (REM) wurden eingesetzt, um das allgemein angenommene und vorhergesagte Versagen der Brücke zu beobachten und um festzustellen, ob Artefakte des fokussierten Ionenstrahls (FIB) durch die Förderung der Bildung eines natürlichen Risses gemildert wurden. Auf der Grundlage dieser entwickelten Methodik wurde der Einfluss von kolumnare KG auf die Bruchzähigkeit von Nitrid-Hartstoffschichten systematisch untersucht. Um zunächst den Einfluss des Vorhandenseins von KG zu untersuchen, wurde eine maßgeschneiderte hergestellt, die aus einer Schicht mit KG und einer epitaktischen Schicht ohne KG bestand. Um den Einfluss der KG-Orientierung zu untersuchen, wurden Mikrobiegebalken aus Nitridbeschichtungen mit Kerben hergestellt, die parallel oder senkrecht zur Wachstumsrichtung der Beschichtung ausgerichtet waren. Drittens wurde die Rolle von KG bei erhöhten Temperaturen zwischen 25 °C und 600 °C untersucht. Darüber hinaus wurden die Auswirkungen des Glühzustands der Beschichtung und der durch FIB induzierten Ga-Ionen durch eine post-mortem-Analyse untersucht.*

Diese Arbeit präsentierte die erste experimentelle Beobachtung von Versagen in der Brückenzone und Rissstop-verhalten, die vor dem fatalen Bruch der neu gebildeten Hauptkerbe auftraten. Dadurch konnten bis zu drei entsprechende Bruchzähigkeitswerte aus einem einzigen Test gewonnen werden, was die Datenstreuung erheblich reduzierte. Das Vorhandensein von KG führt zu einer deutlichen Verringerung der Bruchzähigkeit mit einem Rückgang von etwa 30 % im Vergleich zu säulenförmigen Mikrostrukturen und epitaktischen Mikrostrukturen. Darüber hinaus wurde bei senkrechter Belastung zur Wachstumsrichtung der säulenförmigen Körner eine kontinuierliche Rissablenkung beobachtet, wodurch die Bruchzähigkeit im Vergleich zum parallelen Test um etwa 8 % zunahm. Bei erhöhten Temperaturen nahm die Bruchzähigkeit mit steigender Temperatur ab. Je größer die Anzahl der dem Vakuum ausgesetzten Schichtoberflächen war, desto größer war die Verringerung der Bruchzähigkeit. KG wirken bekanntermaßen als Diffusionswege, die die Oxidation und die Bildung von Hohlräumen fördern, wodurch die effektive Tragfläche verringert und Spannungskonzentrationen eingeführt werden, was wiederum die Bruchzähigkeit von Beschichtungen nach der Wärmebehandlung verringert. Diese systematische Untersuchung zeigte, dass KG die Bruchzähigkeit von Hartstoffschichten sowohl bei Umgebungstemperatur als auch bei erhöhten Temperaturen erheblich beeinflussen.*

*AI-assisted translation, see Appendix 8.4 for documentation of prompts.

Acknowledgement

Firstly, I would like to express my sincere thanks to my main supervisor, Prof. Christoph Kirchlechner, for giving me the invaluable opportunity to pursue my academic studies. He has provided a lot of academic training, continuous guidance, and patient discussion on experimental design. In addition, he offered me many opportunities to participate in international academic conferences. He has also shown great care and consideration in my personal life. In particular, during my pregnancy and the period of after childbirth, he demonstrated exceptional understanding, patience, and support. He is an open-minded professor with an international vision. I am sincerely grateful for the chance to join such an international research group with members from diverse backgrounds around the world. I would also like to thank Prof. Nina Schalk for agreeing to be my second supervisor during the defense and for the valuable guidance in this thesis.

The *in situ* microscopy group is a highly international group, which is full of inspiring discussions and positive energy. I deeply appreciate Dr. Subin Lee, as the group leader, for his selfless guidance and support. This includes, but is not limited to, the training of experimental equipment, experimental discussion, analysis of testing results, and academic writing. I would like to thank Ass. Prof. Hariprasad Gopalan and Dr. Eloho Okotete for their initial experimental support, which enabled me to quickly start my research. I am also grateful to Dr. Viswanadh Arigela, Dr. Li Juan, and Dr. Eloho Okotete for helping me quickly adapt to daily life at KIT. I sincerely thank Dr. Camila Aguiar Teixeira and Dr. Divya Sri Bandla for their support during nanoindenter experiments, and I truly enjoyed the time we shared. I also thank Dr. Ujjval Bansal for his assistance with TEM characterization and analysis. I wish to thank Angelica Maria Medina Gomez, Konrad Prikoszovich, Ved Gumaste, Dr. Ashwini Kumar Mishra, and Dr. habil. Xufei Fang for their valuable scientific discussions and help in daily life. I would like to thank Dr. Patric Gruber, Edmund Böck, Daniela Exner, Rolf Rolli for their help in the laboratory. I am grateful again to all colleagues in IAM-MMI for their support and help.

I gratefully acknowledge financial support from the Austrian Science Fund (FWF) [I4720] and the German Research Foundation (DFG) [436506789] within the framework of the DACH program. I also acknowledge support from the Helmholtz Program Materials Systems Engineering and the Robert Bosch Foundation, as well as the Karlsruhe Nano Micro Facility (KNMFi) for support and access to TEM facilities. I would especially like to thank my two project collaborators, Dr. Matthias Bartosik and PD Dr. Steffen Brinckmann, for their prompt support and highly productive scientific discussions throughout the project.

I would also like to thank my family. The following section is written in Chinese, so that my feelings can be expressed to them in a more direct and heartfelt way.

江月年年望相似，人生代代无穷尽。如今，生命的轮回落在我与父母之间，也延展至我与孩子之间。感谢父母给予我一颗自由而坚定的心，使我得以畅游天地之广阔，仰观宇宙之浩瀚，于异国他乡探索科学的边界。感谢我最心爱的宝贝 Anton，让我真切体会到生命的珍贵，给予我无尽的欢喜与炽热的爱，愿他此生平安、喜乐常在。感谢我的爱人

龚庆，与我一同坐看云起云落，在生活中给予细致的呵护，在事业上给予始终如一的支持与理解。亦感念自己何其幸运，得以生活在和平的国度。感谢人生旅途中所有亲朋好友的陪伴、支持与帮助。

Content

List of Figures

List of Tables

List of abbreviations

AlN	Aluminum nitride
CrN	Chromium nitride
CrN/AlN multilayer	Multilayer structure composed of alternating CrN and AlN layers
cg	Columnar grain
DCB	Double cantilever beam
DSC	Differential scanning calorimetry
DTA	Differential thermal analysis
EDS	Energy-dispersive X-ray spectroscopy
EELS	Electron energy loss spectroscopy
epi	Epitaxy
FEM	Finite element method
FIB	Focused ion beam
GB	Grain boundary
GBs	Grain boundaries
HAADF	High angle annular dark field
HIM	Helium ion microscope
HT	High temperature
LEFM	Linear Elastic Fracture Mechanics
PVD	Physical vapor deposition
RT	Room temperature
SEM	Scanning electron microscope
STEM	Scanning transmission electron microscope
TEM	Transmission electron microscope
TGA	Thermo-gravimetric analysis
XRD	X-ray diffraction
∥-notch	loading parallel to the coating growth direction
⊥-notch	loading perpendicular to the growth direction

List of notations

a	Notch depth/crack length
b	Bridge width
B	Beam width
c	Average crack length
d	Half width of double cantilever
E	Elastic modulus
E_s	Elastic modulus of substrate
E_v	Vacancy formation energy
$f(a/W)$	Geometry correction factor
f_{corr}	Bridge geometry correction factor
$f_{ij}(\theta)$	Angular-dependent dimensionless term
F_B	Load at bridge failure
F_{B1}	Load at bridge-1 failure
F_{B2}	Load at bridge-2 failure
F_C	Load at final fracture
F_{max}	Maximum load
G	Energy release rate
G_c	Critical energy release rate
h	Beam hight of double cantilever
H	Hardness of material
k_B	Boltzmann constant
K	Stress intensity factor
K_C	Critical stress intensity factor
K_I	Stress intensity factor at mode I
$K_{(I,II,III)}$	Stress intensity factor at mode I, II, III
K_{IC}	Critical stress intensity factor at mode I
K_{IC}^*	Bridge notch fracture toughness at mode I
K_{IC}^*-B_R	Right bridge notch fracture toughness at mode I
K_{IC}^*-B_L	Left bridge notch fracture toughness at mode I
$K_{IQ,\ ref}$	Conditional fracture toughness at mode I
$K_{IQ,\ ref;\ C}$	Conditional fracture toughness at mode I from final fracture
$K_{IQ,\ ref;\ B}$	Conditional fracture toughness at mode I from bridge failure
L	Free cantilever length
n	Number of vacancies
N	Number of atoms
pN_2	Partial nitrogen pressure
pO_2	Partial oxygen pressure
r	Distance from the crack tip
R	Gas constant
R_p	Radius of pillar
R_c	Radius of curvature

t	Sample thickness
t_f	Film thickness
t_s	Substrate thickness
T	Absolute temperature
μ	Coefficient of friction between the punch and the sample
v_s	Poisson's ratio of the substrate
w	Beam width of double cantilever
W	Beam thickness
Y	Dimensionless constant depending on geometry and loading mode
α	Coefficient related to the indenter geometry
θ	Angle from the crack
σ	Fracture stress
σ_f	Residual stress of in the film
σ_{ij}	Stress tensor
σ_{YS}	Yield strength of the material
γ	Coefficient related to crack, indenter geometry and material properties
γ_p	Plastic work per unit area of surface created
γ_s	Surface energy
ΔG	Gibbs free energy changes
ΔG^0	Standard Gibbs free energy changes

1 Introduction

1.1 Motivation

Hard coatings composed of oxides, nitrides, and carbides exhibit significant advantages in terms of hardness, wear resistance, and thermal stability compared to uncoated substrate[1-4]. Consequently, these coatings are widely utilized in industrial applications, such as cutting tools, aerospace protective layers, and automotive components [5-8]. Hard coatings fabricated via deposition typically exhibit submicron columnar grain structures with high-density grain boundaries [9-11]. These grain boundaries are susceptible to serving as sites for crack initiation and propagation, diminishing the overall fracture toughness of the coating and inducing anisotropy in its fracture toughness. Furthermore, hard coatings are often subjected to thermal and mechanical stresses [12-16]. The durability of these coatings directly influences the operational lifespan of the components. However, determining and optimizing the fracture toughness of coatings is highly challenging due to their micron-scale thickness, which renders traditional mechanical testing methods (such as compact tension specimens) inapplicable [17]. This inherent difficulty is further exacerbated when attempting to systematically investigate the influence of grain boundary defects on fracture toughness at both ambient and elevated temperatures.

Currently, there is a lack of standardization of micro-scale fracture toughness measurement techniques [18], since the small sample size complicates sample preparation [19]. In recent years, various methodologies have been develop to measure fracture toughness at the micro-scale, such as nanoindentation [20], micropillar splitting [21], clamped beam bending [22], or micro-cantilever bending [23-25]. Among them, the single micro-cantilever bending fracture tests are widely used due to their relative ease in controlling small sample geometries. However, FIB artifacts [26, 27] such as Ga ions implantation, segregation, and residual stresses introduced during sample preparation can severely affect fracture toughness measurements [28]. As an innovative method, the bridge notch method proposed by Matoy et al. [29] generates natural cracks and reduces the effects of FIB-induced damage, resulting in a reliable determination of the intrinsic fracture properties of the material. However, the failure behavior of the bridge has not been thoroughly observed and discussed in experiments, so more detailed studies are required.

Following the further investigation of the methodology for measuring fracture toughness with *in situ* SEM bridge notch micro-cantilever bending tests, the effect of grain boundary on fracture toughness were investigated through three key aspects:

(1) The effect of grain boundaries on fracture toughness at room temperature:

Previous studies have shown that grain boundary engineering can improve the fracture toughness of hard coatings. However, quantitative analysis of the effect of grain boundaries on fracture toughness is still limited. This limitation stems partly from the complexity of the sample preparation, as it is extremely challenging to synthesize two coating systems with identical or similar chemical/defect structures that differ only in grain boundary density. Small changes in deposition parameters can lead to significant changes in material properties, limiting the

feasibility of fair comparisons between sample systems that differ only in grain size. These complexities prevent a deeper understanding of the specific contribution of grain boundaries to fracture toughness.

(2) Effect of grain boundary orientation on fracture toughness at room temperature:

Studies have shown that different grain boundary orientations lead to anisotropy in fracture toughness. For example, high-entropy alloy films exhibit lower fracture toughness when tested perpendicular to the growth direction compared to tests performed parallel to the growth direction [30]. This effect varies depending on the material and grain boundary characteristics. Notably, there is a lack of in-depth research on how grain boundary orientation affects fracture toughness for widely used nitride hard coatings such as CrN and AlN. Filling this gap is critical to understanding the specific role of grain boundary orientation in fracture toughness of nitride hard coatings.

(3) Role of grain boundary on fracture toughness at elevated temperature:

There are significant differences in fracture toughness for nitride hard coating at elevated temperatures. Previous studies have reported that the fracture toughness of TiN [31] and CrN [32] coatings decreases significantly when the annealing temperature exceeds the deposition temperature. This phenomenon may be related to the formation of pores at grain boundaries, which weakens the toughness of the material. However, researchers found no significant degradation in the properties of CrN films after long-term annealing when tested on re-milling samples [33]. Therefore, the mechanism leading to the tendency of the difference in fracture toughness of CrN coatings at elevated temperatures and the role of grain boundaries in this phenomenon remain poorly understood. These differences in tendency may be due to inconsistencies in the annealing state of the samples or diffusion of Ga ions introduced during FIB milling at high temperatures. A systematic study of the sample's behavior at different temperatures, annealing states, and Ga ions conditions is essential to reveal the potential mechanisms of the effect of grain boundary on the fracture toughness of hard coatings.

1.2 Objectives

This thesis provides a systematic investigation of the bridge-notch designs on micro-cantilever fracture testing. Subsequently, the improved methdology is used to systematically investigate the influence of grain boundaries on the fracture toughness of hard coatings at ambient and elevated temperatures. The following points should be answered.

(1) Can natural cracks be introduced and FIB artifacts reduced in bridge notch micro-cantilever and how the data obtained at bridge failure can be interpreted for fracture analysis?

(2) How does the presence and orientation of columnar grain boundaries affect the fracture toughness of hard coatings?

(3) What is the role of grain boundaries on the fracture properties of hard coatings at elevated temperatures, and do Ga ions and annealing states affect test results?

1.3 Strategy

The aim of this thesis is to optimize and understand the bridge notch design to achieve a more reliable fracture toughness measurement method that will efficiently mitigate the FIB artifacts and increase the statistics. The optimized geometry will be used to conduct a systematic study of the effect of grain boundaries on the performance of hard coatings, including the effect on fracture toughness at both ambient and elevated temperatures. The goal of this research is to reveal the intrinsic influence of grain boundaries on the fracture toughness of hard coatings and to provide theoretical support to further enhance their reliability in practical applications.

Further research on methods to measure fracture toughness in micro-scale:

Micro-cantilever samples with extremely thin bridge notches were prepared using FIB milling. Afterwards, a high stiffness, low noise *in situ* SEM indenter device was utilized to evaluate the fracture toughness of the hard coatings by analyzing the data from the video of the tests and the displacement-loading force curves.

The effect of columnar grain boundaries on fracture toughness:

The hard coatings with two different microstructures, columnar grains and epitaxial layers, were quantitatively and qualitatively studied by bridge notch micro-cantilever fracture test to evaluate the effect of columnar grain boundaries on the fracture toughness. Afterwards, the fracture behavior of different GB orientations is comprehensively analyzed by applying two loading directions parallel and perpendicular to the film growth direction.

The fracture toughness of CrN coatings at elevated temperatures:

The fracture toughness of the CrN coating was tested by preparing a bridge notch micro-cantilever beam using FIB milling. High-temperature micromechanical experiments were performed in an *in situ* SEM with the temperature ranging from 25 °C to 600 °C and the toughness data were recorded as a function of temperature. A detailed study of annealing states, Ga ions, and residual stress was carried out through comparative experiments. Afterward, the thin lamella of the annealed sample was analyzed using transmission electron microscope (TEM) and Electron energy loss spectroscopy (EELS) instrumentation to understand the role of grain boundaries.

1.4 Structure of the thesis

Directly after the introduction chapter, summarized in Chapter 2 is the literature review and fundamental theoretical knowledge closely pertinent to the current work. Chapter 3 presents in detail how to optimize the bridge notch micro-cantilever geometry to promote crack arrest before the final fracture, and provides guidance for the geometry control and data analysis, which is published as *Y. Zhang, M. Bartosik, S. Brinckmann, S. Lee and C. Kirchlechner, Direct observation of crack arrest after bridge notch failure: A strategy to increase statistics and reduce FIB-artifacts in micro-cantilever testing [J], Mater. Des., 233 (2023) 112188*. Chapter 4 presents the result of a significant decrease in fracture toughness due to the presence of grain boundaries, which is published as *Y. Zhang, M. Bartosik, S. Brinckmann, U. Bansal, S. Lee and C.*

Kirchlechner, Columnar grain boundaries are the weakest link in hard coatings: insights from micro-cantilever testing [J], Mater. Res. Lett. (2025) 1-9. Chapter 5 discusses the influence of grain boundary orientation, which is published as *Y. Zhang, M. Bartosik, S. Brinckmann, S. Lee, and C. Kirchlechner, Toughening nitride hard coatings by deflecting cracks along grain boundaries [J], Mater. Sci. Eng. A (2025) 148392.* Chapter 6 reports on the role of grain boundary and effects of annealing states and Ga ions on the fracture toughness of CrN coatings at elevated temperature, which is intended to be submitted as *Y. Zhang, M. Bartosik, S. Brinckmann, U. Bansal, S. Lee and C. Kirchlechner, Interplay of oxidation and void formation on degradation of fracture toughness of CrN coatings during thermal exposure [J], in preparation, 202*6. In the end, I will summarize my present work and give perspectives that require further investigation to understand the effect of grain boundaries in nitride coatings at ambient and elevated temperatures.

2 Fundamentals and background

Recently, the design and development of protective hard coating systems have made significant progress, and breakthroughs have been achieved in the enhancement of key performance indicators such as coating mechanical strength, hardness, and wear resistance [34-37]. The thickness of such hard coatings, which is only a few micrometers, directly determines the service life of the components under extreme service conditions as a core functional material for surface engineering [5, 8, 38]. It is, however, worth noting that such hard coating materials generally exhibit typical brittle fracture features [39-41], and their lower fracture toughness values can easily trigger crack initiation and propagation of the coating system under cyclic loading and temperature, which ultimately leads to the overall failure of the system [42]. Consequently, the establishment of reliable fracture toughness characterization methods for optimizing the fracture toughness of coatings has become a key scientific concern for improving the engineering performance of hard protective coatings.*

Regarding the characterization of the fracture behavior of brittle hard coatings, the theoretical framework of Linear Elastic Fracture Mechanics (LEFM) exhibits unique applicability, making the measurements of plane-strain fracture toughness physically reliable and valuable for engineering guidance [43].*

2.1 LEFM theory

LEFM is a basic fracture mechanics approach for materials that remain elastic during crack propagation. The theory is most relevant to brittle materials, which typically exhibit minimal plastic deformation before fracture. It is based on the tip of the stress field around the crack and the energy required to produce a new fracture surface. The stress intensity factor K is a key parameter in the LEFM that quantifies the tip of the stress field around the crack, which plays a key role in understanding and predicting the cracking behavior of stressed brittle materials.*

The origins of LEFM emerge from the pioneering work of Griffith in the early 20th century. Based on previous findings [44, 45], Griffith [46] utilized an energy balance approach to explain why materials fracture at loading stresses significantly lower than their theoretical strength. According to Griffith's theory, the propagation of a crack depends on whether the energy released during its propagation exceeds the energy required to form a new fracture surface. If a through-thickness crack situated within an infinitely wide plate is subjected to a remote tensile stress, the requisite fracture stress, denoted by σ, is required to satisfy the following equation:

$$\sigma = \left(\frac{2E\gamma_s}{\pi a}\right)^{1/2} \tag{2.1}$$

where E is Young's modulus, γ_s the surface energy of a material and a is the half crack length.*

*AI-assisted translation, see Appendix 8.4 for documentation of prompts.

Subsequent studies have shown that there is a corresponding energy dissipation when plastic deformation occurs at the crack tip, Irwin [47] and Orowan [48] have independently modified the Griffith model to take into account the plastic work generated per unit area of the surface, with the new equation as follows [48-50],

$$\sigma = \left(\frac{2E(\gamma_s+\gamma_p)}{\pi a}\right)^{1/2} \tag{2.2}$$

where γ_p is the plastic work per unit area of surface created and is typically much larger than γ_s.*

Later, Irwin [51] proposed the concept of energy release rate G. The critical energy release rate (G_C) was introduced including both surface energy and plastic work energy. The relationship between stress σ, critical energy release rate G_C, and crack length a is expressed as Euqation (2.3).*

$$G_C = \sigma^2 \pi a/E \tag{2.3}$$

In addition to understanding the fracture process from an energy perspective, Irwin [52] and others [53-55] went beyond the energy concept by introducing stress intensity factors to describe the stress distribution near the crack tip in linear elastic materials. There are three modes of fracture, Mode I is identified as the opening mode, where the crack surfaces move perpendicular to each other, and Modes II and III are sliding and transverse tearing. In an isotropic linear elastic material, the stress field in front of the crack tip can be expressed as follows:

$$\sigma_{ij}(r,\theta) = \frac{K_{(I,II,III)}}{\sqrt{2\pi r}} f_{ij}^{(I,II,III)}(\theta) \tag{2.4}$$

where σ_{ij} is the stress tensor, K is the stress intensity factor under the loading Mode I, II, III, r is the distance from the crack tip, θ is the angle from the crack, and $f_{ij}(\theta)$ is the angular-dependent dimensionless term. Although the stress intensity solution is given in many forms, K can always be related to the crack by appropriate correction factors [49]:

$$K_{(I,II,III)} = Y\,\sigma\sqrt{\pi a} \tag{2.5}$$

where σ is the applied stress, a is the crack length, and Y is dimensionless constant depending on geometry and loading mode. For the most commonly studied mode I, fracture occurs when the K_I exceeds a critical value known as the fracture toughness (K_{IC}), which is a material property under plane strain conditions. The plane strain fracture toughness K_{IC} is regarded as an inherent property of the material and can be utilized as a metric for comparing the fracture resistance of different materials. To ensure valid plane strain conditions, the sample size must meet the following criteria [56]:

$$a, B, (W-a) \geq 2.5\left(\frac{K_{IC}}{\sigma_{YS}}\right)^2 \tag{2.6}$$

*AI-assisted translation, see Appendix 8.4 for documentation of prompts.

where B represents the thickness of the specimen, W represents the width of the specimen, and σ_{YS} represents the yield strength of the material.*

The determination of this Mode I stress strength factor and fracture toughness can be determined experimentally using standardized test methods, such as compact tensile specimens, single edge notched bending geometries, bending specimens, disc specimens, and medium tensile panels. In each case, cracking in the specimen is introduced by fatigue, although the fatigue loading requirements vary from standard to standard [56-58].*

2.2 Micro measurement methods

Notably, there is no standardized procedure for evaluating micro/nano-scale fracture toughness [2]. A conventional test method is commonly performed at the macroscopic scale. However, with the advent of miniaturized materials and the advancement of materials research, the traditional methods of tensile and three-point support experiments are extremely challenging to apply when the sample size reaches the dimensions of the coating thickness. Although fatigue pre-cracking has been achieved, obtaining atomic-level sharp notches by fatigue pre-cracking is generally challenging at micrometer dimensions[17, 59, 60].*

The development of advanced machining equipment and testing platforms has made it possible to prepare samples with micro-dimensions, thus facilitating microscopic testing. Currently, a variety of methods are employed to evaluate fracture toughness at small length scales [17, 61]. These include nanoindentation, pillar splitting, double cantilever bending test, clamped beam bending, and single cantilever bending test. Among them, the single cantilever fracture test has emerged as the most prevalent due to its relative simplicity in fabricating samples with well-defined geometries.*

2.2.1 Nanoindentation

At the microscale, the advancement of nanoindentation has enabled the evaluation of fracture toughness in thin films and micro samples [20, 62]. This method is predicated on the estimation of the fracture toughness of materials by introducing and analyzing radial cracks through a sharp indenter [63-67] (e.g., Vickers, Berkovich, and cube-corner). The original Lawn-Evans-Marshall (LEM) model [68-71] is a pioneering work with a classic formula proposed:

$$K_C = \alpha \cdot \sqrt{\frac{E}{H}} \cdot \frac{F_{max}}{c^{2/3}} \tag{2.7}$$

where c is the average crack length in Figure 2.1, E is elastic modulus, H is the material hardness, F_{max} is the maximum load, and α is a coefficient related to the indenter geometry. However, this model is mainly applicable to brittle bulk ceramic materials, and the accuracy of the LEM model may be affected when the crack geometry [72] deviates from the typical half-penny [17].*

*AI-assisted translation, see Appendix 8.4 for documentation of prompts.

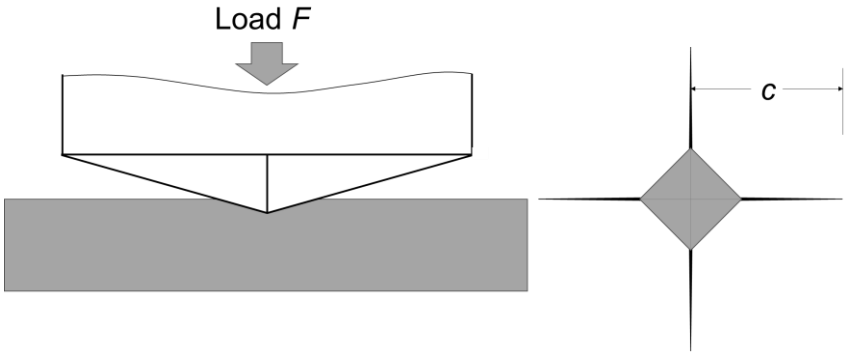

Figure 2.1. Schematic of crack geometry under sharp Vickers indentation loading, reprinted from [65].

In general, the fracture toughness test method based on indentation has the advantages of simple sample preparation, fast test, and high-throughput research, but it also has certain limitations. These limitations include the effects of substrate, residual stress, the geometry of the indenter, and the diversity of crack geometry on the accuracy of the test results [17, 73-75]. Consequently, this method is regarded as a semi-quantitative approach to evaluating the fracture toughness of materials, suitable for preliminary selection and relative comparison of the fracture toughness of different materials.*

2.2.2 Single cantilever bending test

In recent years, the micro-cantilever has played an important role in microfracture experiments due to its ease of fabrication and wide adaptability to different materials. In 2005, Di Maio and Roberts fabricated free-standing micro-cantilevers with notches in silicon using FIB technology and tested them using a nanoindentation instrument [24]. Since then, this approach has been progressively extended to the study of various materials with different geometries under diverse experimental conditions, resulting in a variety of experimental data and theoretical frameworks. These experiments are even combined with *in situ* SEM for monitoring, which allows precise observation of the crack propagation process. In addition to the FIB technique, chemical etching, lithography, and femtosecond laser ablation have been introduced to improve processing efficiency [76-78].*

The flexibility of the FIB-SEM instrument allows the preparation of micro-cantilever beams with various geometries on the sample surface. Among these, complex geometries such as pentagonal [24, 79-84] and triangular [85-88] cross-sections provide more options for investigating specific microstructures and interfaces. Rectangular [28, 29, 89-93] beams (Figure 2.2), on the other hand, are widely used for simplicity in fabrication. As long as the specimen size satisfies the small plastic zone size (see Equation. (2.6)), the fracture toughness can be calculated directly from analytical solutions by the following equation:

*AI-assisted translation, see Appendix 8.4 for documentation of prompts.

$$K_{IC} = \frac{F_C L}{BW^{3/2}} f(a/W) \tag{2.8}$$

where F_C is the fracture load, L is the distance between the notch and the load point, B is the beam thickness, W is the beam width, and $f(a/W)$ is a dimensionless geometric function that can be determined by FEM simulation for various notched beam geometries [29, 94, 95]. In conclusion, the development of single micro-cantilever beam fracture experiments not only enriches the methodology of fracture mechanics research but also provides an important tool for exploring the microfracture behavior of a wide range of materials.*

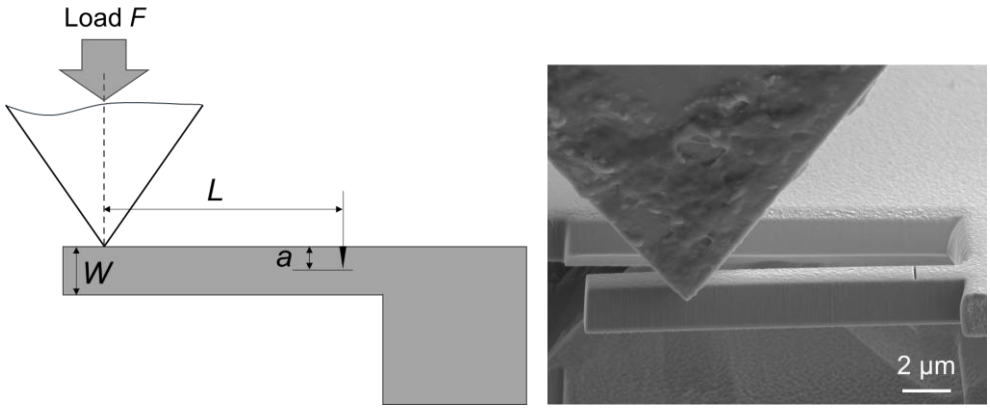

Figure 2.2. (a) Schematic and (b) SEM image of a single cantilever beam on nitride coating, reprinted from [96].

2.2.3 Clamped beam bending

Clamped beam bending is a novel geometrical method applied to small-scale fracture testing in recent years, initially used to investigate the fracture toughness of (Pt,Ni)Al bond coats [22]. Compared to the conventional three-point bending test, this method realizes pure Type I loading and controlled hybrid loading by clamping the ends of the beam and applying the load at the notch Figure 2.3. This enables the stable propagation of cracks in brittle materials [97-99], thus providing a new tool for the study of fracture toughness and toughening mechanisms in materials. It facilitates staged crack propagation and arrest before complete failure under precise control of the loading conditions and enables the generation of a real crack from the notched tip processed by FIB milling; thereby circumventing the influence of the finite notched root radius on the measurements. Furthermore, the K_{IC} values obtained at different a/W ratios exhibit minimal variation, indicating that the damage to the notch root by FIB has little effect on the results.*

*AI-assisted translation, see Appendix 8.4 for documentation of prompts.

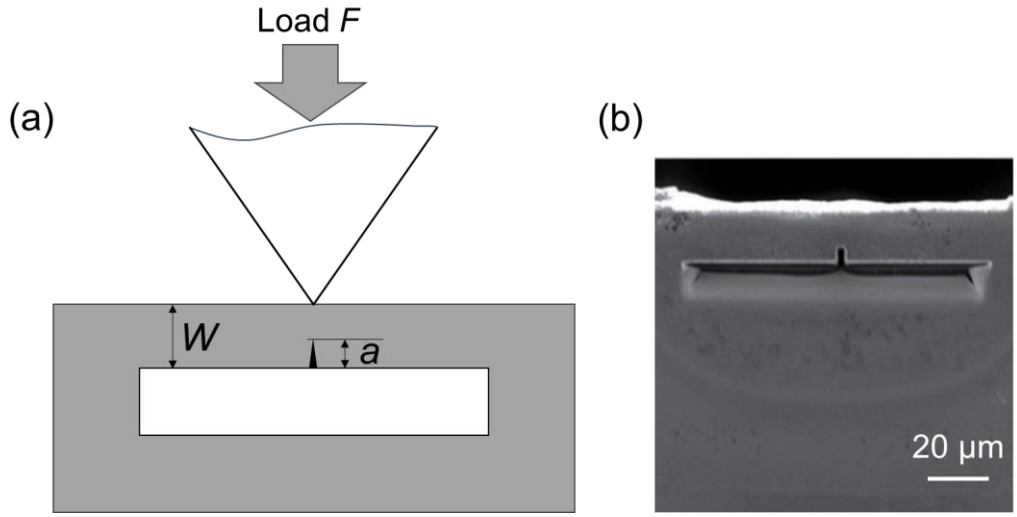

Figure 2.3. (a) Schematic of a clamped beam cantilever and (b) SEM image of clamped beam cantilever on (Pt,Ni)Al bond coats, reprinted from [22].

Despite many advantages, clamped beam bending tests have the following limitations [99]. Firstly, the effect of residual stress presents a challenge. The ends of the beam are constrained, resulting in a non-negligible influence of residual stresses on the fracture behavior. Instead, the residual stress values require independent measurement methods and account in the FEM. While this property may offer insights into the actual fracture process of the material, it inevitably increases the complexity of the test. In addition, this method lacks an analytical formulation due to the non-monotonic variation of the stress intensity factor (K_I) with the a/W ratio. Consequently, FEM simulations are currently necessary to extract K_I values for each test, increasing the computational cost of the experiment. *

2.2.4 Double cantilever bending test

Conventional double cantilever beams (DCBs) typically apply bending moments under symmetric precracking conditions to promote stable crack extension [23], and similar principles can be applied to micro-scale studies [33, 99-102]. Liu et al. successfully investigated the microfracture mechanics of CrN-based hard coatings with DCB geometry using a flat punch to apply load [102]. The design needs to satisfy specific size ratio and symmetry requirements. Symmetry is particularly critical in this geometry, as the two arms must be of equal width and the flat punch indenter surfaces need to be perfectly parallel to ensure that the loading process complies with the I-type loading requirements. However, it was observed that in the tests on brittle silicon materials, this geometry did not support any stable crack propagation, and all samples fractured catastrophically after the initial crack opening [99]. This phenomenon may be attributed to the spontaneous release of energy stored in the indenter during crack propagation, leading to instability and catastrophic failure. But the critical stress intensity factor (K_{IC}) can still be calculated from the maximum fracture load, without measuring the crack length [102],

*AI-assisted translation, see Appendix 8.4 for documentation of prompts.

$$K_{IC} = \sqrt{3} \cdot \frac{(e-\mu h)}{td^{3/2}} F_{max} \tag{2.9}$$

where F_{max} is the fracture load, $e=(d-w)/2$, μ is the coefficient of friction between the punch and the sample, t is the thickness of sample. d, w, and h are beam dimensions as shown in Figure 2.4.*

Alternatively, a wedge tip can be used for loading [99]. However, compared with flat punches, wedge tip involves more serious friction problems, including the necessity of modeling the friction generated by the contact between the tip and the two cantilever side walls, which complicates the analysis. To generate an I-type load, the wedge tip must be precisely located in the center between the two cantilevers. In contrast, flat punch loading avoids the complex analysis caused by friction effects and avoiding the determination of the loading point [103].*

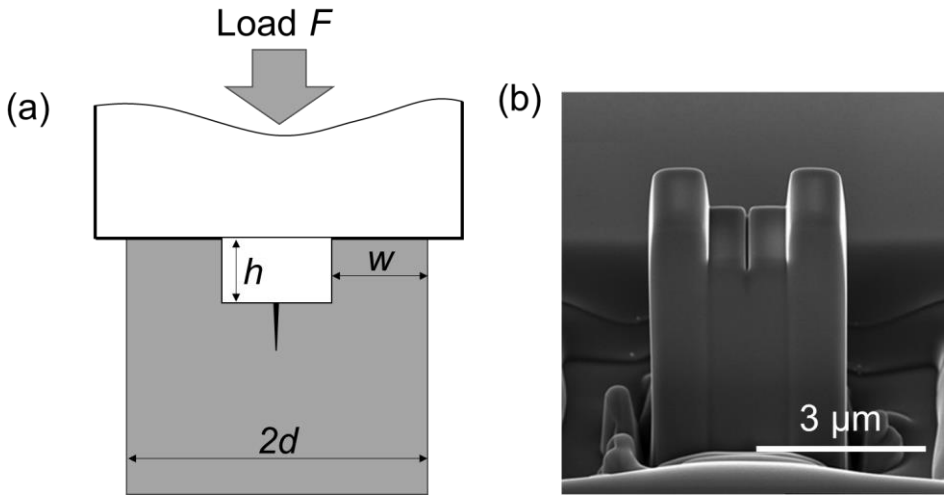

Figure 2.4. (a) Schematic and (b) SEM image of a SiC double cantilever beam, reprinted from [102].

In conclusion, the DCB structure has the capacity for utilization in the study of fracture toughness of brittle materials. The flat punch loading method provides more accurate experimental conditions for crack propagation and circumvents the interference of friction problems on the test results. However, the potential instability of crack growth and the strict requirements of sample size continue to limit the application of this test method. Future research may include optimizing the geometric design of the beam to improve the stability of crack propagation, further reducing the influence of friction effects on experimental results and expanding its application to a wider range of material systems.*

2.2.5 Mircropillars spliting

The micropillar splitting method, as developed by Sebastiani et al. [21], is a small-scale fracture toughness measurement technique that has wide application in the characterization of the fracture toughness of brittle materials [104-107]. This method requires the preparation of micropillar

*AI-assisted translation, see Appendix 8.4 for documentation of prompts.

samples with the ratio of height to diameter greater than 1 by FIB milling and indentation with a sharp indenter (Figure 2.5). As the applied load increases, the crack nucleates under the indenter and subsequently propagates to the surface of the pillar at a critical fracture load (F_C), which is then determined by the load-displacement curve. Combined with the pillar radius (R_p) and the coefficient (γ), which is related to the crack growth in the pillar, the indenter geometry, and the material properties, the fracture toughness can be estimated by the following equation:

$$K_C = \gamma \cdot \frac{F_C}{{R_p}^{3/2}} \tag{2.10}$$

the coefficient γ and the validity of this equation were determined with FEM on pillar indentation cracking [17, 21].*

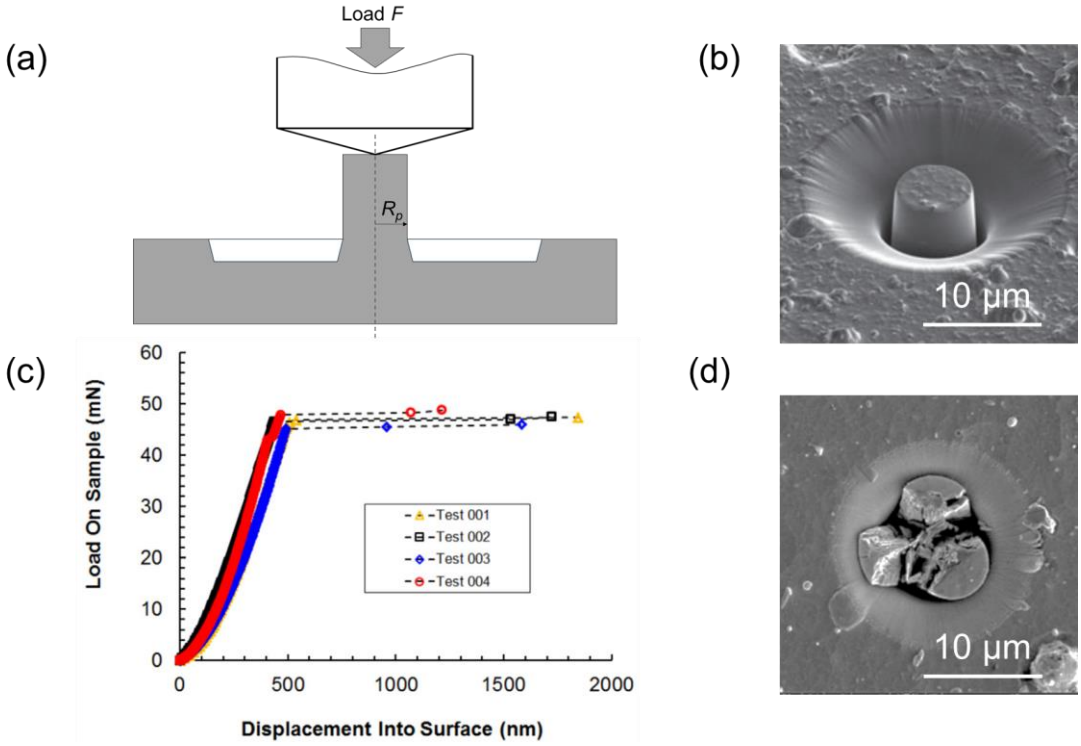

Figure 2.5. (a) Schematic of the pillar splitting with Berkovich indenter. (b) Example of a CrAlN/Si_3N_4 pillar before splitting, (c, d) representative load-displacement curves obtained on the CrN sample and SEM image of a pillar after splitting, recombined based on [21].

Compared to the cantilever bending technique, the micro-pillar splitting method offers distinct advantages, including its simplicity of sample preparation and reduced ion damage. In addition, the release of residual stresses during FIB milling and the occurrence of pillar splitting at a shallow indentation prevent the influence of residual stresses [21, 108] and substrate [21].*

However, the micro-pillar splitting method also has limitations, including the difficulty of distinguishing between crack initiation and propagation processes and its applicability exclusively

*AI-assisted translation, see Appendix 8.4 for documentation of prompts.

to brittle materials. In addition, the corresponding coefficient (γ) for each material must be obtained by FEM, which increases the complexity of the analysis of the experimental data. In particular, the validation of the fracture toughness data obtained under the unnotched condition remains controversial [109].*

2.3 Notch type

Fracture mechanics studies necessitate the reliable determination of the plane-strain fracture toughness K_{IC}, typically through forming an atomically sharp notch by fatigue pre-cracking [17]. Although fatigue pre-cracks are commonly used experimentally at the macroscopic scale, this is difficult to achieve at the micrometer length scale, where the introduction process is complicated and has a low success rate [59, 86, 110, 111]. Notches are therefore usually fabricated by FIB milling for high-precision localization and efficient preparation in micro-cantilever beam fracture testing. However, the commonly used Ga-ion FIB is prone to FIB artifacts such as over-fibbing [95], Ga-ion implantation [112], knock-on damage [113], FIB-induced crystal defects [114, 115], residual stresses [88], finite notch root radius [29, 116] and redeposition [26]. To minimize these FIB artifacts and obtain stable crack growth, two pre-notch shapes have been developed instead of a through-thickness notch, including the chevron notch, and the bridge notch. A comparison of these three notch shapes is presented below.*

2.3.1 Through-thickness notch

In microscale fracture testing, through-thickness notches have become a common design due to their simple and well-defined geometry, which facilitates the calculation of fracture toughness from experiments and applies to both brittle and ductile materials.*

Typically, through-thickness notches are fabricated by milling along the target region under optimized FIB conditions (Figure 2.6). However, the fabrication of such notches is challenging due to the high FIB milling rate at the sample edge, which can lead to an over-fibbing effect [95]. This phenomenon results in a bent notch front rather than a straight one. This, in turn, increases the error and scatter of experimental data and complicates the stress field around the notch. Therefore, highly specialized techniques are required to achieve ideal through-thickness notches with straight crack fronts through multi-step milling. While FIB milling can produce sharp notches with high spatial resolution at the desired location, it still has a root radius at the notch tip, which remains larger than that of natural cracks [117] or fatigue cracks [59, 86, 110, 111].*

*AI-assisted translation, see Appendix 8.4 for documentation of prompts.

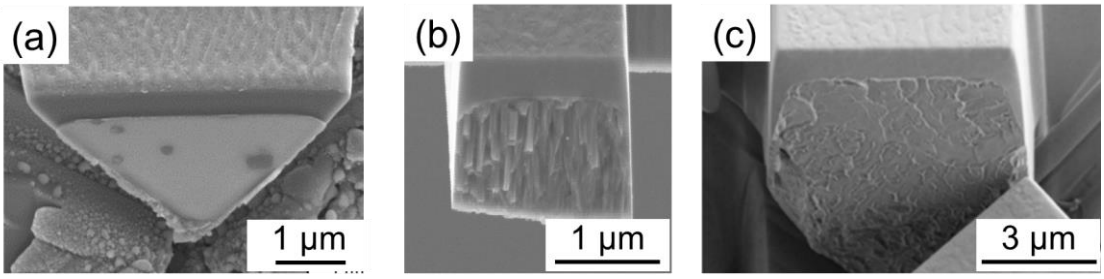

Figure 2.6. SEM images of a through-thickness notch fractured in (a) triangular [88], (b) rectangular, and (c) pentagonal [84] single cantilever beams.

2.3.2 Chevron notch

To obtain atomic-level sharp pre-cracks, Mueller et al. [118] conducted the first systematic study of chevron notch in micro-cantilever fracture experiments with quartz and alumina. In this geometry, the notch tip serves as a stress concentration point, and cracks can initiate and propagate stably at lower loads until a fracture occurs after reaching the critical crack length. This notch design not only effectively induces the formation of sharp pre-cracks, but also reduces the artifacts introduced by FIB machining.*

The chevron notch, due to its triangular ligament structure (Figure 2.7), eliminates the need for fatigue pre-cracking in fracture toughness testing of brittle materials [79, 86, 118-121]. However, the symmetry of the chevron notch is difficult to be accurately maintained during FIB milling, which may lead to the complication of mixed-mode fracture toughness and crack propagate behavior. Therefore, the limitations of the chevron notch still need to be fully considered when applying it to fracture toughness testing.*

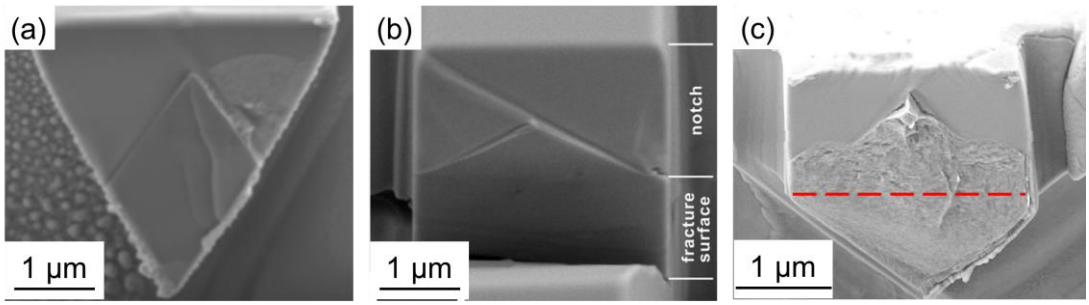

Figure 2.7. SEM images of chevron notch on fracture surface in (a) triangular [86], (b) rectangular [121], and (c) pentagonal [79] single cantilever beams.

*AI-assisted translation, see Appendix 8.4 for documentation of prompts.

2.3.3 Bridge notch

In order to simplify the machining process and reduce the difficulty of preparation, as well as to effectively minimize the artifacts of FIB machining and introduce a naturally sharp pre-crack, Matoy et al. [29] proposed an innovative geometric micro-cantilever with a bridge notch. The design optimizes the geometry by maintaining two side-ligaments at the through-thickness notch shown in Figure 2.8. During loading, the material bridge will fail firstly due to the higher stress intensity factor, generating sharp atomic pre-cracks. This method of pre-crack has been shown to effectively mitigate the impact of FIB-induced damage, thereby enabling more precise measurement of the material's intrinsic properties.*

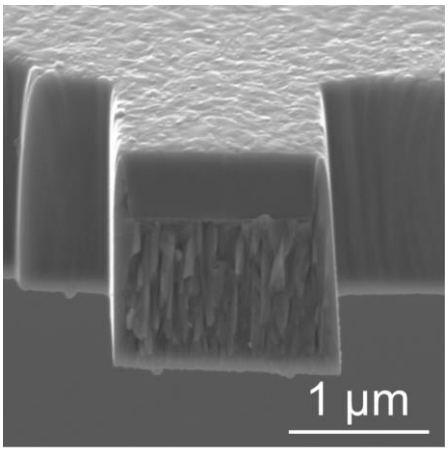

Figure 2.8. SEM images of bridge notch on fracture surface of single cantilever beams (acquired by author).

The bridge notch micro-cantilever has been widely utilized in a range of material systems, including nitride coatings [32, 33], carbide hard coatings [89], silicon oxide films [29], and intermetallic phases [122]. This design successfully mitigates the experimental errors associated with over-fibbing effects and finite root radius in through-thickness notches, while offering enhanced processing ease and reduced experimental scatter. Theoretically, the design of the bridge notch enables the control of the crack propagation during loading, which is particularly well-suited for testing in displacement control systems. This capability facilitates the generation of natural cracks and prevents catastrophic failure of the micro-cantilever. However, the reliability of the bridge notch micro-cantilever bending test depends upon the optimization of notch geometry. Inappropriate geometric parameters may produce immediate catastrophic fracture without the bridge failure before the final fracture, thereby leading to a misestimation of fracture toughness [95]. Therefore, to ensure the reliability of the test results, it is necessary to further investigate how to ensure that the bridge failure occurs before the final fracture so that natural pre-cracking can be introduced before the eventual fracture [123]. This subject will be thoroughly studied and analyzed in Chapter 3.*

*AI-assisted translation, see Appendix 8.4 for documentation of prompts.

2.4 Thermal stability of nitride thin films

Nitride coatings are a high-performance surface protective material with several significant advantages, primarily its excellent mechanical properties and corrosion resistance, which have led to the practical application in several industrial fields, for instance, diffusion barrier layers in semiconductor technology, wear-resistant layers on cutting tools and mechanical components [124-126]. Notably, such protective coatings are often required to withstand complex mechanical loads and maintain stable service performance in high-temperature environments for long-term periods [127-129].*

However, nitride coatings prepared by physical vapor deposition techniques generally exhibit thermodynamically unstable microstructures, comprising point defects, dislocations and sub-grains [130, 131]. When exposed to high-temperature environments, these unstable microstructures dissipate energy through dynamic processes such as point defects migration, dislocation annihilation, and grain boundary migration, thereby inducing microstructural evolution of the coating system, such as recovery, grain growth, and recrystallization behavior. In addition, the thermal stability of nitride coatings also involves key processes such as oxidation and phase decomposition reactions. Recent studies have demonstrated a significant correlation between the mechanical properties of hard coating systems at high temperatures and the evolution of their microstructures as well as the stability of their chemical compositions at high temperatures [131-138]. These findings emphasize the need for research on the thermal stabilization mechanism of nitride coatings, which is of great significance for improving the reliability of coating materials under extreme conditions.*

2.4.1 Recovery

As the initial process of coating heat treatment, the recovery refers to a series of annealing phenomena that occur prior to the appearance of new unstressed grains. These phenomena include the migration and combination of point defects, the rearrangement and annihilation of dislocations, and the growth and coalescence of subgrains [139]. The primary driving forces of the recovery process are the temperature and stresses within the coating [130]. The study of the recovery effect is typically accomplished by *in situ* measuring stress at high temperatures [129, 140]. The stress relaxation that occurs during heat treatment has been found to be linearly related to the biaxial stress of the coating in the as-deposited state shown in Figure 2.9 [131, 141].*

The state of the inherent residual stresses in a coating significantly influences its behavior during annealing or recovery [130, 142]. Voids and vacancy defects formed during deposition introduce tensile stress in the coating. Ion bombardment can inhibit these defect densities, thereby introducing compressive stress. In addition, instead of being released during annealing, this tensile stress may further increase due to the recovery effect. The reason for this is that the thermal energy induces point defects in the lattice to migrate to grain boundaries or other defect aggregation regions, and the accumulation of defects leads to local volume contraction, which in

*AI-assisted translation, see Appendix 8.4 for documentation of prompts.

turn triggers an increase in the overall tensile stress in the coating. In contrast, recovery processes can often significantly reduce compressive stress in coatings that are initially under compressive stress. Recovery promotes stress release and atomic rearrangement, resulting in an effective reduction of compressive stresses. Therefore, the type of initial residual stress in a coating not only determines its mechanical response during the deposition and post-treatment but also has a direct impact on subsequent stability and service performance. Understanding and manipulating such inherent residual stresses is an important way to optimize the microstructure and mechanical properties of coatings.*

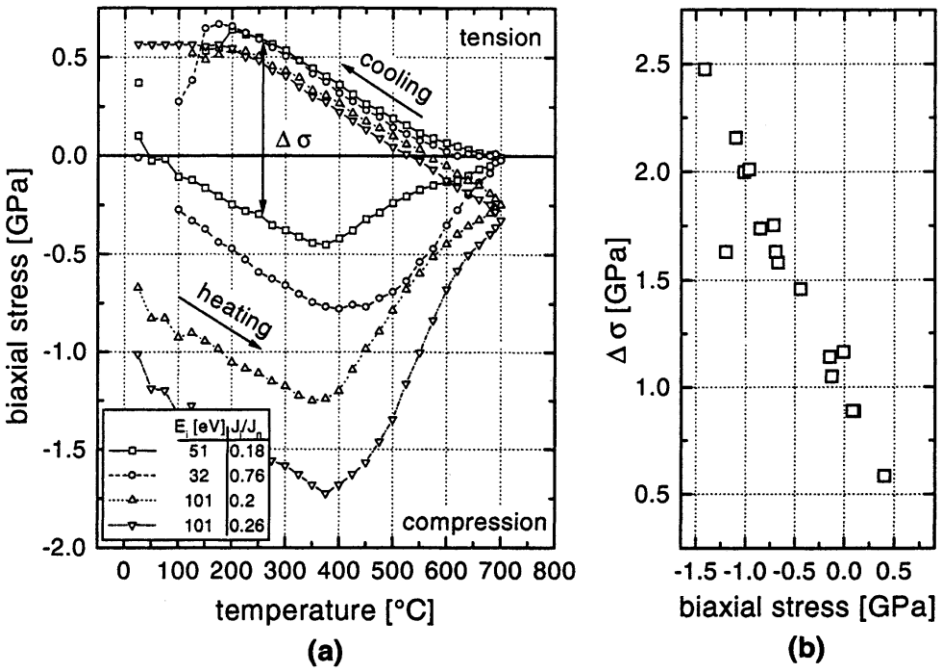

Figure 2.9. (a) Stress-temperature cycles for CrN coatings deposited using different ion bombardment conditions on silicon and (b) Effect of biaxial stress in the as-deposited state on the stress relaxation during the heat treatment up to 700 °C under different ion bombardment conditions [141].

2.4.2 Recrystallization

Recrystallization is a process in which new grains with a low dislocation density are formed within the deformed or recovered microstructure [35, 143]. These grains then grow to replace the regions containing defects with kinetics like a phase transition, where nucleation marks the initial formation of new grains and growth replaces the original grains. Recrystallization requires sufficient thermal activation and driving forces [130]. For hard coatings, recrystallization behavior varies widely. For instance, CrN coatings demonstrate minimal stability and typically recrystallize at relatively low temperatures (400-550 °C) as equiaxed Cr_2N grain [124, 144, 145]. Conversely, (Ti,Al)N coatings exhibit high stability with no detectable recrystallization after annealing at 900 °C for 2 h [124]. Differential scanning calorimetry (DSC) provides an excellent

*AI-assisted translation, see Appendix 8.4 for documentation of prompts.

method for accurately determining the onset temperature of recrystallization [146]. However, the energy released from the recrystallization and grain growth of single-phase coatings characterized by larger grain sizes is not sufficiently quantifiable with DSC [130].*

2.4.3 Diffusion

In most physical vapor deposition processes, low-energy ion irradiation is widely used to control the microstructure and chemical composition of the film during growth. However, despite the positive effects of ion bombardment on densification and composition control, it may also bring some potential adverse effects, including the generation of point defects, doping of inert gases, and the introduction of excessive nitrogen. These defects and impurities will cause the coating to be in a strong non-equilibrium state and promote the formation of metastable phases or non-equilibrium structural features. This non-equilibrium structure induces diffusion driving forces, further affecting the stability and performance of the material. Additionally, the impurities or lattice point defects of nitrides vary depending on the deposition process used for synthesis. These characteristics are expected to significantly affect the diffusivity of metals or nitrogen species in nitrides. However, the high melting point of nitride ceramics complicates diffusion measurements and often limits the availability of suitable radioactive tracers [124]. Usually, micro and macro stresses in Cr-N coatings affect the volume diffusion of Cr [147]. Defects (such as voids or vacancies) formed during the deposition process usually cause tensile stress, which reduces the diffusion barrier and facilitates the migration of chromium atoms in the nitride matrix. Conversely, some defects promote the formation of compressive stresses, which hinder the movement of lattice atoms, thereby inhibiting the bulk diffusion of Cr. As for nitrogen, its diffusivity is substantially faster than metal atoms [148], which is closely related to the smaller atomic radius of nitrogen.*

2.4.4 Oxidation

The oxidation behavior of nitride coatings has been extensively studied. For instance, the oxidation behavior and mechanism of Cr-N coatings in oxidizing atmospheres at temperatures up to 1000 °C have been the focus of numerous investigations [147, 149, 150]. The general reactions of oxygen with CrN and Cr_2N phases are as follows [150]:

$$2CrN_{(S)} + 1.5O_{2(g)} \rightarrow Cr_2O_{3(S)} + N_{2(g)} \tag{2.11}$$

$$Cr_2N_{(S)} + 1.5O_{2(g)} \rightarrow Cr_2O_{3(S)} + 0.5N_{2(g)} \tag{2.12}$$

Mayrhofer et al. [147] utilized both dynamic and isothermal thermo-gravimetric analysis (TGA) in the oxidizing atmosphere on the antioxidant properties and oxidation kinetics of Cr-N coatings, measured the activation energies of oxidation reactions at different stages, and also found that the oxidation behavior is related to its biaxial macroscopic stresses, its chemical composition, and the

*AI-assisted translation, see Appendix 8.4 for documentation of prompts.

intrinsic properties of the material. In addition, many factors can also affect the oxidation kinetics of the nitride coating, such as adsorption, nucleation, crystal growth, chemisorption, etc.*

2.4.5 Decomposition

Nitride coatings also tend to thermally decompose at high temperatures, influenced by the atmosphere, deposition method, and heating process. Ernst et al. [151] utilize TGA and differential thermal analysis (DTA) techniques on CrN coating at Ar atmosphere, it was determined that CrN coatings undergo two decomposition processes (Step #1; CrN→Cr_2N, Step #2 Cr_2N→Cr) from ambient temperature to 1440 °C. The decomposition temperatures of Step #1 ranged from 925 °C to 1118 °C, and the heating rate and deposition method were the main influences on this temperature. However, the decomposition of Step #2 occurs above 1200 °C, and is independent of the deposition method, exhibiting sensitivity only to the heating rate.*

Furthermore, Almer et al. employed X-ray diffraction (XRD) to examine the phase composition of CrN coatings subjected to varying temperature in an Ar atmosphere, revealing the emergence of the Cr_2N(300) peak at approximately 400 °C [144]. In contrast, Wu et al. noticed that Cr_2N coatings exposure at 900 °C for 5 h in a muffle furnace was observed to yield the CrN phase. They proposed a hypothesis that there is a phase transition from Cr_2N to CrN, the involved reaction is as Equation (2.13) [150], which was also observed by Mayrhofer et al [147]:

$$Cr_2N_{(S)} + 0.5N_{2\,(g)} \rightarrow 2CrN_{(S)} \tag{2.13}$$

According to the principles of thermodynamics, the stability of Cr_2N and CrN is influenced by temperature and the partial pressure of nitrogen [152]. This explains why the stability of Cr-N coatings in different atmospheres is different, and the Cr_2N phase can be observed in CrN coating at elevated temperatures under the Ar atmosphere. [144, 151].*

This section provides the theoretical foundation required for the present study. LEFM establishes the framework for fracture analysis in micro-cantilever bending tests, while the overview of various testing methods clarifies their advantages and limitations, demonstrating the broad application of single micro-cantilever bending tests. The review of different notch types indicates that the design of the bridge notch minimizes the FIB artifacts and enables natural pre-crack initiation. However, further investigation is needed to ensure that bridge failure occurred before the final fracture. Additionally, the part of thermal stability of nitride coating provides background for understanding how GBs influence fracture behavior under high temperature in this study.*

*AI-assisted translation, see Appendix 8.4 for documentation of prompts.

3 Direct observation of crack arrest after bridge notch failure: A strategy to increase statistics and reduce FIB-artifacts in micro-cantilever testing

Chapter 3 is based on a published journal article.

Y. Zhang, M. Bartosik, S. Brinckmann, S. Lee and C. Kirchlechner, Direct observation of crack arrest after bridge notch failure: A strategy to increase statistics and reduce FIB-artifacts in micro-cantilever testing, Mater. Des. 233 (2023) 112188. https://doi.org/10.1016/j.matdes.2023.112188

A detailed description of the contributions of all the researchers involved in experiments and interpretations can be found in the appendix.

3.1 Introduction

In recent years, there have been significant advances in the design of hard protective coatings that have yielded improved mechanical properties [35]. In hard coating applications, several micrometers thick coatings deposited on the substrate determine the service life of the component. Determining and optimizing their mechanical properties, for example, fracture toughness, has become one of the most challenging tasks since the conventional approaches cannot be applied and there is no standardized procedure to evaluate the fracture toughness at the micro/nano scale [32]. The most widely used experimental method for assessing fracture toughness K_{IC} at a small length scale is the single micro-cantilever fracture test [17, 153, 154], because it is relatively easy to fabricate samples with a well-defined geometry.

In most cases, micro-cantilevers and their pre-notch are fabricated using Ga^+ FIB milling. There are different types of pre-notches for single micro-cantilever beam geometry, for instance, a chevron notch [155], a through-thickness notch [156], and a bridge notch [29]. Compared to the simple and well-defined geometry of a cantilever with a through-thickness notch, it is difficult to determine the crack length in cantilevers with chevron notches during the test and to maintain the symmetry of the chevron notch during FIB milling. In the case of through-thickness notches, it is easier to calculate fracture toughness from the experiment because of its well-defined geometry, however, the higher milling rate of the FIB at the side of the cantilevers, so-called "over-fibbing" results in a curved notch front rather than a straight front. Furthermore, the stress-field around the over-fibbed notch is significantly more complicated compared to that of an ideal through-thickness notch.

Besides the over-fibbed notch geometry of a micro-cantilever, FIB-induced artifacts, for example, Ga^+ implantation [112], knock-on damage [113], FIB-induced crystal defects [114, 115], residual stresses [88], a finite notch root radius [29, 116] and re-deposition [26], strongly affect the fracture toughness values measured by micro fracture experiment. Although FIB milling can produce sharp notches at the desired location with high spatial resolution, it has a certain root radius,

typically around 10 nm [29], which is larger than that of natural cracks or fatigue cracks. There are alternative geometries for micro fracture tests, such as clamped beam bending geometry [99], which can promote stable crack propagation thus the sample fails by a natural crack, however, there are more complications and limitations in this geometry, for instance notch alignment. Another approach to circumvent the Ga+ FIB artifacts is using FIB with different ion species [105], or optimizing FIB milling conditions [33]. For instance, He from helium ion beam milling (HIM) does not show any chemical interactions with the sample [157] and also offers a smaller beam size, resulting in smaller notch root radius [158]. HIM can also be used to fabricate micro cantilevers, however, the milling speed is much slower than Ga^+ FIB milling [159].

One of the approaches to reduce the FIB-induced cantilever side effects is using a bridge notch. As soon as the thin bridge fails, an atomically sharp crack will be nucleated and propagate leading to the complete failure of the cantilever [29]. This method has been proven effective in various material systems such as carbide hard-coatings [89], silicon oxide thin films [29], or intermetallic phases [122]. The advantage of this geometry is that it can create a natural crack which is less affected by FIB damage, so that it is possible to measure materials' inherent properties. However, to the best of our knowledge, bridge failure had not been experimentally observed.

The computation of a new geometry factor is required to assess the fracture toughness from a single cantilever with a bridge notch. Brinckmann et al. [95] computed this geometry factor and related it to the geometry factor of a through-thickness one by defining a correction factor. Based on this correction factor and the geometry factor of a through-thickness notch, the local stress intensity at the bridge notch can be estimated.

In this study, we present the first observation of crack propagation and crack arrest at the bridge notch before the final fracture of a single cantilever in CrN/AlN multi-layered and CrN monolithic hard coatings. The quantification of the fracture toughness from the bridge-failure shows good correlation (less than 10% deviation) to the one calculated from the failure of the main through-thickness notch after the bridge failure, in other words crack arrests.

3.2 Materials and Methods

3.2.1 Thin coating preparation

Two different coatings were grown on Si (100) substrates by unbalanced reactive magnetron sputtering: monolithic CrN with a thickness of 1.5 µm and a CrN/AlN multi-layered coating with a total thickness of 1.9 µm. The CrN/AlN multi-layered coating consisted of alternating layers of approximately 4 nm CrN and 2 nm AlN. The coatings were prepared in an AJA ATC-1800 ultra-high vacuum deposition system equipped with one Cr (purity 99.95%) and one Al (purity 99.99%) target, which both had a three-inch diameter. The targets were powered in pulsed DC mode with a pulse frequency of 100 kHz and a pause of 1 µs. A time-averaged power of 300 W and 500 W was applied to the Cr and Al target materials, respectively. The coatings were grown in a mixed N_2/Ar (12 sccm / 8 sccm flow rate ratio) gas atmosphere at a total gas pressure of 0.2 Pa. A DC bias voltage of -70 V was applied to the substrates during coating growth to ensure the formation of a dense coating morphology. While the deposition parameters were kept constant throughout

the deposition process, mechanical shutters under computer control opened and closed at regular time intervals to create the multilayer structure (in the case of the CrN/AlN multi-layered coating, see Figure 3.1).

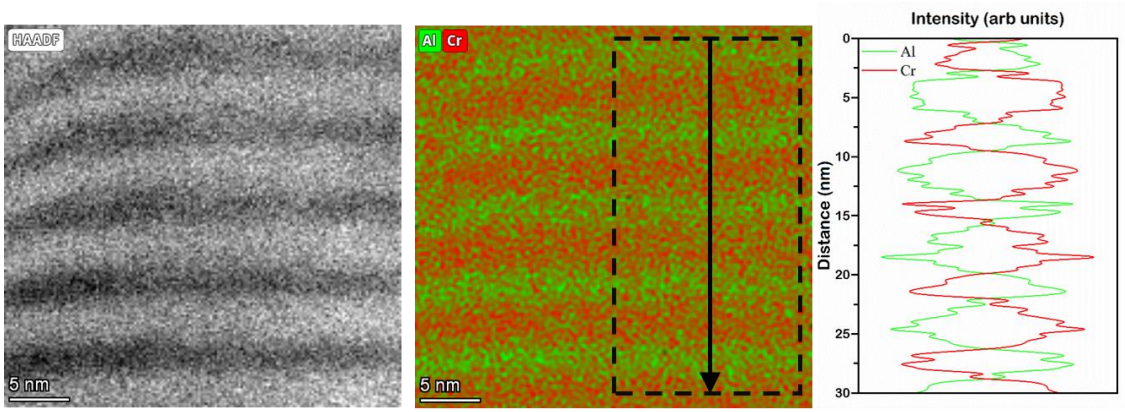

Figure 3.1. Scanning transmission electron microscopy energy dispersive X-ray spectroscopy map showing multi-layered structure of the CrN/AlN hard coating. The thickness of CrN and AlN layer is 4 nm and 2 nm, respectively. Reprinted from [123].

Prior to the deposition, the Si (100) substrates (7 x 20 x 0.38 mm^3) were pre-cleaned in an acetone- or ethanol-filled ultrasonic bath for at least 5 minutes in each, before they were clamped on the substrate holder and transferred to the vacuum chamber in the load-lock system. The base pressure in the vacuum chamber was below 3 x 10^{-6} mbar. After thermal cleaning of the substrates at 550 °C for 30 minutes, the substrates were ion etched for 5–10 minutes at 500 °C in pure Ar atmosphere and the targets were sputter-cleaned under the closed shutters for 5 minutes using the same parameters as later used during the deposition process, first in pure Ar gas and then in mixed N_2/Ar gas atmosphere. The substrates rotated constantly with a rotation frequency of about 0.5 Hz.

3.2.2 Fabrication of micro-cantilevers

Before producing cantilevers using FIB, the silicon substrates of both CrN/AlN multi-layered and CrN hard coatings were etched using a 30 wt.% potassium hydroxide solution for 30 min at 60 °C to obtain 20 µm long freestanding film segments. Then, the cantilevers were prepared by FIB milling (Crossbeam 550L, Zeiss) at 30 kV in 3 steps; rough milling with 3 nA, intermediate milling with 700 pA, and fine milling with 50 pA probe current. Notches were fabricated with a 20 pA current and 1.0 µs dwell time to have a straight notch front without noticeable FIB re-deposition. The geometry of cantilevers is shown in Figure 3.2; L is the distance between the loading position and the notch, H is the distance between the base of the cantilever and the notch, B is the cantilever width, b is the notch width, W is the cantilever thickness, a is the notch depth. The a/W ratios are between 0.2 and 0.3. The nominal width B of the cantilever was about 1.9 µm for CrN/AlN multi-layered hard coatings and 1.5 µm for CrN hard coatings, and the nominal ratios of H:L:W:B are 1:5:1:1. The width of ligaments (or bridges) next to the notch, b, was kept as small as possible, with a ratio of b/B of 0.92 which implies that each bridge has a relative width of 4% with respect to the cantilever width.

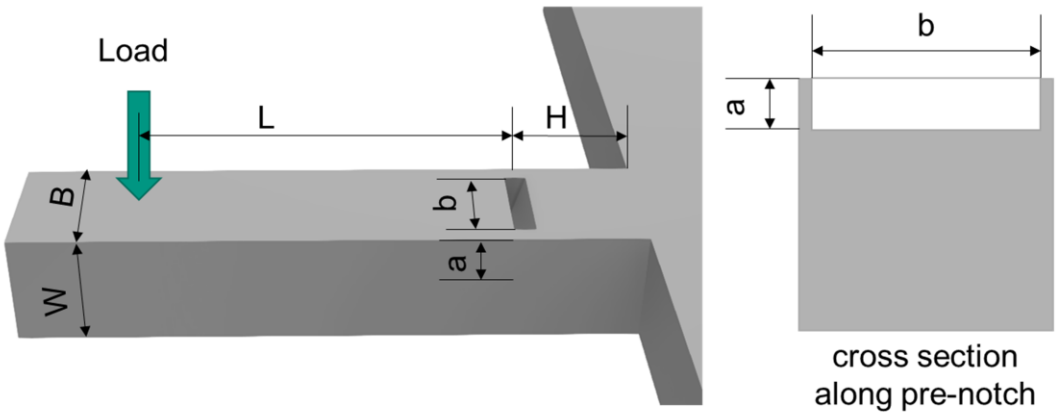

Figure 3.2. Geometry of a bridge notch cantilever. Reprinted from [123].

3.2.3 *In situ* SEM mechanical testing

In situ micromechanical fracture experiments were conducted to determine the fracture toughness of the hard coatings inside a SEM (Merlin Gemini II, Zeiss). A Hysitron PI 89 NG SEM PicoIndenter (Bruker) equipped with a 10 µm wide diamond wedge tip (Synton-MDP AG) was used in displacement-controlled mode with a displacement rate of 5 nm/s. The low load transducer of the PI 89 NG was used, which has a maximum load of 10 mN and noise floor of 0.4 µN.

3.2.4 Data analysis

The analytical solution for the conditional fracture toughness $K_{IQ,\,ref}$ in single cantilever bending tests under loads gives [29]:

$$K_{IQ,ref} = \frac{F_C L}{BW^{3/2}} f\left(\frac{a}{W}\right) \tag{3.1}$$

where F_C is the load at fracture, and $f(a/W)$ is a geometry shape factor for an ideally straight through thickness notch proposed by Matoy et al. [29] which is described as below.

$$f\left(\frac{a}{W}\right) = 1.46 + 24.36(a/W) - 47.21(a/W)^2 + 75.18(a/W)^3 \tag{3.2}$$

In this study, we use bridge notches that do not have a straight initial crack front (see Figure 3.2, right). According to the FEM simulations of Brinckmann et al. [95], the relative ratio between the stress intensity at the top of the bridges and the one at the center of the notch depends on the geometry of the bridges, which is described by the aforementioned correction factor. Using the correction factor, the conditional fracture toughness can be calculated from a micro-cantilever with a bridge notch. A detailed evaluation of the stress intensity factors in the different cantilever sections follows in Section 3.3.3.

Note that the conditional fracture toughness $K_{IQ,\,ref}$ as calculated from Equation (3.1) can be considered as fracture toughness K_{IC} for the samples investigated in this study.

3.3 Results

3.3.1 Direct observation of material bridge-failure

Figure 3.3a shows a SEM image of a representative CrN/AlN multi-layered micro-cantilever with a bridge notch before deformation. The load-displacement curve shows elastic loading in the beginning and three discontinuous points, denoted as B1, B2, and C (Figure 3.3b). By image-frame analysis of the *in situ* SEM video, it is found that B1 and B2 correspond to the failure of the bridges as shown in Figure 3.3d and e, respectively. Compared to the image before the bridge-failure (Figure 3.3c), arrested cracks are clearly visible after bridge failure, as pointed out by the white arrows in Figure 3.3d and e. Once the bridges break, the cantilever stiffness is reduced by 10% in average, and this stiffness reduction leads to a load drop at B1 and B2 as the displacement is constant. The length of the arrested crack in Figure 3.3e is measured to be 630 nm which is a little deeper than the depth of the FIB-notch which is 575 nm. Figure 3.3f shows an SEM image of the fractured surface; the CrN/AlN multi-layered coating has a dense morphology, and the columnar grain structure is visible. However, any noticeable features at the bridges which might originate from the crack arrest cannot be detected. For the fracture toughness evaluation in the following sections, the geometry and depth of the notch were measured from the fracture surface images.

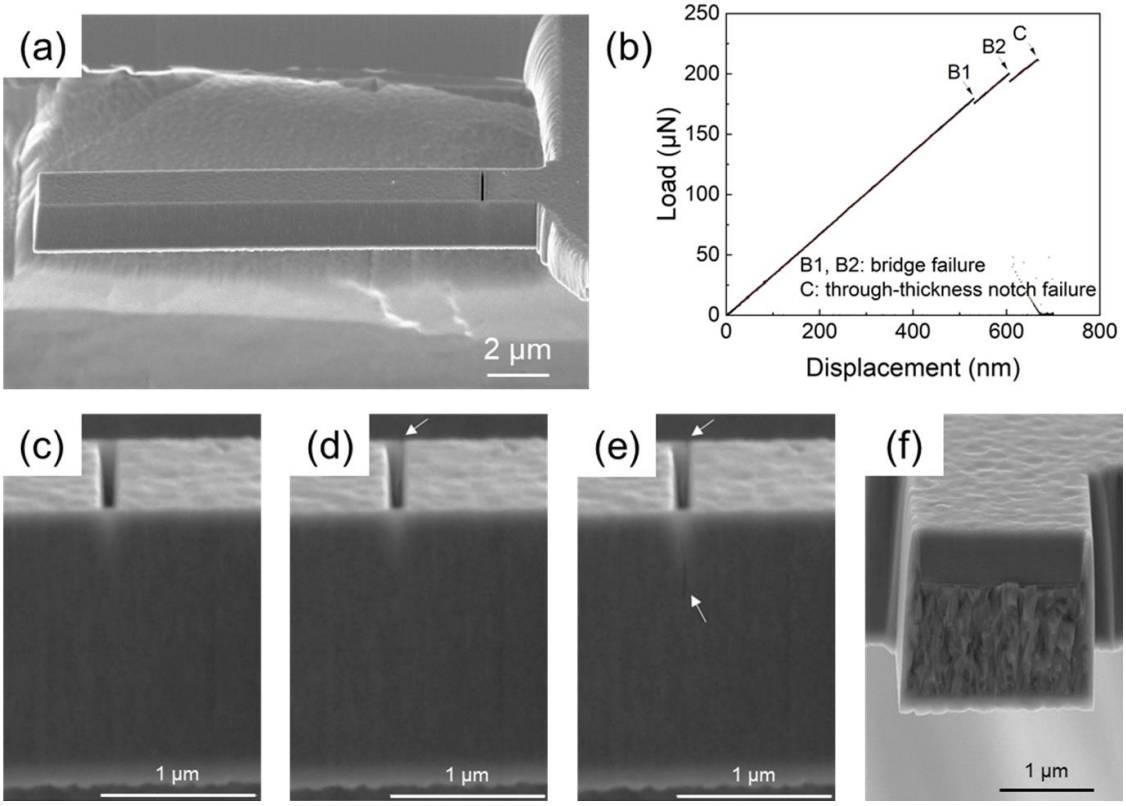

Figure 3.3. (a) Free-standing CrN/AlN multi-layered hard coating cantilever; (b) load-displacement curve showing elastic region and three discontinuous points. B1 and B2 are the bridge-failure points, and C is the cantilever fracture point; (c) SEM image of the cantilever before the bridge-failure; (d) SEM image showing failure of one of the bridges when the load reaches to B1; (e) SEM image at B2 showing the failure of the other bridge; (f) fracture surface of the cantilever after point C. Reprinted from [123].

3.3.2 Cumulative distribution of the maximum load

Similar experiments were performed on 11 cantilevers from CrN/AlN multilayer hard coatings (all load-displacement curves shown in Figure 3.4). For each test, the bridge failure and subsequently crack arrest before the final fracture were observed. And Figure 3.5 shows the cumulative distribution function of the load drops, the maximum load at B1, B2, and C point correspond to F_{B1}, F_{B2}, and F_C, respectively. We fit those data with a normal cumulative distribution function (CDF). The shades represent a 95% confidence interval. F_{B1}, F_{B2}, and F_C mean load is 177.1 μN, 202.5 μN, and 219.8 μN, and the standard deviation is 26.4 μN, 27.7 μN, and 12.8 μN, respectively.

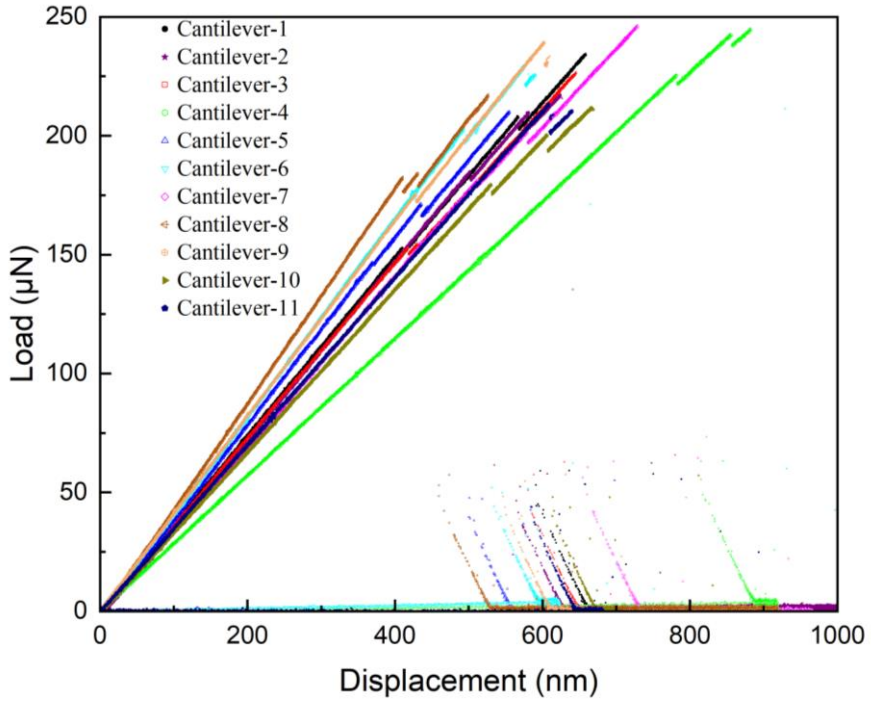

Figure 3.4. The load-displacement curves from 11 samples of multi-layered CrN/AlN multilayered hard coatings. Reprinted from [123].

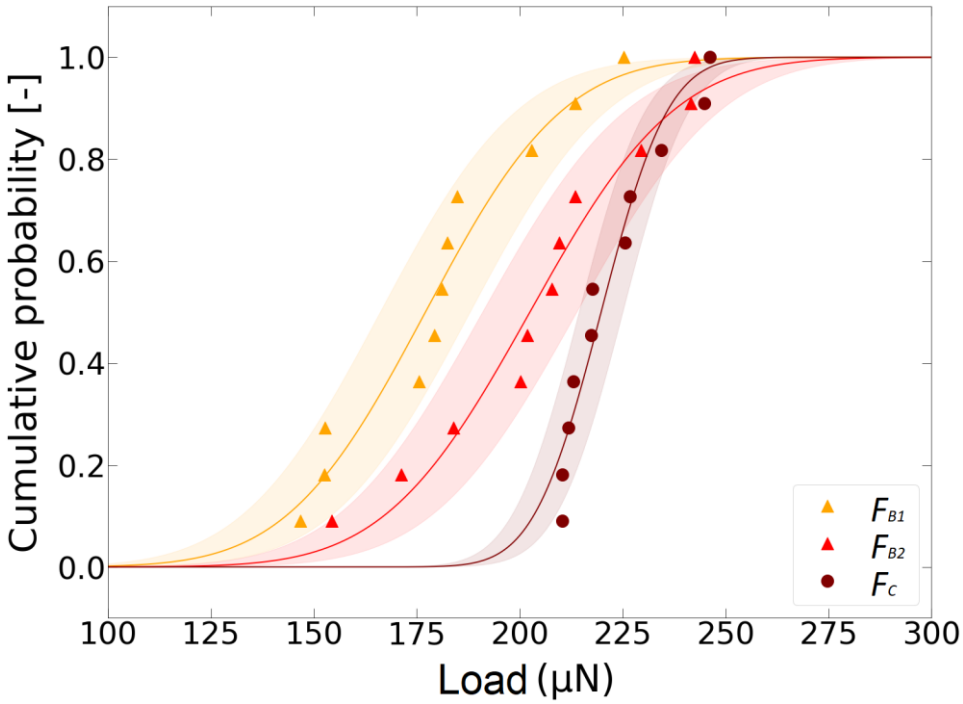

Figure 3.5. The normal cumulative distribution of load measured at B1, B2 and C for 11 CrN/AlN multi-layered cantilevers. The shade bands represent 95% confidence intervals. Reprinted from [123].

The key-findings are reflected in the cumulative probability curve: (i) The force for the complete cantilever failure, F_C, shows much less scatter compared to F_{B1} and F_{B2}, as the standard deviation is less than half of that of F_{B1} and F_{B2}. A possible scenario is that the complete failure of the cantilever is driven by natural cracks which are formed by bridge failure, thus F_C is less susceptible to FIB artifacts, for example, FIB damage and notch radius. (ii) The variation of the distribution in F_{B1} and F_{B2} are comparable. This suggests that the earlier bridge failure at B1, does not affect the second bridge failure event.

In most of cases, we observed two distinct load drops for each bridge failure at points B1 and B2. In rare cases, B1 and B2 occurred at the same load. Due to a possible asymmetry of the bridge shape on either side e.g. due to slight differences in bridge geometry, redeposition at the FIB-notch, different grain boundaries at the two bridges, and *et cetera*, B1 and B2 typically do not occur at exactly the same load. As soon as both bridges failed (see region after B2 in the load-displacement curve (Figure 3.3b)), the notch can be regarded as a through-thickness notch with a sharp natural crack at both sides (Figure 3.3d). The stress intensity, in this case, can be described by Equation (3.1), which means that the fracture toughness obtained from F_C at point C is $K_{IC} = K_{IQ,\,ref,\,C}$.

3.3.3 Cumulative distribution of the K_{IC}

From the maximum force before the fracture of bridges and cantilevers, F_{B1}, F_{B2}, and F_C, the critical stress intensity factors were calculated. In the case of the final fracture, F_C, we assumed a through-thickness notch although the exact geometry of the FIB-notch and the natural crack after the breaking of the bridges is more complex. In the case of bridge failure, we used a correction factor, f_{corr}, proposed by Brinckmann et al [95], which predicts the stress intensity at the top side of the bridge with respect to the one at the center of the FIB-notch. Then, we can calculate the bridge failure toughness K_{IC}^{*} using the same geometry factor for the cantilever by Matoy et al. [29] and correcting the relative ratio between stress intensity at the top of the bridge. It can be expressed as,

$$K_{IC}^{*} = K_{IQ,ref,B} \,/ f_{corr} \tag{3.3}$$

$$K_{IC}^{*} = \frac{F_B L}{B W^{3/2}} f\left(\frac{a}{W}\right) \,/\, f_{corr} \tag{3.4}$$

where F_B is the load (F_{B1} and F_{B2}) at points B1 or B2 in the load-displacement curve at bridge failure. f_{corr} depends on the geometry of the bridge notch, i.e. a/W ratio as well as $1 - b/B$. A detailed description of f_{corr} is followed in Section 3.4.1 and also in the Ref. [95]. After crack arrest, the notch can be regarded as a through-thickness notch with a sharp natural crack. Finally, we calculated the through thickness notch fracture toughness K_{IC} from the through-thickness notch (after crack arrest), and the bridge notch toughness K_{IC}^{*} from the bridge failure using Equations (3.1) and (3.4) as shown in Figure 3.6a. K_{IC} shows slightly higher fracture toughness while the scatter is less compared to K_{IC}^{*}. The same experiment (all load-displacement curves are shown in Figure 3.7) and analysis were conducted on a different material system, CrN monolithic coating, of which results are shown in Figure 3.6b. The similar trends can be seen, for example,

a higher through thickness fracture toughness K_{IC} from the complete fracture of the cantilever but with less deviation, compared to the bridge notch fracture toughness K_{IC}^{*}.

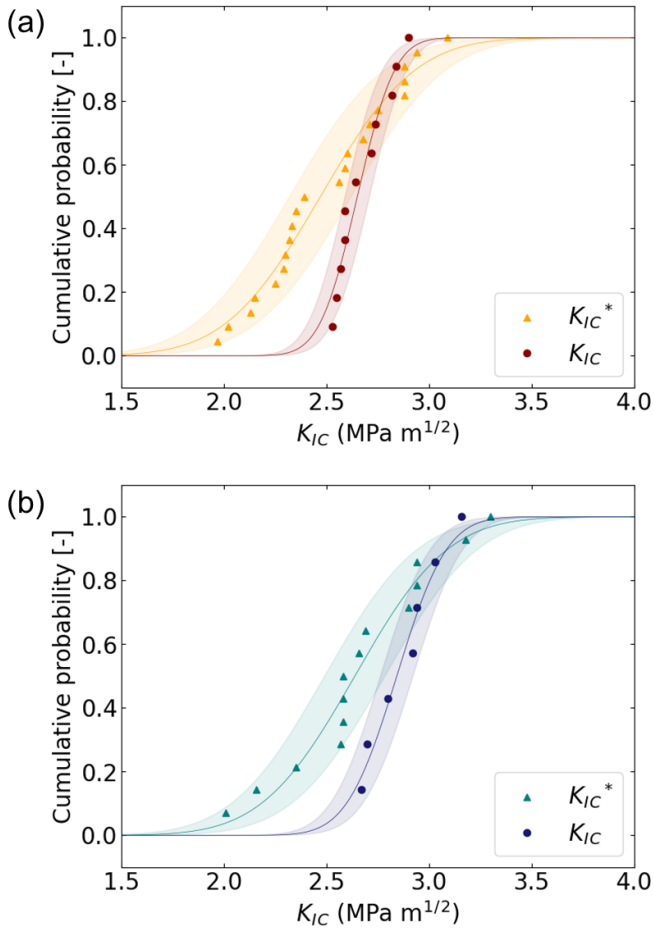

Figure 3.6. The cumulative distribution functions of the bridge notch fracture toughness K_{IC}^{*} and the trough thickness notch fracture toughness K_{IC} for (a) CrN/AlN multi-layered and (b) CrN hard coatings. Reprinted from [123].

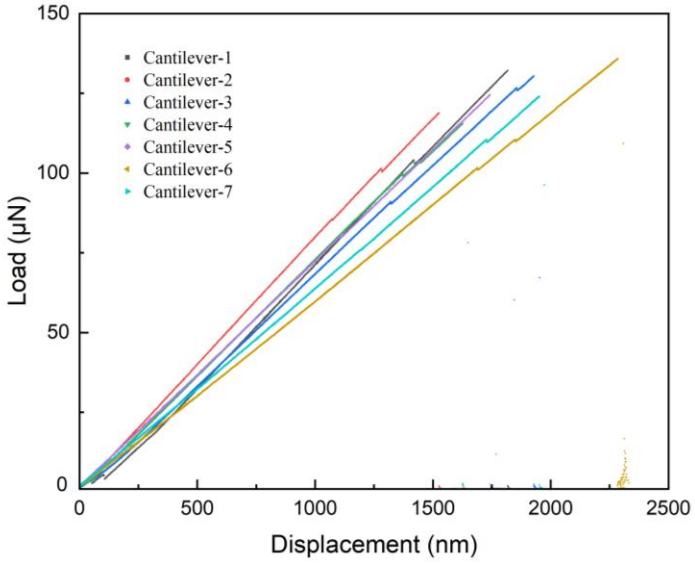

Figure 3.7. The load-displacement curves from 7 different samples of CrN hard coatings. Reprinted from [123].

The mean fracture toughness (K_{IC}^{*} and K_{IC}) for the CrN/AlN multi-layered hard coating is 2.5 ± 0.4 Mpa $m^{1/2}$ and 2.7 ± 0.1 MPa $m^{1/2}$, respectively. For the CrN hard coating, the mean fracture toughness is 2.6 ± 0.4 MPa $m^{1/2}$ and 2.8 ± 0.2 MPa $m^{1/2}$, respectively. The smaller scatters in the through thickness notch fracture toughness K_{IC} could originate from the sharper natural cracks after the bridge failure and fewer FIB artifacts.

The reason for the shift of the cumulative distribution can generally be analyzed by plotting the ratios of K_{IC}/K_{IC}^{*}, calculated for both hard coatings separately (see Figure 3.8). Even though the two sample systems had slightly different cantilever dimensions due to different coating thicknesses, the cumulative distribution of the ratio between K_{IC} and K_{IC}^{*} is almost identical. The mean of K_{IC}/K_{IC}^{*} is 1.07 ± 0.15 and 1.07 ± 0.17 for CrN hard coating and CrN/AlN multi-layered hard coatings, respectively. Consequently, the fracture toughness measured from the final fracture of the cantilever is 7% higher than that measured from the bridge failures. The possible reasons are discussed in Section 3.4.3.

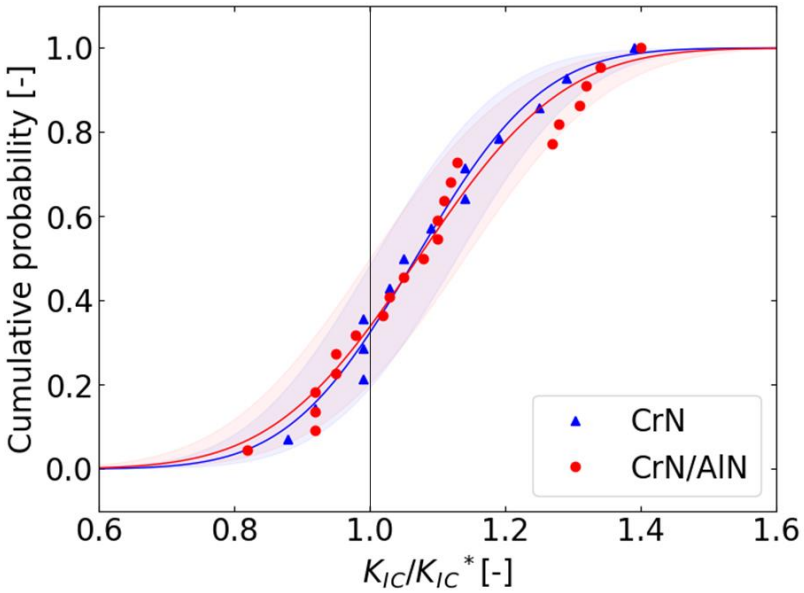

Figure 3.8.The cumulative distribution function of K_{IC}/K_{IC}^* for the CrN hard coating and the CrN/AlN multi-layered hard coating. Reprinted from [123].

3.4 Discussion

Matoy and co-workers [29] proposed the bridge notch geometry in order to form a natural crack in small scale cantilevers, which is less prone to FIB artifacts. Nevertheless, to the best of our knowledge, the intended sequence of bridge-failure, crack propagation of a sharp crack in the bridges, crack arrest, and final fracture of the micro-cantilever has never been experimentally reported before. In this section, we will first discuss the prerequisites for crack arrest in micro-cantilevers. Subsequently, we will discuss differences between the obtained fracture toughness at bridge-failure and at final fracture, differences in their scatter and finally on implications for the small scale testing community.

3.4.1 How to promote crack arrest?

In bridge notch cantilevers, fracture always initiates at the top inner corner of the bridge notch [95], where the stress intensity is highest. To observe subsequent crack arrest, the stress intensity at the bridge top needs to be larger than the stress intensity in the later formed through-thickness notch (after crack arrest) at the same displacement (or load, depending on the intrinsic behavior of the testing device). Using FEM modeling, Brinckmann and co-workers [95] mapped the ratio of the stress intensity of bridge notches and the one of through-thickness notches (see Figure 3.9). This ratio strongly depends on the bridge notch geometry, i.e. on the a/W ratio as well as on the relative size of the bridge notch ($1\text{-}b/B$). Stress intensity ratios larger than 1 would result in crack propagation without crack arrest because the stress intensity at the through-thickness notch would already exceed the critical value in the event of the bridge-failure.

On the other hand, when the stress intensity ratio f_{corr} (as in Figure 3.9) is smaller than 1, the crack will start from the top side of the bridge because of higher stress intensity, and arrest near the FIB-notch root. It is because the stress intensity at the through-thickness notch (after crack arrest) is smaller than the one at the bridge part, therefore a load increase is required to propagate the crack further. To summarize, bridge notch geometries in the lower right corner of Figure 3.9 promote crack arrest while geometries in the upper left corner show continuous crack propagation and do not allow for the measurement of B1 and B2. Generally, to observe crack arrest, an a/W ratio higher than 0.2 is required and notches with very thin bridges are recommended (see Figure 3.9).

The bridge geometry for the presented cantilevers is around $a/W = 0.3$ and $(1\text{-}b/B) = 0.07$, which is shown by the black cross on the white rectangle in Figure 3.9 resulting f_{corr} of ~0.9. Therefore, crack initiation at the bridge top and crack arrest after forming a through-thickness notch is expected and observed. It shall be noted that the sensor noise of less-sensitive indenter systems might hide the load drops caused by bridge-failure (points B1 and B2 in Figure 3.3b). In our case, the average load drops at the bridge failure was a few µN.

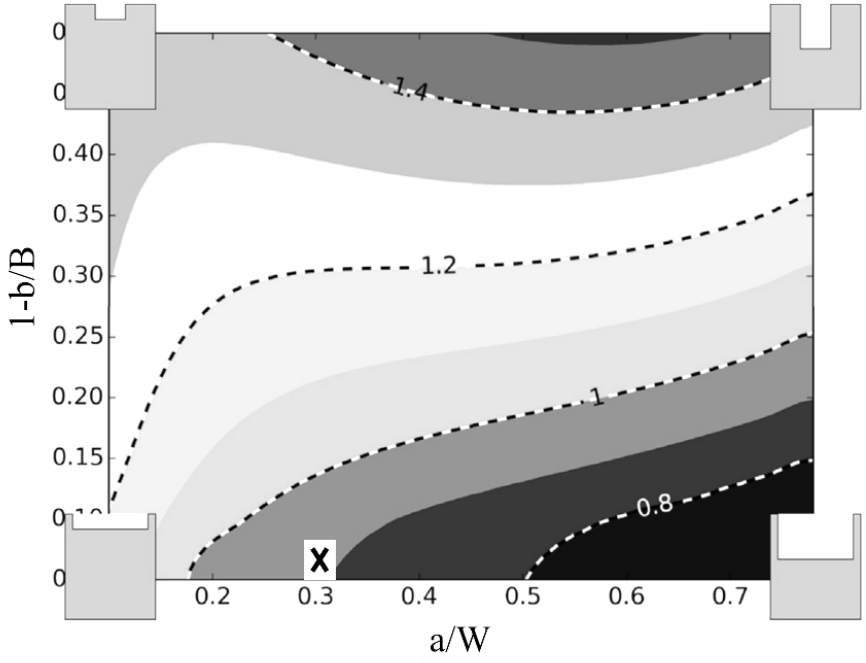

Figure 3.9. Stress intensity factor in the absence of a bridge (according to the reference Equation (3.1)) divided by the average stress intensity top half of the bridge. *a/W* is the ratio of the reference crack length and the cantilever thickness. *1-b/B* is the representation of the width of two bridges. The white rectangle with an X indicates the geometry chosen for cantilevers investigated in this study. Reproduced with permission from Brinckmann et al. [95]. Reprinted from [123].

3.4.2 Computing multiple values for the fracture toughness based on crack arrest

There are two important implications of the bridge failure. Firstly, as previously mentioned, the natural cracks from the bridge failure significantly reduce scatters in the K_{IC} improving accuracy of the data. But also, two additional fracture toughness values can be measured for each failure of the bridges. As micro mechanical testing is always subjected to an experimental scatter due to its sensitivity to local inhomogeneous of the microstructure, a statistical analysis is required. Therefore, two additional data points from a single experiment can help to improve the statistics thus the accuracy of the results from micro-cantilever fracture experiments.

To obtain multiple fracture toughness values from one cantilever, the position of the crack initiation needs to be correlated to the load at the onset of crack propagation to compute the correct stress intensity. As stated above, in bridge notches crack always initiates at the inner top corner of the bridge notch [95], as also observed in our experiments. The bridge notch fracture toughness K_{IC}^{*} can therefore be obtained from Equation (3.4) using the load F_{B1} and F_{B2}. Subsequently, crack arrest after bridge-failure forms a through-thickness notch (with two natural cracks at the side and the FIB-milled notch in the center), at which the final fracture occurs. The through-thickness notch fulfils the geometric requirements assumed in the FEM-based stress intensity calculations from Matoy et al. [29], and therefore, the through thickness notch fracture toughness K_{IC} can be calculated based on Equation (3.1) and the load at final fracture, F_C.

3.4.3 Possible reasons for differences in K_{IC} and K_{IC}^{*}

The collective assessment of K_{IC} and K_{IC}^{*} reveals quantitative differences in the brige notch fracture toughness and the through thickness notch fracture toughness (see Figure 3.8). The toughness obtained at the final fracture is 7% higher than the one obtained from bridge-failure observed from two different material systems (Figure 3.8). Two main sources for these discrepancies are identified:

(i) The local stress intensity factor as calculated from FEM models does not match the real one due to the geometry of the real sample.

(ii) The material in the thin bridges is altered by the Ga^{+} ion beam differently than in the sharp crack being present after crack arrest.

The FEM-based stress intensity calculations assume a vertical bridge notch with sharp corners [95]. In contrast, due to the small dimensions of the bridges which are typically less than 100 nm, a certain edge-rounding occurs, and FIB taper forms. Both effects would reduce the stress intensity in the real cantilever with respect to the ideal one modeled in FEM. Therefore, while the effect of geometric imperfections of the bridge notch is indisputable, it cannot explain the lower bridge notch fracture toughness as observed in our experiments (see Figure 3.6 and Figure 3.8).

Consequently, we argue that the FIB-damage in the material bridges is the main reason for the observed discrepancy. At bridge-failure, stress localizes at the top region of the bridge which is most prone to FIB milling effects, because the Ga^{+} ion damage is expected to propagate tens of

nanometers into the sample [115]. In contrast, the arrested crack which gives rise to the final fracture is a naturally formed, sharp-crack far from the region associated with FIB damages. For most materials, we assume that FIB damage results in embrittlement, rather than toughening, which would be in line with our results presented in Figure 3.8.

Let us finally note that the crack driving load in a FIB-milled through-thickness notch (shown in the Figure 3d in Ref. [95]) is largest in the sample center, where plane strain conditions are present. In this region, we expect a FIB-milled notch to have many different FIB artifacts, such as a finite notch root radius, FIB-induced crystal defects, residual stresses and *et cetera*. However, due to the slight advance of our natural crack (the surface crack is slightly longer than the FIB-milled pre-notch) and its superior sharpness, we speculate that the final fracture occurs from the two sharp cracks at the side of the specimen and not in the FIB-affected center of the notch, then the natural cracks propagate to the center of the specimen.

3.4.4 Reasons for the increased scatter of K_{IC}^{*} compared to K_{IC}

It is noted that the fracture toughness from bridge-failure shows substantially more scatter than the one from the newly formed through-thickness notch (compare the behavior of K_{IC} and K_{IC}^{*} in Figure 3.6). We address this increased scatter by imperfections of the top region of the bridge notch: unavoidable FIB taper angle and corner rounding (see Section 3.4.3) result in a non-ideal bridge geometry (see Figure 3.3f) that is not fully reproducible from one experiment to the other. These bridge geometry deviations are one reason for the increased scatter of the fracture toughness obtained by bridge-failure.

We believe that another possible reason is the relatively low material volume subjected to high stress intensities compared to the final through-thickness notch: while in bridge-failure we essentially see two points of high stress intensity (at the inner corner of the bridge, see [95]), the entire through-thickness notch is subjected to high stress intensities with small variations along the notch. Even when the final cracking initiates from the natural sharp cracks at the side of the specimens only, the volume being subjected to high stress intensities is substantially larger than in the two hot spots in the case of the bridge notch. The small area subjected to high stress intensities gives rise to a large scatter, as well-understood from weakest link statistics in ceramic materials [160].

3.4.5 Implications for the FIB-based measurement of micro-cantilever fracture toughness

The observation of crack arrest after crack initiation at the bridge notch has at least two implications for the measurement of micro-cantilever fracture toughness.

1) The strategy of forming a natural crack based on the bridge notch geometry, as proposed by Matoy et al. [29], is well-suited to reduce the effect of FIB-damage. Our results indicate that the toughness in a naturally formed crack is larger than the one obtained from crack initiation at the FIB-affected regions. Please note that this argument will only hold for knock-on damage, for example, the formation of stacking faults or dislocations [161], typically

observed tens of nanometers from the surface [115], but does not hold for materials exhibiting extensive Ga^+ segregation to interfaces. For example, liquid metal embrittlement by Ga in Al is a fast process and even a small amount of implanted Ga atoms will segregate at grain boundaries far from the milled area and will change the mechanical properties of Al samples [115].

2) To obtain a valid estimation of the fracture toughness by bridge notch cantilevers, the location of crack initiation needs to be identified, because the stress intensity at the bridge notch and the through-thickness notch varies strongly [95]. If bridge-failure (B1 and B2 in Figure 3.3) and final fracture (C in Figure 3.3) can be observed *in situ* and in the load-displacement curve, the correct geometry factors can be used with confidence. In all other cases, it remains unclear if the bridge failed at the maximum load or the sharp crack gave rise to final failure. Consequently, if the imaging resolution of the *in situ* device, the load resolution of the indenter or its stiffness prevent an identification of the points B1, B2 and C, it is recommended to target bridge geometries with f_{corr} close to but smaller than 1, because the stress intensities at the bridge and the through-thickness notch after bridge failure are identical. To directly observe the bridge-failure and measure the corresponding load at the event, a f_{corr} smaller than 1 is recommended because it allows for the observation of a natural crack without / with less FIB artifacts.

3.5 Conclusions

Within this work, the fracture toughness of two different hard coatings was assessed by designing very thin bridge notches in a micro-cantilever using an *in situ* SEM indenter equipment with high stiffness and low noise. The following conclusions can be drawn:

- The first experimental observation of cracking at the bridge notch during single cantilever bending tests on multi-layered CrN/AlN hard coatings and CrN hard coatings is presented.
- The through-thickness notch (after crack arrest) fracture of the cantilever occurs at a naturally sharp crack and therefore is less prone to FIB-milling artifacts.
- Up to three fracture toughness values were obtained from a single experiment: two bridge notch fracture toughness values from the bridge-failure and one through thickness notch fracture toughness from the final cantilever fracture. The toughness values obtained from bridge-failure are, on average, 7% lower than the ones obtained from the final fracture of the cantilever, which may be due to the non-perfect matching of the FEM model and FIB artifacts.
- Recommendations for the testing strategy and the cantilever geometry are provided. For a direct observation of bridge failure and the measurement of the corresponding load, a f_{corr} less than 1 is required. This ensures that the maximum load occurs at the final failure of the through-thickness notch after crack arrest.

4 Columnar grain boundaries are the weakest link in hard coatings: insights from micro-cantilever testing

Chapter 4 is based on a published journal article.

Y. Zhang, M. Bartosik, S. Brinckmann, U. Bansal, S. Lee and C. Kirchlechner, Columnar grain boundaries are the weakest link in hard coatings: insights from micro-cantilever testing, Mater. Res. Lett. (2025) 1-9. https://doi.org/10.1080/21663831.2025.2560526

A detailed description of the contributions of all the researchers involved in experiments and interpretations can be found in the appendix.

4.1 Introduction

Hard coatings have been widely used for various industrial applications including cutting tools, protective layers for aerospace components, and wear-resistant surfaces for mechanical parts [1, 35, 36]. These coatings possess superior hardness, wear resistance, and thermal stability, thus effectively protect the metallic substrates and components [162-164]. However, one of their critical limitation is brittleness, more specifically, their limited fracture toughness. It is widely recognized that microstructural features such as grain boundaries (GBs) or point defects and their density can play a detrimental role in fracture toughness governing crack nucleation and propagation [28, 165, 166]. Typically, hard coatings, composed of oxides, nitrides, or carbides, are mostly fabricated using physical vapor deposition (PVD) method, however, PVD-grown coatings typically exhibit a columnar grain microstructure characterized by grain sizes below a few hundred nanometers, which leads to a high density of GBs [9, 10]. This results in a high density of GBs, which can further degrade fracture toughness [32, 33, 90, 167-175]. For example, our recent study showed that the orientation of columnar grained microstructure with respect to the loading direction influences the crack propagation path thus fracture toughness as well [172].

Although GBs are widely recognized as the weak links in hard coatings and there have been many attempts to improve their mechanical properties via so-called GB engineering, the fundamental understanding of their quantitative impact on fracture toughness remains limited. Previous studies have explored the influence of GBs on the fracture toughness of hard coatings by comparing different hard coatings with different microstructures and GB density [176-178]. For instance, the fracture behavior of α-Al_2O_3 coatings was investigated through micro-cantilever bending tests, which reported slightly enhanced fracture toughness in single crystal coatings compared to polycrystalline ones [178]. Conversely, improvements in mechanical properties through GB engineering have also been reported in zirconia coatings [177]; the polycrystalline samples showed better crack resistance under nanoindentation compared to a single crystal.

One of the challenges to quantitatively measure the effect of GBs on fracture toughness is that various factors, besides GBs, influence the (apparent) fracture toughness of hard coatings, such

as crystallographic texture, residual stress, off-stoichiometry, and elemental segregation. These intrinsic properties are strongly affected by the deposition process, where even small variations in the deposition parameters can significantly change the properties of the coatings [130, 179]. Consequently, synthesizing model systems that differ only in their content of columnar GBs while maintaining identical chemical and defect structures is extremely challenging, which has hindered quantitative insights into their effect on fracture toughness.

To address this gap, we conducted *in situ* SEM micro-cantilever fracture testing on CrN/AlN hard coatings. Two key approaches were used to investigate the influence of GBs on the fracture toughness of the nitride hard coating. Firstly, a unique microstructure was introduced to the coating by controlling misfit strain: an epitaxial and single crystal in the bottom of the coating and the top part with a columnar-grained microstructure. Secondly, instead of a conventional through-thickness notch, a bridge notch with a thin side ligament was introduced to prepare micro-cantilevers. This approach minimizes FIB-induced artifacts and allows fracture toughness to be measured from small volumes, specifically from different regions of the coating with distinct microstructures. By combining these two approaches, we were successfully able to isolate the contribution of GBs to the fracture toughness from several other factors which could alter fracture toughness, and ultimately quantify the influence of the columnar GBs on the fracture toughness.

4.2 Materials and methods

CrN/AlN multilayered coatings, consisting of alternating layers of nominally 4 nm CrN and 2 nm of AlN, were deposited on MgO (100) and Si (100) substrates, respectively (detailed deposition processes can be found in our previous study [123]). Prior to deposition, the substrates were ultrasonically cleaned in acetone and ethanol, respectively. They were then mounted in an AJA ATC-1800 ultra-high vacuum deposition system, where they underwent thermal cleaning at 550 °C for 30 minutes in a vacuum, followed by 5–10 minutes of Ar ion etching at 500 °C. The Cr (diameter three-inch, purity 99.95%) and Al (diameter three-inch, purity 99.99%) targets were sputter-cleaned behind closed shutters for 5 minutes before film growth. The coatings were subsequently grown in pulsed DC mode (100 kHz pulse frequency, 1 μs pause). To ensure a dense morphology, 300 W was applied to the Cr target and 500 W to the Al target in a mixed N_2/Ar gas atmosphere (12 sccm / 8 sccm flow rate ratio) at a total pressure of 0.2 Pa, combined with a -70 V DC bias applied to the substrates. The substrates were continuously rotated at approximately 0.5 Hz during deposition. The multilayered structure was achieved through computer-controlled opening and closing of mechanical shutters at specific intervals. The total thickness of the CrN/AlN multilayered coatings was 1.9 μm.

The microstructure of the coating was characterized firstly using SEM (Merlin Gemini II, Zeiss), focused ion beam (FIB, Crossbeam 550L, Zeiss) and transmission electron microscopy (TEM, Titan Themis 300, Thermo Fisher Scientific) to study their grain structure, orientation relationship and chemical distribution. Subsequently, micro-cantilevers with square cross-sections were fabricated using FIB milling with 30kV Ga^+ ions and ion currents of 15 nA, 3 nA, 700 pA, and 50 pA for stepwise milling. The dimensions of the micro-cantilevers were kept consistent with an L:W:B ratio of 5:1:1, where L is the distance to the loading point from a notch, W is the thickness, and B is the width of the micro-cantilever as shown in Figure 4.1. As the coating thickness, W, is

pre-determined to 1.9 µm by the coating synthesis, their width was adjusted to have a square cross-section.

A bridge notch rather than a through-thickness notch was employed. As demonstrated in our previous studies [123, 180], with a bridge-notch, fracture typically initiates from the bridge failure, where an atomically sharp crack is generated via crack arrest, thereby reducing the scatter in the measured fracture toughness values. In the present work, the bridge notch geometry was specifically utilized to enable the determination of apparent fracture toughness in local regions of the coatings. For this purpose, a notch with a depth, *a*, ranging from 20–30% of the thickness *W* was introduced using a 20 pA and 30 kV ion beam. The width of the notch, *b*, was chosen to yield a *b/B* ratio of 0.92 to maximize stress localization and promote bridge-failure with subsequent crack arrest. Finally, each of the ligaments (or bridge) was a width of less than 100 nm.

The cantilevers were prepared in two geometries with different orientations relative to the coating growth direction, as shown in Figure 4.1. In one case, the loading direction was parallel to the growth direction (Figure 4.1a and c), whereas in the other case it was perpendicular (Figure 4.1b and d)).

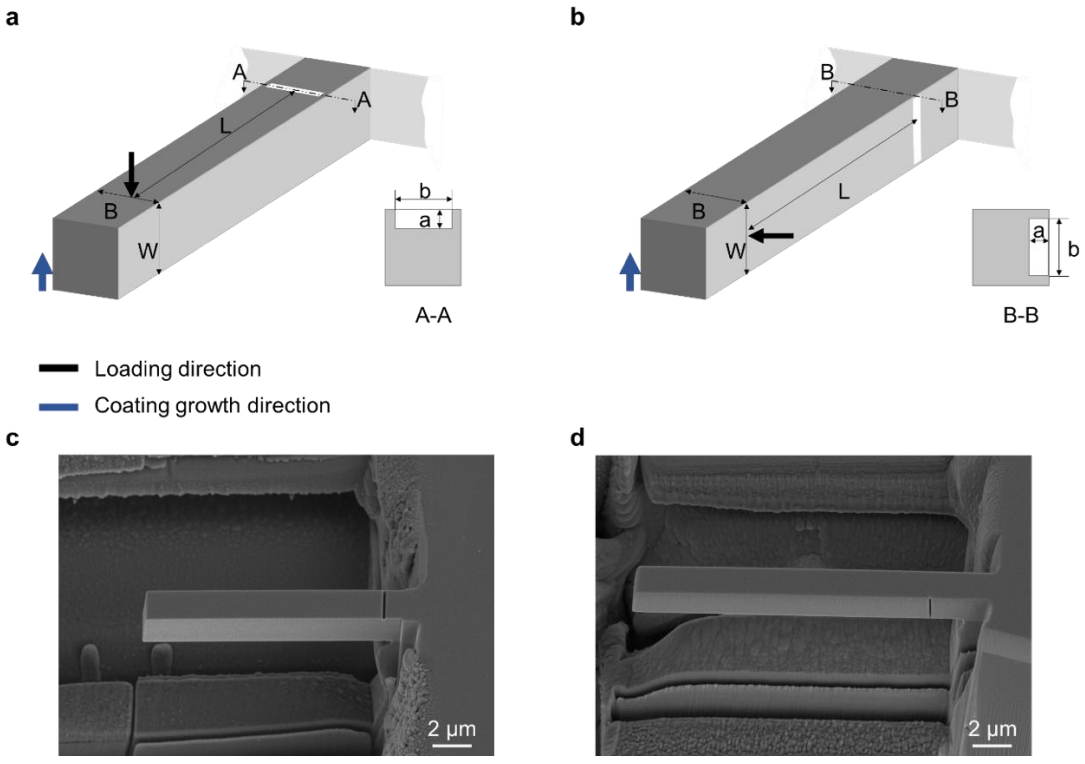

Figure 4.1. (a, b) Schematics of the cantilever geometries and their orientation relative to the loading direction. (c, d) Representative SEM images of each geometry. In (c), the loading direction is parallel to the coating growth direction (i.e., along the columnar grain microstructure), whereas in (d) it is perpendicular to the growth direction. Reprinted from [96].

Micro-fracture experiments were performed *in situ* using a nanoindenter (Hysitron PI-89, Bruker) equipped with a 10 µm diamond wedge tip (Synton-MDP AG) in an SEM (Merlin Gemini II, Zeiss). All tests were conducted in a displacement-controlled mode at 5 nm/s using a transducer

with a maximum load of 10 mN and a noise floor of 0.4 μN. The fracture toughness, K_{IC}, is evaluated at the point of final failure of the specimens. At this point, the two bridges had already failed, and the final fracture occurred at the arrested natural crack [123, 180]. This protocol follows Matoy's pioneering work introduced in [29],

$$K_{IC} = \frac{F_C L}{BW^{3/2}} f\left(\frac{a}{W}\right) \tag{4.1}$$

where, F_C is the load at final fracture, and $f\left(\frac{a}{W}\right)$ is a geometry shape factor defined by:

$$f\left(\frac{a}{W}\right) = 1.46 + 24.36(a/W) - 47.21(a/W)^2 + 75.18(a/W)^3 \tag{4.2}$$

The fracture toughness K_{Ic}^{*} represents the fracture toughness at bridge-failure. It can be calculated using the geometry correction factor f_{corr} [29, 95, 123]:

$$K_{IC}^{*} = \frac{F_B L}{BW^{3/2}} f\left(\frac{a}{W}\right) / f_{corr} \tag{4.3}$$

where, F_B represents the load at bridge-failure. Note that two additional fracture toughness values can be obtained per micro-cantilever from each bridge failure, for those cases where a clear load drop, bridge failure and crack arrest are observed *in situ*.

4.3 Results and interpretation

A CrN/AlN multilayer coating with individual layer thicknesses of 4 nm (CrN) and 2 nm (AlN) was deposited on both Si and MgO substrates under the same conditions. Despite the identical deposition process, the coatings exhibited distinct microstructures. Firstly, the coating on a MgO (100) substrate had two distinct microstructures within the film, as schematically depicted in Figure 4.2a: a roughly 500 nm-thick epitaxial structure is formed at the bottom (see Figure 4.2b and d), which is followed by a columnar-grained microstructure (compare Figure 4.2b and c). The column diameter in the upper part of this coating is about 70 nm. In contrast, the coating deposited on a Si (100) substrate exhibited only a columnar-grained structure with comparable columnar diameter (approximately 100 nm) of the one on a MgO substrate, see Figure 4.3. Hereafter, the coating on MgO will be referred to as columnar grain/epitaxial (cg/epi) coating, while the one on Si will be referred as columnar grain (cg) coating.

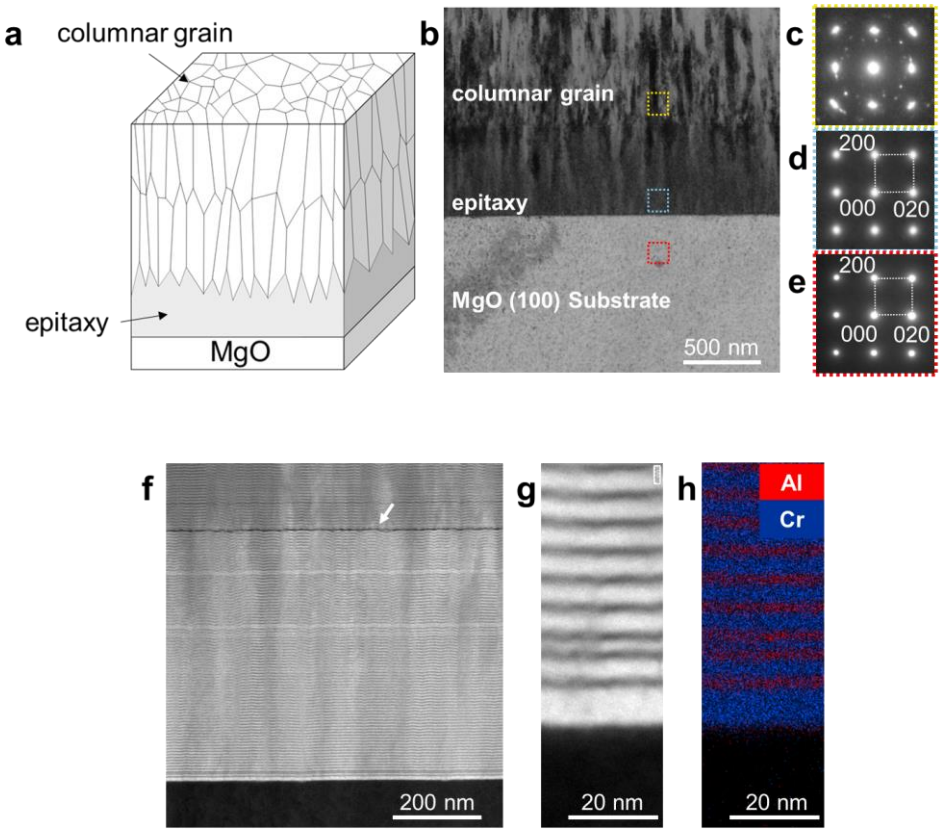

Figure 4.2. Microstructure investigation of cg/epi-coating. (a) Schematic drawing of the cg/epi-coating with an epitaxial layer between the columnar-grained microstructure and the MgO (100) substrate. (b) TEM image of the cross-section of the cg/epi-coating. Selected area diffraction patterns from (c) the columnar-grained microstructure, (d) the epitaxial structure, (e) and the MgO (100) substrate. (f) HAADF-STEM image of the epitaxial part and the interface with MgO substrate. (g) HAADF-STEM image at higher magnification on the epitaxial part showing CrN and AlN multi-layered structure and (h) its corresponding EDS maps. The target thickness of CrN and AlN layers were 4 and 2 nm, respectively. Reprinted from [96].

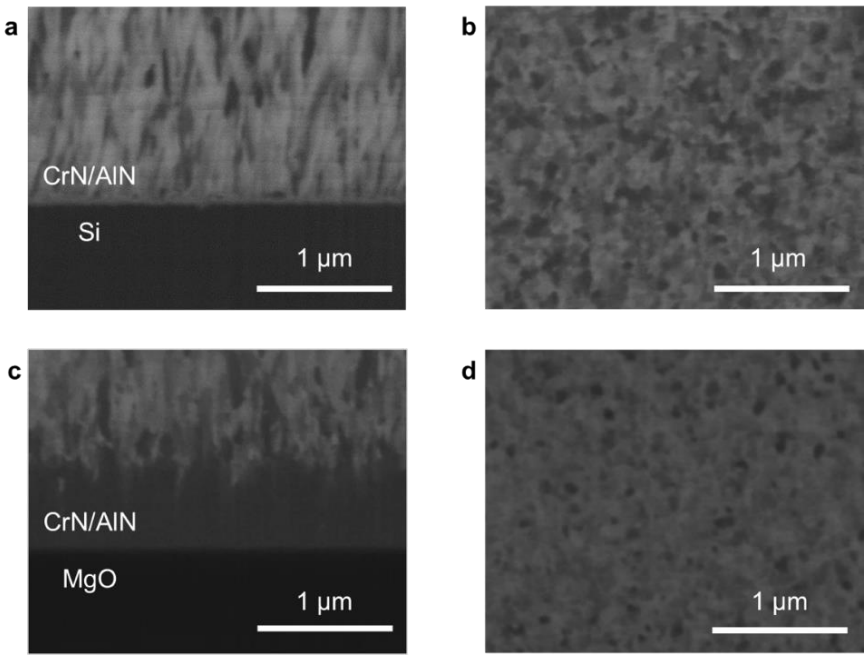

Figure 4.3. Comparison of the two coatings deposited on Si (top row, fully columnar structure) and MgO (bottom row, partly epitaxial). The FIB channeling contrast images is used in all these images. Cross-section images are presented to the left, while the right micrographs are top-view images. (a) and (b) Microstructure of CrN/AlN on Si (100) (cg-coating, fully columnar). (c) and (d) Microstructure of CrN/AlN on MgO (100) with an epitaxial layer (cg/epi-coating). After an epitaxial region a clear transition to a columnar microstructure, which is comparable to the one on Si, is formed in case of the CrN/AlN on MgO(110). Reprinted from [96].

TEM selected area electron diffraction patterns from each part of the cg/epi-coating (Figure 4.2c–e) showed the (100) cube-on-cube orientation relationship between the MgO substrate and the epitaxial part in Figure 4.2d, which is largely maintained in the upper part as well. Scanning transmission electron microscope (STEM) high-angle annular dark-field (HAADF) imaging and energy dispersive spectroscopy (EDS) mapping reveal the layered microstructure of the coating (Figure 4.2f–h). Faulted layers as indicated by an arrow in Figure 4.2f, show darker contrast compared to other layers suggesting lower atomic density. Since it is located near the point where the transition from the epitaxial to columnar microstructure occurred, it is speculated that due to the accumulated strain energy from the epitaxial growth, the faulted layer was formed and altered the microstructure of the layers deposited afterwards. Further comparisons of the columnar grain structures in the cg- and cg/epi-coatings, including HAADF-STEM imaging, electron diffraction, and STEM-EDS composition analysis, are provided in Figure 4.4.

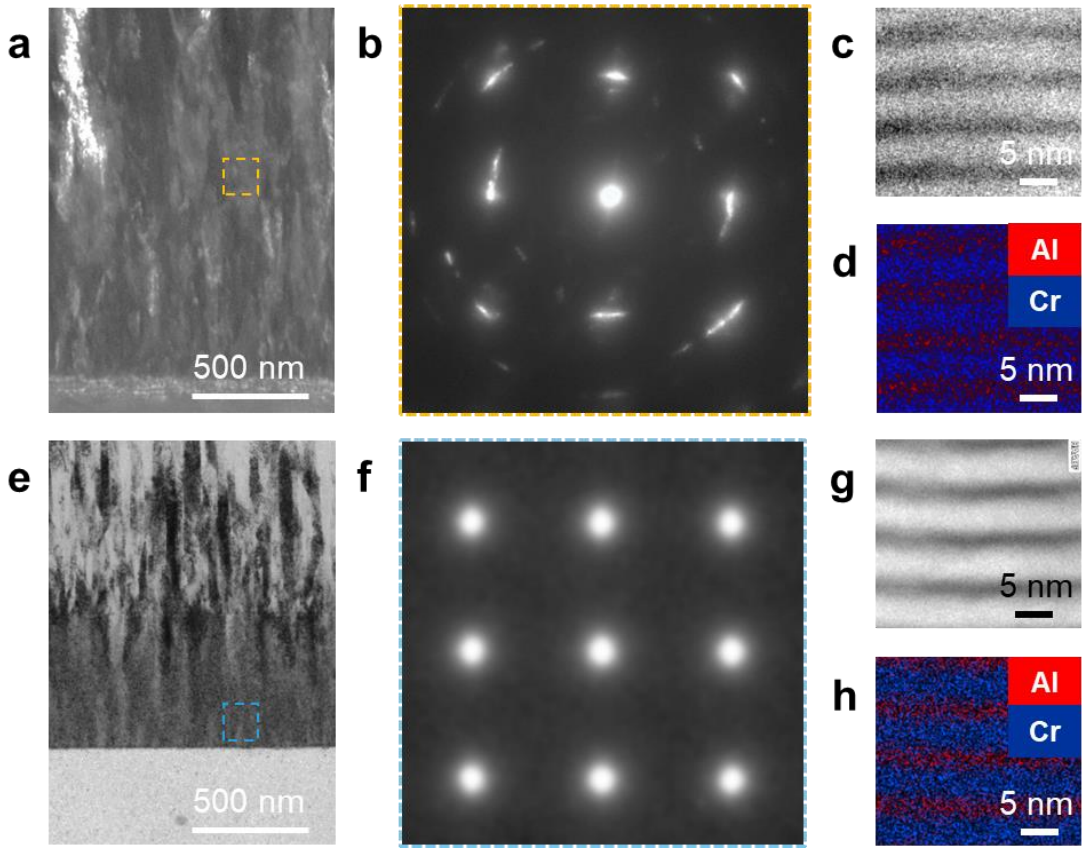

Figure 4.4. Microstructure and chemical analysis on the cg-coating (a–d) and cg/epi-coating (e–h). (a) and (e) TEM images of the cross-section of the coatings. The selected area electron diffraction patterns (b) from the columnar grain structures on the cg-coating and (f) epitaxy structure on the cg/epi-coating. (c) and (g) HAADF-STEM images of each coating for EDS mapping and corresponding maps are shown in (d) and (h), which display the multilayered structure, i.e., alternating CrN and AlN. Reprinted from [96].

The influence of the epitaxial structure on the fracture toughness of the coating was investigated firstly by comparing the fracture toughness of cg/epi and cg-coating. A representative SEM image of the experimental setup, a cantilever and a wedge tip, is shown in Figure 4.5a. In both samples, the load-displacement curves, 8 curves from cg/epi-coatings (Figure 4.5b) and 11 curves from cg-coatings [123], exhibited linear elastic behavior until bridge failure (points B1 and B2) with subsequent crack arrest. From each of the three load drops (B1, B2, and C), fracture toughness values can be determined. For the first two drops corresponding to bridge failure, the apparent fracture toughness $K_{IC}{}^{*}$ was obtained using Equation (4.3), while for the final fracture event (C), K_{IC} was calculated using Equation (4.1). Representative load-displacement curves are shown in Figure 4.6.

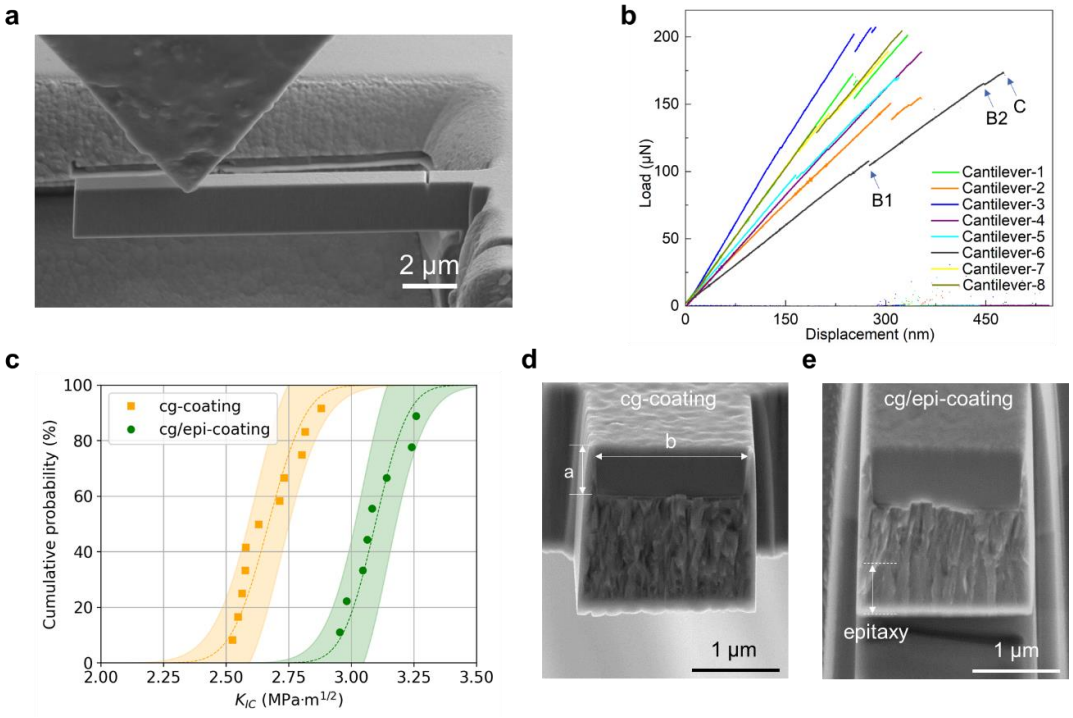

Figure 4.5. (a) Free-standing micro-cantilever of the cg/epi-coating. (b) Load-displacement curves from 8 micro-cantilever bending tests of the cg/epi-coating. The failure of the material bridges, B1 and B2, and the final fracture, C, are indicated on one representative curve. (c) Cumulative distribution of the fracture toughness, K_{IC}, for the cg/epi-coating and cg-coatings at point C. The cg/epi-coating with epitaxial structures exhibited higher fracture toughness. The shaded band indicates 95% confidence intervals of the normal distribution fitting. (d) SEM image of the fracture surface of the cg-coating and (e) the cg/epi-coating. Intergranular fracture is visible in the cg-coating and the top part of the cg/epi-coating. Reprinted from [96].

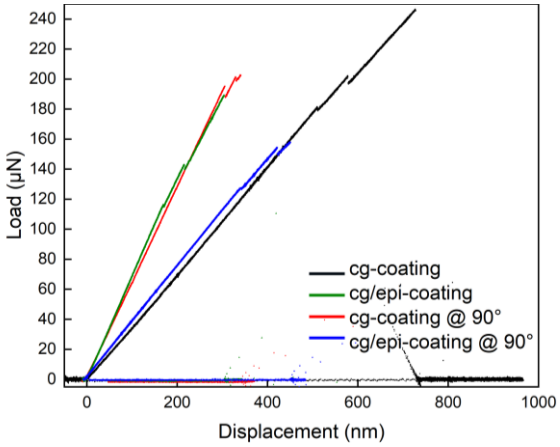

Figure 4.6. Representative load-displacement curve for each test type, with the load directions both parallel and perpendicular (denoted as 90 °) to the coating growth direction. Reprinted from [96].

Cumulative probability distribution of the fracture toughness, K_{IC} calculated using the final failure (F_C), clearly demonstrates that K_{IC} of cg/epi-coating is higher than that of cg-coating as shown in Figure 4.5c. The mean K_{IC} value is 3.1 ± 0.1 MPa $m^{1/2}$ for cg/epi-coating while 2.7 ± 0.1 MPa $m^{1/2}$ [123] for cg-coating with the standard deviation representing the scatter band. The shaded region in Figure 4.5c represents the normal distribution fit with its 95% confidence band, and the detailed data used for the calculation are provided in Table 4.1. Although the epitaxial part was located at the bottom of the coating and comprised only a quarter of the total thickness, it notably enhanced the fracture toughness by nearly 15%.

Table 4.1. Detailed data for the calculation of K_{IC} in the Figure 4.5c. Reprinted from [96].

Item	***B* (μm)**	***W* (μm)**	***L* (μm)**	***a* (μm)**	***F*$_C$ (μN)**	***K*$_{IC}$ (MPa $m^{1/2}$)**
cg-coating	1.87	1.95	9.49	0.57	234.4	2.82
	1.91	1.93	9.47	0.57	217.3	2.59
	1.81	1.94	9.51	0.57	226.7	2.84
	1.93	1.99	9.49	0.57	244.8	2.74
	1.87	1.94	9.47	0.57	210.4	2.57
	1.93	1.91	9.49	0.57	225.6	2.72
	1.91	1.94	9.49	0.57	246.2	2.90
	1.92	1.93	9.49	0.57	217.6	2.59
	1.91	1.94	9.49	0.57	213.0	2.53
	1.91	1.94	9.51	0.57	211.9	2.55
	1.91	1.90	9.49	0.57	210.4	2.64
cg/epi-coating	1.92	1.85	9.00	0.70	201.5	2.99
	1.88	1.69	9.09	0.69	154.9	2.95
	1.87	1.89	9.00	0.71	208.7	3.09
	1.64	1.91	8.98	0.73	188.9	3.15
	1.63	1.85	9.02	0.71	169.8	3.06
	1.72	1.84	9.04	0.77	173.7	3.28
	1.83	1.85	9.04	0.71	189.2	3.05
	1.82	1.85	9.00	0.71	204.6	3.26

A comparison of the fracture surfaces reveals a flatter morphology in the epitaxial region adjacent to the MgO substrate (Figure 4.5d and e), whereas the cg region and the upper part of the cg/epi-coating show rougher surfaces, suggesting predominantly intergranular fracture. This reduction in roughness in the epitaxial region indicates a change in crack path once the crack enters the bottom layer. Consequently, even though the notch was positioned in the cg region, the underlying epitaxial layer contributes to the overall fracture resistance of the cg/epi-coating, leading to the slightly higher measured K_{IC} in Figure 4.5. To further quantify the contributions of the columnar and epitaxial regions, we performed dedicated bridge-notch experiments, as described in the following section.

To determine the apparent fracture toughness of the columnar-grained and the epitaxial microstructure, we employed bridge notches in 90-degree rotated micro-cantilevers (compare the growth directions in Figure 4.7a). This approach allows for positioning each material bridge in either of the two microstructures in epi/cg-coating, and measure the apparent fracture toughness from the local region of the coating.

We first analyzed the bridge-failure sequence, i.e., the temporal occurrence of failure of each bridge. By correlating the *in situ* SEM video with the load drops in the load–displacement curves, we could determine which bridge (left or right) fractured first. For example, Figure 4.7b and c shows the failure of the left bridge while the other still remained intact. The statistics of the failure sequence (Figure 4.7d) provide a clear indication of the weaker bridge: in the case of cg/epi-coatings, the columnar-grained microstructure (left bridge) failed first, whereas a uniform distribution was found for the cg-coating. Additional *in situ* SEM snapshots showing the failure sequences of both coatings can be found in Figure 4.8. The differences in failure sequence in the cg/epi sample clearly demonstrate the contrasting fracture behavior of the epitaxial and columnar microstructures, and qualitatively indicates that columnar grain boundaries are indeed the weakest link in hard coatings, exhibiting lower fracture toughness compared to the epitaxial microstructure.

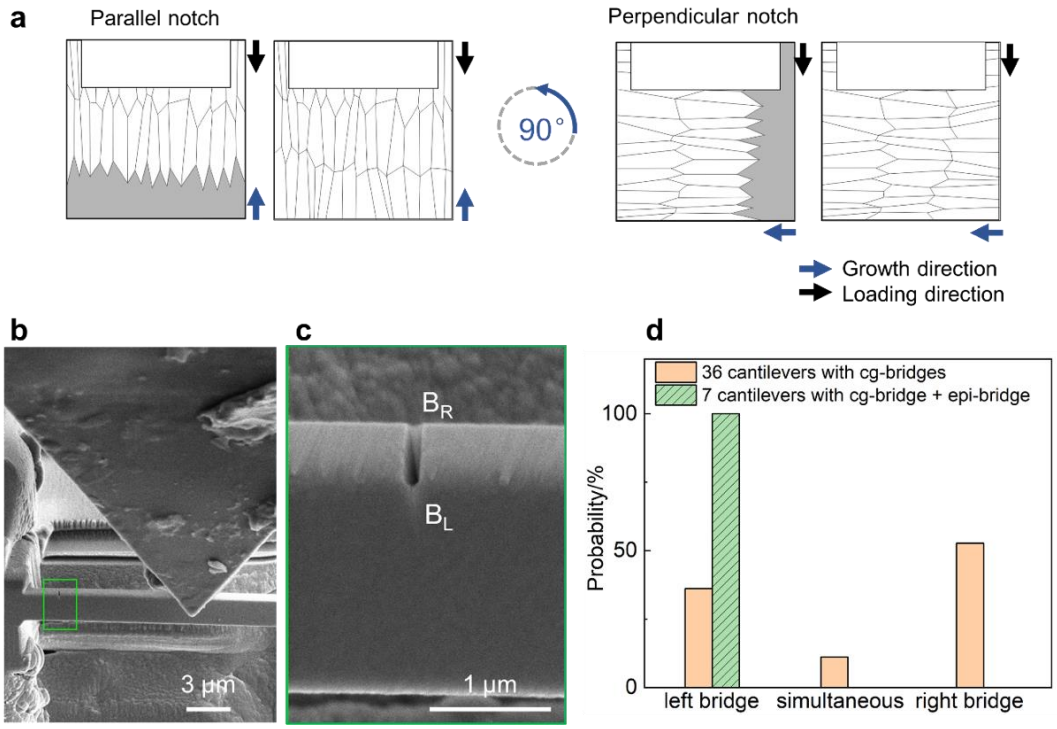

Figure 4.7. (a) The schematics showing cross-sections of micro-cantilevers with bridge notches. Material bridges were positioned within each microstructure, i.e., the columnar grain and epitaxial microstructure, by rotating the coating 90 degrees. (b) Screen shot from test video, and (c) its enlarged view, where the bridge on the observed tip side is defined as the left bridge (B_L) and the opposite as the right bridge (B_R) (d) Statistics of bridge-failure sequence. The orange bars represent 36 micro-cantilevers only with cg-bridges, and the green bar shows 7 micro-cantilevers from the cg/epi-coating with a cg-bridge on the left and an epi-bridge on the right side. The failure sequence is random when the microstructure of both bridges is similar, while in the cg/epi-coating, the bridge with epitaxial microstructure was always broken after the columnar one. Reprinted from [96].

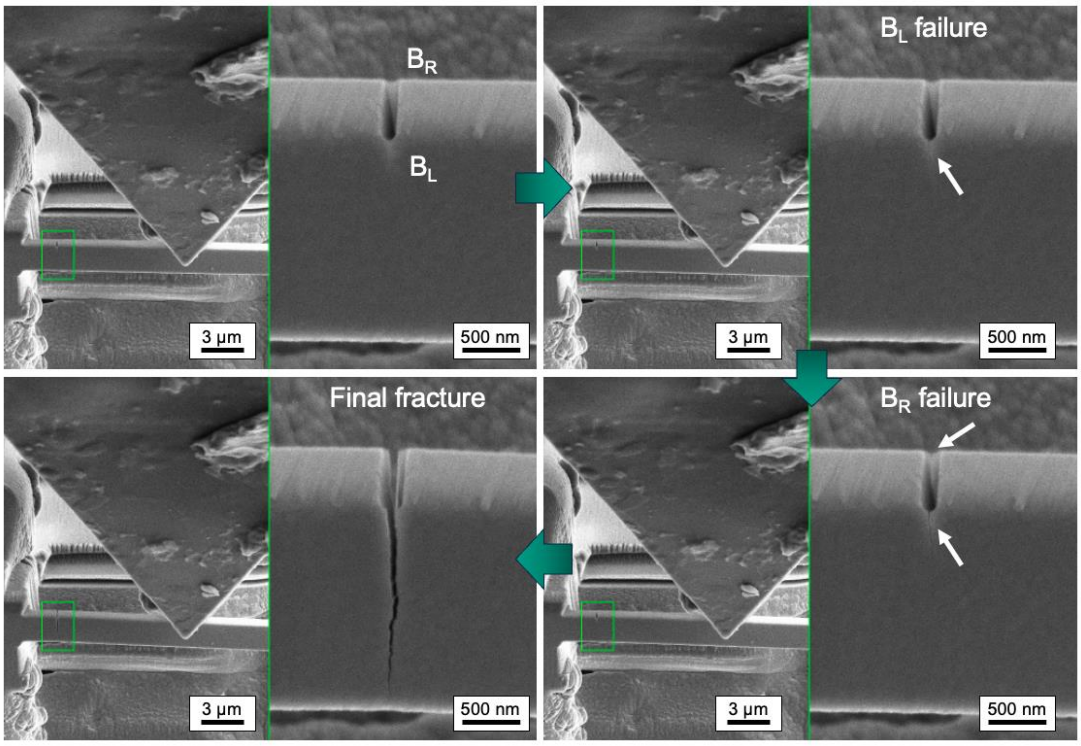

Figure 4.8. The snapshots of the *in situ* SEM videos showing the failure sequence of each bridge. Reprinted from [96].

Besides the failure sequence, we also used the load drops (B1 and B2 in Figure 4.5b) caused by bridge-failure to calculate the local apparent fracture toughness K_{IC}^{*} from bridge-failure using Equation (4.3). In brittle ceramics, extrinsic toughening is often considered the primary mechanism for enhancing toughness, as discussed by Lawn [23]. For example, the fracture toughness of traditional polycrystalline SiC is typically 2.5–4 MPa $m^{1/2}$ [181], but can increase to ~9.1 MPa $m^{1/2}$ when intergranular fracture dominates [39, 182]. One might expect significantly higher fracture toughness in the columnar microstructure than in the epitaxial layer. However, the epitaxial bridge showed a fracture toughness (denoted K_{IC}^{*}-B_R) of 4.1 ± 0.4 MPa $m^{1/2}$, which is higher compared to that of the columnar-grained bridge (K_{IC}^{*}-B_L), which is 3.0 ± 0.3 MPa $m^{1/2}$ (see Figure 4.9a). The critical loads and sample dimensions for the determination of K_{IC}^{*} are presented in the Table 4.2. Although the two samples were deposited on different substrates, the latter value is similar to experiments on a cg-coating in similar geometry i.e. with crack propagation perpendicular to the growth direction (see the orange markers in Figure 4.9a, 3.0 ± 0.2 MPa $m^{1/2}$). This is another indication that the fracture toughness of such brittle hard coatings is dominated by microstructure, more specifically, GB structure, as the microstructure in the left bridge (B_L) is comparable to the one in the cg-coating.

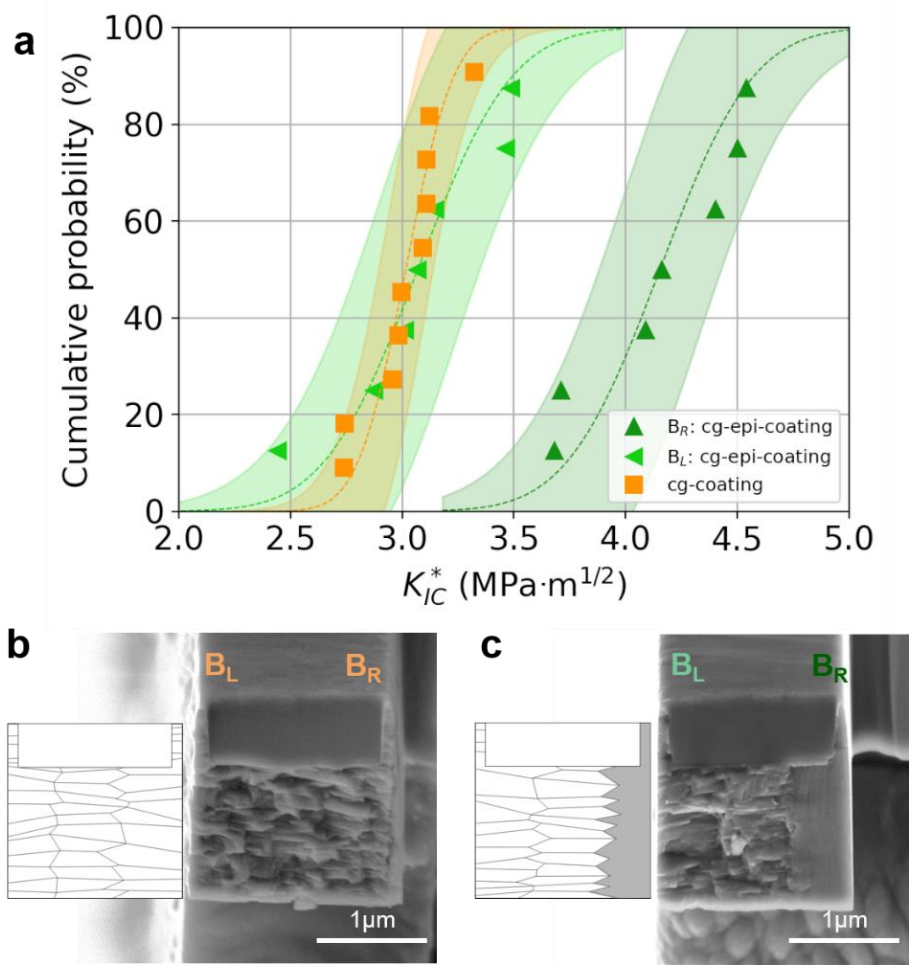

Figure 4.9. Comparison of the apparent fracture toughness from bridge-failures of two microstructures, and their fracture surface. (a) The cumulative distribution functions of the fracture toughness K_{IC}^{*} derived from bridge-failure of the cg-coating, and the cg/epi-coating with crack growth perpendicular to the film growth direction. The bands represent 95% confidence intervals. (b) SEM images of the fracture surface of the cg-coating and (c) the cg/epi coatings. Reprinted from [96].

Table 4.2. Detailed data for the calculation of K_{IC}^* in the Figure 4.9a. Reprinted from [96].

Item	B	W	L	a	b	F_B		K_{IC}*	
	(µm)	(µm)	(µm)	(µm)	(µm)	(µN)		(MPa $m^{1/2}$)	
	1.83	1.85	9.04	0.64	1.64	195.2	201.4	3.00	3.09
cg-coat-	1.85	1.83	9.09	0.65	1.65	169.7	170.2	2.74	2.75
ing	1.82	1.85	9.09	0.64	1.65	186.3	195.3	2.96	3.11
@ 90°	1.82	1.88	8.98	0.64	1.64	207.0	220.1	3.13	3.32
	1.82	1.88	9.13	0.65	1.64	191.9	199.7	2.99	3.11
Item	B	W	L	a	b	F_{BL}	F_{BR}	K_{IC}^*-B_L	K_{IC}^*-B_R
	(µm)	(µm)	(µm)	(µm)	(µm)	(µN)		(MPa $m^{1/2}$)	
	1.69	1.63	9.00	0.63	1.563	127.5	154.4	3.07	3.72
	1.71	1.74	9.09	0.63	1.593	156.7	220.0	3.14	4.40
cg/epi-	1.75	1.70	9.00	0.64	1.652	114.8	211.0	2.45	4.50
coating	1.75	1.74	9.09	0.64	1.645	143.8	207.7	2.88	4.17
@ 90°	1.76	1.65	9.02	0.64	1.66	151.3	198.3	3.46	4.54
	1.73	1.45	9.04	0.64	1.63	102.4	120.4	3.48	4.09
	1.69	1.72	9.00	0.65	1.623	137.8	168.6	3.01	3.69

In addition to these quantitative measurements, the fracture surfaces also revealed clear differences between the epitaxial and the columnar microstructures. While the fracture surface is rough across the cross-section in the case of cg-coating (Figure 4.9b), indicating intergranular fracture, the right side of the fracture surface of the cg/epi-coating was smooth, characteristic of intragranular fracture in the epitaxial microstructure (Figure 4.9c). Further images of the fracture surfaces are shown in Figure 4.10.

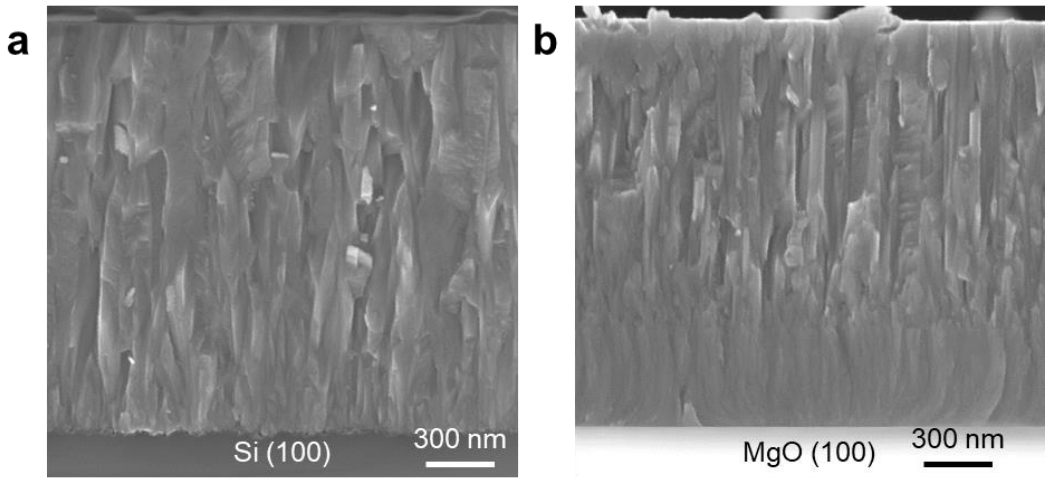

Figure 4.10. Fracture surfaces of (a) cg-coating and (b) the cg/epi-coating broken manually from the substrate side (without FIB). The epitaxial region close to the substrate shows less topography than the same area in the cg-coating. Reprinted from [96].

4.4 Discussion

In the first dataset, where the crack propagates along the growth direction (Figure 4.5), the FIB notches of both samples were located within the columnar-grain region, regardless of their overall microstructure. The results show a higher overall fracture toughness for the cg/epi-coating, suggesting that epitaxial growth enhances toughness. However, the contribution of the epitaxial region cannot be quantitatively separated from this dataset.

In contrast, for samples rotated by 90°, such a separation becomes possible due to the thin material bridges. The right bridge (B_R) of the cg/epi-coating is epitaxial and free of columnar GBs, thus the obtained toughness values represent the fracture toughness of the epitaxial-GB free coating (Figure 4.9). The left bridge (B_L), however, exhibits columnar grain boundaries similar to those in cg-coating. Consequently, the fracture toughness values of the left bridge for both samples are in same range because of the similar microstructure. This configuration enables a direct separation and quantitative assessment of the detrimental role of columnar grain boundaries in reducing the fracture toughness of hard coatings.

The role of grain boundaries in fracture toughness has long been debated in the community. While some studies suggest that grain boundaries are detrimental, others report that they can enhance toughness by activating toughening mechanisms such as crack deflection or branching. Our results show that in the case of catastrophic failure of a brittle material, grain boundaries act as weak links compared to epitaxial regions or single-crystal-like grain interiors, where the higher atomic density requires greater energy for crack propagation. In particular, random high-angle grain boundaries, which are the most common type in engineering materials, represent less densely packed structures and therefore provide preferential crack paths that reduce toughness.

In polycrystalline materials with relatively large grains, however, grain boundaries may contribute to toughening through the aforementioned mechanisms if their orientation impedes straight crack propagation. R. Daniel et al. [171], for example, demonstrated crack deflection at grain-boundary junctions as a toughening mechanism. Similarly, our recent work on CrN and AlN coatings showed improved fracture toughness when multiple crack kinking was activated [172]. In that case, the fracture toughness increased from 2.7 ± 0.1 MPa $m^{1/2}$ when the crack propagated parallel to the columnar texture to 3.0 ± 0.2 MPa $m^{1/2}$ in the perpendicular orientation. In summary, individual grain boundaries are weaker than single-crystal regions under crack propagation, but their collective distribution may either decrease or enhance fracture toughness depending on geometry. In typical PVD-grown hard coatings, where columnar grain boundaries dominate, they act predominantly as easy crack paths, which limits fracture toughness and highlights the potential of grain-boundary engineering.

Beyond the structural role of grain boundaries, chemical segregation could also influence the mechanical response. Since no post-deposition heat treatment was applied in our experiment, significant segregation is not expected. Nevertheless, to exclude this possibility, we have performed STEM-EDS, which didn't show noticeable GB segregation (e.g., from Ga). Therefore, the significantly higher fracture toughness in the epitaxial part compared to the columnar grain part is expected to originate from its inherent properties of the single crystal and generally weak

GBs at the columnar grain structure, but not from grain boundary weakening caused by segregation.

A noteworthy aspect is the role of residual stress. Residual stress is inevitably introduced during deposition and may differ between the cg- and cg/epi-coatings due to the different substrates. However, in the present microcantilever geometry (single beam, ~2 μm thick), most of the residual stress was released during fabrication. This was confirmed by the observation that cg-coatings remained nearly straight after being cut from the substrate, while cg/epi-coatings showed a slight downward bending, indicating elastic relaxation of residual stress (see Figure 4.11). Therefore, in the present study, the influence of residual stress on the measured fracture toughness is considered negligible compared to the effect of microstructure.

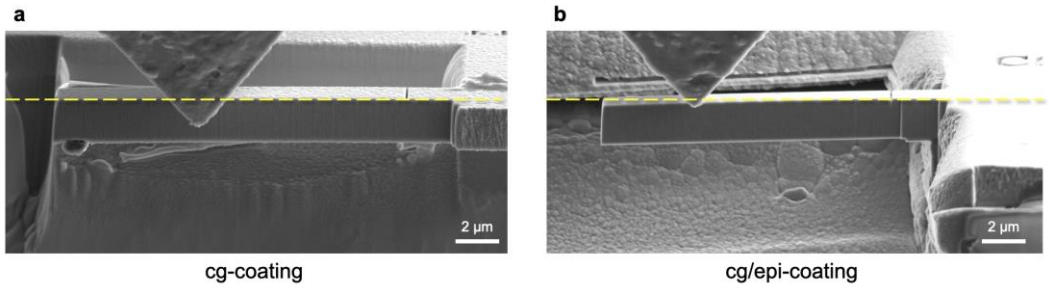

Figure 4.11. SEM images of two cantilevers from (a) cg- and (b) cg/epi-coatings, respectively. The cantilever from the cg-coating remains almost straight while cg-epi coating cantilever is slightly bent downward, which is attributed to the residual stress. The vertical dashed line in yellow is included to help visualizing the elastic bending of the cantilever. Reprinted from [96].

Finally, other crystal defects inside a grain, for example, point defects or voids, could also influence the fracture toughness. Since the coating was deposited in a single deposition process and no additional heat treatment was conducted, we don't expect substantial fluctuation in the defect density within different positions of the coating.

4.5 Conclusion

In conclusion, columnar grain boundaries clearly act as the weakest link in the fracture of hard coatings. This study provides a quantitative assessment of the decrease in their resistance to crack growth with bridge notch micro-cantilevers. The low grain boundary toughness was demonstrated both qualitatively through the failure sequence of the sample bridges, and quantitatively through fracture toughness measurements at bridge-failure, using samples with two distinct microstructures in one coating: columnar grains and an epitaxial seed layer. The apparent fracture toughness measured from the bridges composed solely of the epitaxial microstructure was found to be around 30% higher compared to that of the columnar grains (compare 4.1 ± 0.4 MPa $m^{1/2}$ and 3.0 ± 0.3 MPa $m^{1/2}$).

5 Toughening nitride hard coatings by deflecting cracks along grain boundaries

Chapter 5 is based on a published journal article.

Y. Zhang, M. Bartosik, S. Brinckmann, S. Lee and C. Kirchlechner, Toughening nitride hard coatings by deflecting cracks along grain boundaries, Mater. Sci. Eng. A (2025) 148392. https://doi.org/10.1016/j.msea.2025.148392

A detailed description of the contributions of all the researchers involved in experiments and interpretations can be found in the appendix.

5.1 Introduction

Hard coatings, composed mainly of metal carbides or nitrides, are widely used in aerospace [8], automotive engineering [38], and cutting tools for manufacturing [5] due to their ability to extend component service life by providing protection against harsh environments [35-37, 183]. A critical property of these coatings is their toughness, fundamentally represented by the fracture toughness, K_{IC} [17, 49, 52, 56, 184]. During fabrication—particularly in coatings synthesized using PVD—a columnar grain microstructure with elongated grains aligned parallel to the growth direction often forms [9, 10, 185, 186]. Grain boundaries (GBs) have been reported to act as preferential pathways for crack propagation, thereby reducing fracture toughness. Consequently, due to their anisotropic microstructure with elongated columnar grains, PVD-grown hard coatings are expected to exhibit orientation-dependent fracture toughness, which varies with the crack propagation direction relative to the columnar microstructure's orientation, hereafter referred to as the GBs orientation.

However, quantifying the anisotropic fracture behavior poses significant challenges due to their micrometer-scale thickness and limited volume, requiring the use of fracture testing at the microscale [24, 29, 175]. Several studies have reported the effect of crack propagation direction on the fracture toughness of hard coatings using micromechanics [90, 167, 168, 171, 187, 188], as well as the anisotropic nature of fracture toughness [30, 168, 188, 189]. For instance, a nanostructured NbMoTaW high-entropy alloy thin film exhibited lower fracture toughness when tested perpendicular to the film growth direction compared to tests performed parallel to the growth direction [30]. In contrast, a recent study by Schoof et al. on vanadium-aluminum (oxy)nitride coatings revealed higher K_{IC} when tested perpendicular to the growth direction in coatings with a columnar grain structure [168]. These contrasting observations underscore the inconsistencies in the role of GB orientation in hard coatings which may depend on the material and even specific GB properties. Moreover, while nitride coatings have been extensively studied, a quantitative analysis addressing the influence of GB orientation still remains lacking for CrN and AlN.

This study aims to explore the anisotropy in fracture toughness and crack propagation behavior of three nitride hard coatings—CrN, AlN, and their laminated structure—by focusing on the role

of columnar microstructure and GBs. To this end, *in situ* SEM micro-cantilever bending tests were performed under two distinct loading directions: one promoting crack propagation parallel to the coating growth direction, and the other perpendicular to it, thereby altering the orientation of the crack path relative to the columnar grain structure. By employing the same coating system under two distinct loading directions, we were able to isolate and quantify the effect of GB orientation on fracture toughness, independent of other microstructural variations that may arise during synthesis. This approach eliminates confounding variables associated with comparing different coatings, enabling a direct assessment of how GB alignment and crack propagation direction influence fracture toughness.

Our results reveal that in all three coatings, cracks propagating perpendicular to the growth direction underwent continuous crack deflection along GBs due to smaller effective grain size encountered along their path, resulting approximately 8% increase in fracture toughness. In contrast, when the crack propagated parallel to the columnar structure, the GBs were aligned with the crack path, allowing relatively smooth propagation and thus lower toughness. To the best of our knowledge, this is the first quantitative assessment of fracture toughness anisotropy in CrN and AlN coatings using micro-fracture testing. These findings not only demonstrate the critical role of GB orientation and crack deflection in enhancing fracture toughness, but also provide a valuable framework for microstructure-guided design of mechanically robust hard coatings.

5.2 Experimental procedures

Three different coatings were prepared using unbalanced reactive magnetron sputtering: (1) a monolithic CrN coating with a thickness of 1.5 µm on Si (100) substrates, (2) a 4.0 µm thick monolithic AlN coating on MgO (100) substrates, and (3) a CrN/AlN multilayer coating with a thickness of 1.9 µm on Si (100) substrates. The CrN/AlN multilayer coating consists of alternating layers of approximately 4 nm of CrN and 2 nm of AlN [123]. The phase of the films was analyzed using X-ray diffraction [190]. SEM (Merlin Gemini II, Zeiss) and FIB (Crossbeam 550L, Zeiss) were used to characterize the surface and cross-sectional microstructure of the samples.

These three coatings were selected to investigate the influence of microstructural features on fracture behavior. CrN and AlN coatings were intentionally deposited on different substrates—Si and MgO, respectively—to introduce variations in substrate type, crystal structure (cubic for CrN vs. hexagonal for AlN), grain size, and residual stress. This allowed us to evaluate how these factors affect crack propagation along grain boundaries and overall fracture toughness. The CrN/AlN multilayer, deposited on the same substrate as CrN, shares the cubic structure but incorporates a nanoscale layered architecture, enabling the influence of multilayering and associated residual stress to be assessed.

The depositions were carried out in an AJA ATC-1800 ultra-high vacuum deposition system, equipped with Cr and Al targets, each with a three-inch diameter and 99.99% purity. The targets were powered in pulsed DC mode at 100 kHz with a 1 µs pause. The Cr and Al targets were subjected to time-averaged powers of 300 W and 500 W, respectively. The coatings were grown in a gas mixture of N_2 at a flow rate of 12 sccm and Ar at a flow rate of 8 sccm, with a total gas pressure of 0.2 Pa. To obtain a dense coating morphology, a DC bias voltage of -70 V was applied

to the substrates during coating growth. Throughout the deposition process, the deposition parameters were kept constant while computer-controlled mechanical shutters periodically opened and closed to create the multilayer structure of the CrN/AlN multilayer coating. During deposition, the substrates were constantly rotated with a frequency of about 0.5 Hz. More detailed information of the deposition processes can be found in [191].

Before fabricating micro-cantilevers, the Si substrates of CrN/AlN multilayer and CrN coatings were etched using a 30 wt.% potassium hydroxide solution at 60 °C for 30 minutes to obtain 20 µm-long free-standing film segments. Cantilevers were then fabricated by using FIB milling with Ga ions at an acceleration voltage of 30 kV (Crossbeam 550L, Zeiss). The ion beam current was varied as follows: 15 nA for coarse milling, 3 nA, 700 pA, 300 pA for intermediate steps, and 50 pA for final milling. The cantilevers of the AlN coating on MgO—which cannot be similarly etched as Si—required removal of the substrate by Ga ion milling with the same series of milling currents as mentioned above. Notches were milled using a 20 pA current with a 1.0 µs dwell time. A bridge notch design retaining two ligaments on either side was employed instead of a straight through-thickness notch. The purpose of this design is to initiate a crack from the FIB-milled notch at the material bridge, and then arrest its propagation to form a naturally sharp crack, which triggers the final fracture of the cantilever [29, 123]. The dimensions of the bridge notch cantilevers were prepared according to the schematic in Figure 5.1, with L being the distance between the loading position and the notch, W is the thickness of the cantilever, B is the width of the cantilever, b is the width of the notch, and a is the depth of the notch. The thickness W varied from 1.5 µm to 2.5 µm, depending on the coating thickness (1.5 µm for the CrN coating, 1.9 µm for the CrN/AlN multilayer coating, and 2.5 µm for the AlN coating). To minimize geometry-related influences on the fracture response across samples with varying coating thicknesses, the L:W:B ratio was kept constant at 5:1:1 for all cantilevers by adjusting the width B accordingly. The notch depth, a, was set to 20–30% of the cantilever thickness, and the bridge width was minimized to below 100 nm to enhance the stress concentration at the bridge, thereby promoting bridge failure and subsequent crack arrest [123].

Micromechanical fracture tests of the FIB-prepared cantilevers were conducted in an SEM with an *in situ* nanoindenter (Hysitron PI-89, Bruker) equipped with a 10 µm wide diamond wedge tip (Synton-MDP AG). All *in situ* SEM deformations were performed in a displacement-controlled mode with a displacement rate of 5 nm/s. The maximum load of the transducer was 10 mN, and an intrinsic noise floor was 0.4 µN.

Indentation hardness was measured using a UMIS nanoindenter from Fischer-Cripps Laboratories. A diamond Berkovich tip was used, and the nanohardness and indentation modulus were calculated using the Oliver and Pharr method [192]. A schematic overview of the experimental procedure and comparative framework is provided in Figure 5.2, illustrating the three different coating systems, the two loading directions, and the overall analysis logic.

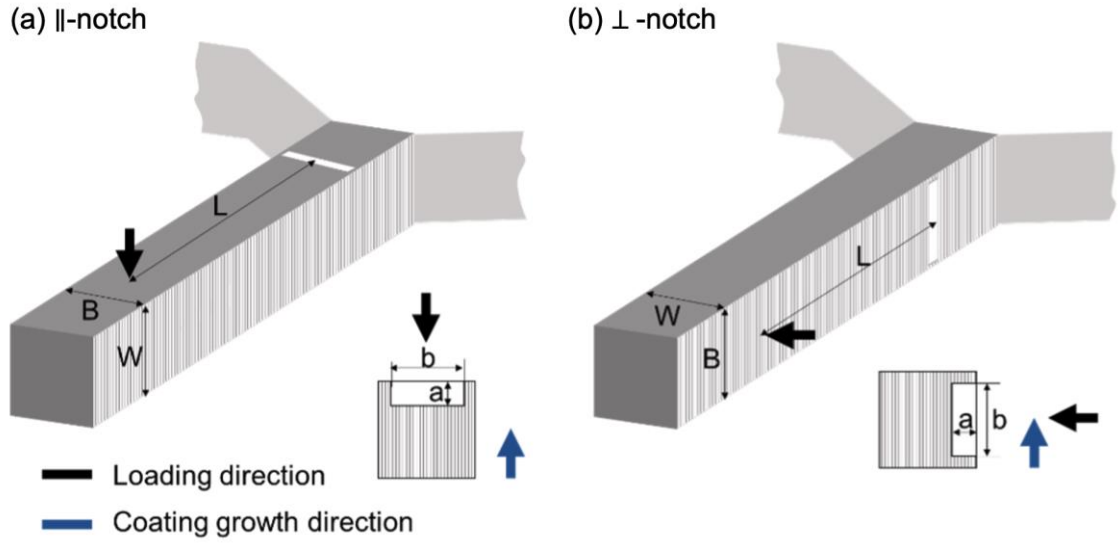

Figure 5.1. Schematic illustration of two micro-cantilever geometries with different loading directions: (a) loading parallel to the coating growth direction (∥-notch), and (b) loading perpendicular to the growth direction (⊥-notch). The insets illustrate the cross-sectional view of the bridge notches. Reprinted from [193].

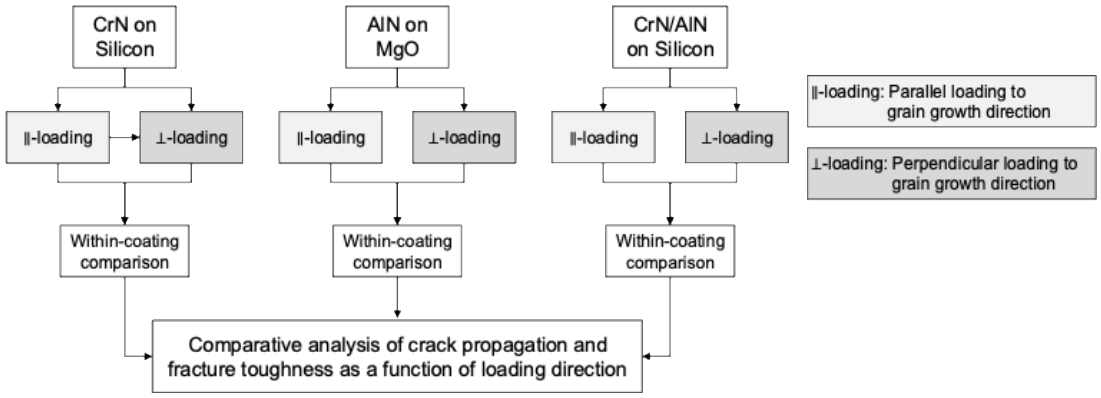

Figure 5.2. Flowchart of the experimental design. Three coatings were tested under two loading directions (∥ and ⊥ to grain growth) to compare crack propagation behavior and K_{IC} values. Reprinted from [193].

5.3 Results and discussion

The microstructures of the three hard coatings investigated in this study are presented in Figure 5.3. FIB channeling contrast imaging was performed on both the FIB cross-section and the top surface to analyze microstructure and grain size. The columnar grain structure, which is elongated along the film growth direction, is clearly revealed in all coatings. The columnar grains exhibit a grain size ranging from approximately 70 to 100 nm measured at the top surface.

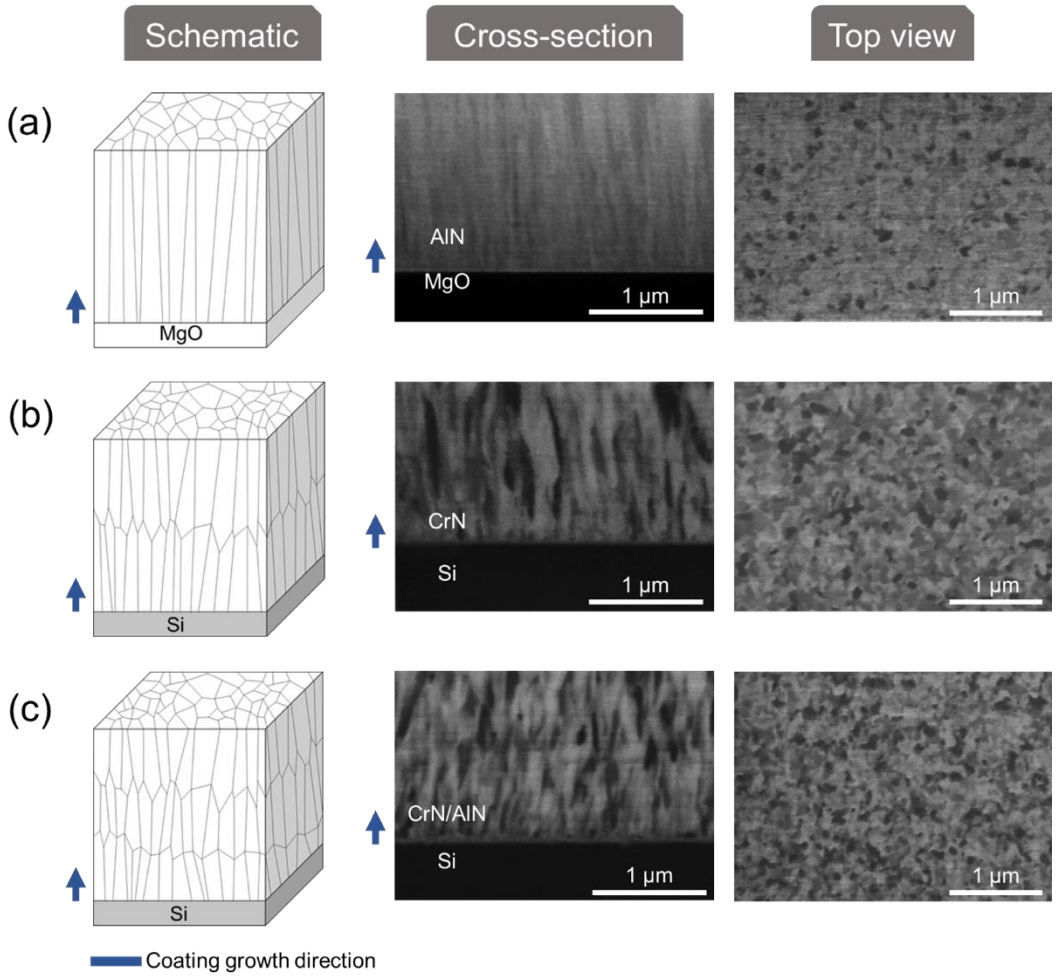

Figure 5.3. The first column displays a schematic drawing of the microstructure, the second and the third columns are FIB channeling contrast images, showing the cross-section and the top view of each coating, (a) AlN on MgO, (b) CrN on Si, and (c) CrN/AlN on Si. Reprinted from [193].

Micro-cantilevers were fabricated using FIB to have two different crack propagation—and consequently load application—directions. In the first geometry, the crack propagation from the FIB-milled notch was parallel to the coating's growth direction, hereafter referred to as ∥-notch. In the second geometry, the crack propagation was perpendicular to the growth direction, and therefore perpendicular to the columnar grain direction, referred to as ⊥-notch. Please note that the global crack plane of both, the ∥- and the ⊥-notch, are identical, but only the crack propagation direction differ as the tests were performed on the same samples with different loading orientations. Therefore, crystallographic texture which typically is present in hard coatings does not cause the differences in the measured fracture toughness of samples with ∥- and the ⊥-notches.

Representative load–displacement curves from ∥-notched cantilevers are shown in Figure 5.4a, displaying the typical linear-elastic fracture of micro-cantilevers: a linear load increase up to a critical point, followed by sudden fracture [99, 194]. Variations in the slopes of these curves, reflecting differences in sample stiffness, are primarily attributed to differences in sample geometry, such as film thickness. Load drops at the point of bridge failure, marked by black arrows and provided in a magnified view inside insets, indicate crack arrest similar to our previous

report in [123]. These load drops occur because the thin material bridges on the cantilever body fails first due to localized stress concentration. This stress focusing at the bridge effectively arrests the crack temporarily and promotes fracture initiation from a naturally sharp crack tip formed during bridge failure [123]. A total of 8, 11, and 7 cantilevers with a ∥-notch were tested for AlN, CrN/AlN, and CrN coatings, respectively. All load-displacement curves for CrN/AlN coatings with ∥-notch are shown in Figure 5.4b as examples. For comparison, the corresponding load-displacement curves for cantilevers with a ⊥-notch are provided in Figure 5.5. In all cases, the cantilevers failed in a brittle, linear-elastic fracture manner, exhibiting highly consistent load-displacement behavior across multiple specimens. Notably, in most cases, two distinct load drops were observed, indicating crack arrest due to bridge failure. This suggests that fracture initiated from a naturally sharp crack before final failure occurred [123].

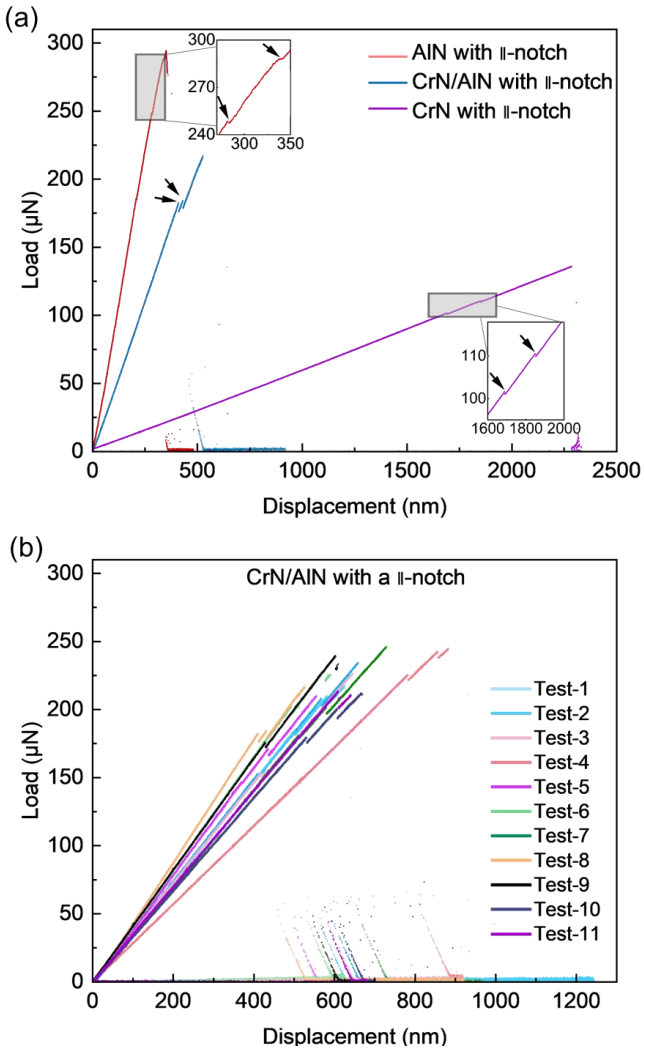

Figure 5.4. (a) Load-displacement curves from a single test on AlN, CrN/AlN and CrN coatings with a ∥-notch. Arrows indicate the load drops caused by bridge failure and subsequent crack arrest. (b) All curves of 11 micro-cantilever fracture tests on CrN/AlN coating with a ∥-notch. Reprinted from [193].

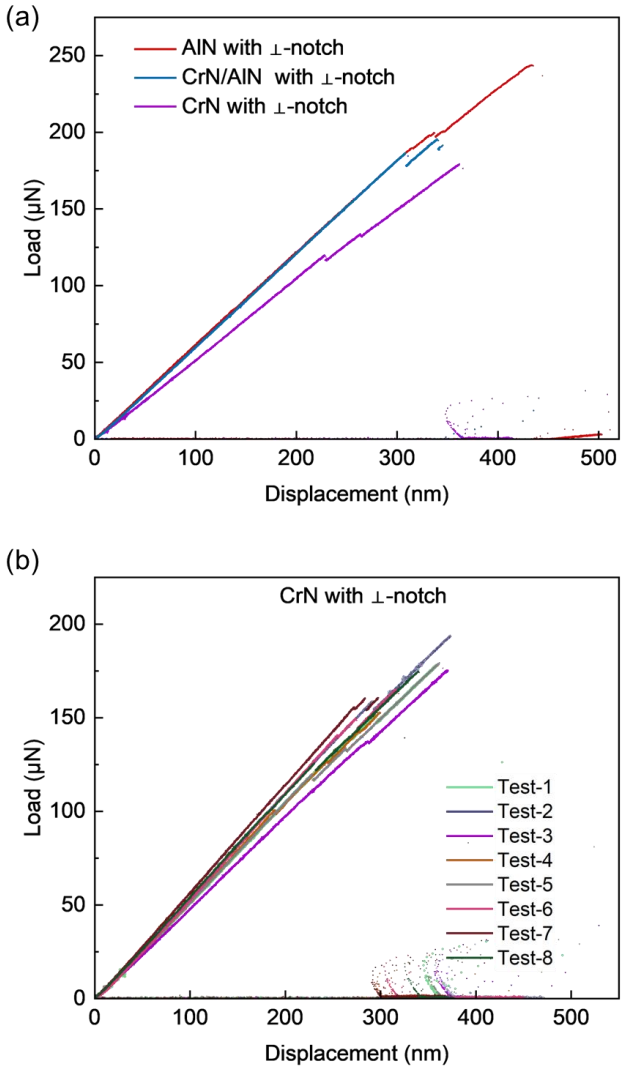

Figure 5.5. The load-displacement curves. (a) A representative cantilever bending test on AlN, CrN/AlN, and CrN coatings with a ⊥-notch. (b) All 8 cantilever bending tests on CrN coating with a ⊥-notch. Reprinted from [193].

The fracture toughness and failure characteristics of AlN, CrN/AlN, and CrN coatings were evaluated from the resulting load-displacement curves and the cantilever geometry. As shown in Figure 5.4, all samples exhibited linear-elastic fracture with bridge failures, followed by final fracture at the arrested crack. Therefore, the fracture toughness, K_{IC}, calculated assuming a through-thickness notch geometry after crack arrest using the following equation [29]:

$$K_{IC} = \frac{F_C L}{B W^{3/2}} f\left(\frac{a}{W}\right) \tag{5.1}$$

$$f\left(\frac{a}{W}\right) = 1.46 + 24.36(a/W) - 47.21(a/W)^2 + 75.18(a/W)^3 \tag{5.2}$$

where, F_C is the load at the final fracture, $f\left(\frac{a}{W}\right)$ is a geometry shape factor, and L, B, W, and a are the parameters from the geometry of the cantilever.

The calculated fracture toughness, $\underline{K_{IC}}$, of all cantilevers including those with ∥-notch or ⊥-notch, is plotted as a cumulative probability distribution for statistical analysis (Figure 5.6). The data were fitted with a normal cumulative distribution function (CDF) where the 95% confidence intervals are highlighted by shading. Firstly, we found that the AlN hard coating has a lower fracture toughness than the CrN hard coatings in both ⊥-notch and ∥-notch. The K_{IC} of the CrN/AlN multilayer coatings with a material volume ratio of 2 is in between the CrN and AlN coatings. The expected toughening effect from the nanoscale interfaces in the CrN/AlN multilayer was less pronounced, indicating that the interface density in the current design may not be sufficient to significantly enhance fracture resistance through crack deflection or energy dissipation mechanisms.

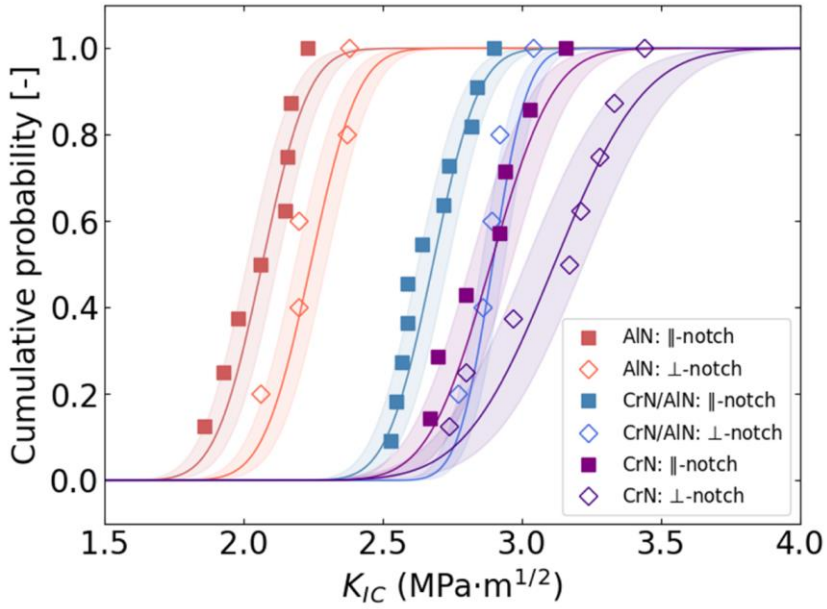

Figure 5.6**.** Cumulative distribution of fracture toughness of AlN (red curves), CrN/AlN (blue curves), and CrN (orange curves) coatings. Data from ∥-notch cantilevers are represented by solid markers, while results from ⊥-notch cantilevers are indicated by open markers. Reprinted from [193].

Additionally, in all three coatings, the cantilevers with ⊥-notch exhibited higher fracture toughness compared to those with ∥-notch (Figure 5.6 and Table 5.1). An increase in fracture toughness of 8.4%, 8.0%, and 8.0% was measured for AlN, CrN/AlN, and CrN micro-cantilevers, respectively, when ⊥-notch cantilevers were compared with ∥-notch cantilevers. These quantitative measurements highlight the critical role of GB orientation relative to the crack propagation direction in determining the fracture toughness of hard coatings, regardless of their chemical composition, or their substrate and resulting microstructural features such as grain size or residual stress.

Table 5.1. Indentation hardness and Young's modulus of AlN, CrN/AlN, and CrN coatings. And their fracture toughness (MPa $m^{1/2}$) and standard error of the mean with ⊥- and ∥-notch. Reprinted from [193].

Coating—Substrate	Hardness [GPa]	Young's modulus [GPa]	Fracture toughness (MPa $m^{1/2}$)	
			⊥-notch	∥-notch
AlN—MgO	20.3 ± 1.7	327 ± 20	2.24 ± 0.06	2.07 ± 0.05
CrN/AlN—Si	28.2 ± 0.7	314 ± 9	2.90 ± 0.04	2.68 ± 0.04
CrN—Si	21.7 ± 0.9	309 ± 10	3.12 ± 0.09	2.89 ± 0.07

Representative SEM images of the fracture surfaces on the tested micro-cantilevers are shown in Figure 5.7. A columnar grain structure is observed in all SEM images, which is consistent throughout the coating's thickness. In the first row, where the crack propagation is parallel to the growth direction, the columnar microstructure is characterized by a vertically aligned pattern, while the fracture surfaces of the cantilevers with a ⊥-notch exhibit horizontal features in the second row. Fractography shows the crack propagation mainly along GBs regardless of notch orientation, indicating that intergranular fracture was the dominating fracture mechanism.

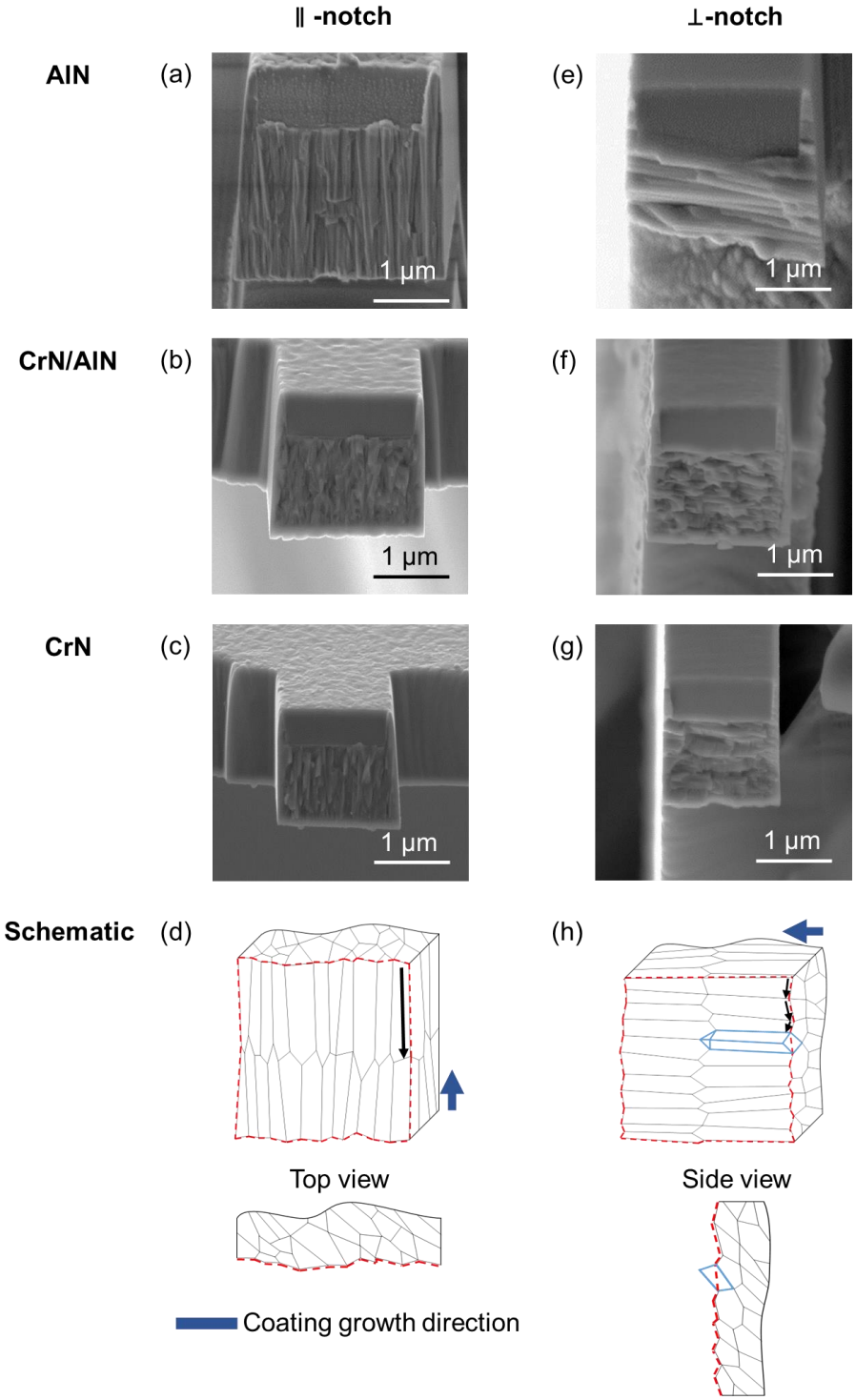

Figure 5.7. Fracture surface of AlN, CrN/AlN, and CrN coatings with different notches. (a)–(c) The first row shows surfaces with a ∥-notch, (e)–(g) while the second row shows those with a ⊥-notch. (d) Schematic illustration of crack propagation direction in different geometries with columnar grain structure. The black arrows indicate the direction of crack propagation. The crack propagation is parallel to the growth direction, and in (h) the crack propagation is perpendicular to the growth direction. Reprinted from [193].

Crack propagation was further analyzed based on the fractured surface. In the case of ⊥-notches, cracks continuously deflect while propagating along GBs. Additionally, the fracture surface reveals that, in some instances, the crack needs to propagate through the grain interior simply because there is no well-oriented GB nearby, as illustrated by the blue grain in Figure 5.7h. Our recent study found that GBs of hard coatings exhibit considerably lower fracture toughness compared to their single crystalline counter bodies with the identical chemical composition [195]. Furthermore, crack deflection and the necessity of propagating through tougher regions can modify the energy release rate at the tip of a kinked crack [49], potentially impeding crack propagation and thereby increasing fracture toughness.

In contrast, when the crack propagates along well-aligned, elongated GBs—i.e., parallel to the loading direction—it can easily propagate upon nucleation without kinking (Figure 5.7d). Although no direct evidence of crack branching was observed in the ⊥-notched samples, it can be speculated that this phenomenon is more likely to occur in these ⊥-notched samples than in those with ∥-notches due to the smaller grain size in the crack propagation direction.

Previous studies have suggested that GB engineering [169, 171, 196-198] could be a promising way to strengthen the hard coating. Notably, simply orienting the columnar grained microstructure can improve fracture toughness by 8%, even with the same microstructure and composition.

5.4 Conclusions

Three hard coatings—CrN, AlN and their multilayered variant—all exhibiting a columnar grain structure, were deposited using unbalanced reactive magnetron sputtering. Their fracture behavior was quantitatively investigated using *in situ* SEM micro-cantilever bending tests focusing on GB orientation-dependent cracks propagation, i.e. parallel and perpendicular to the elongated grain shape. The results clearly demonstrate that crack deflection along GBs significantly influences fracture toughness. Specifically, when cracks propagate perpendicular to the coating growth direction, the fracture toughness increases by approximately 8% compared to the parallel case, due to enhanced crack deflection and occasional transgranular fracture. Among the coatings, CrN exhibited the highest fracture toughness, which may be attributed to its relatively uniform cubic structure and favorable residual stress state. The CrN/AlN multilayer also showed toughening effects due to its nanoscale architecture, likely due to increased interface density. These findings highlight the critical role of GB orientation and microstructural design in improving the fracture performance of hard coatings.

6 Interplay of oxidation and void formation on degradation of fracture toughness of CrN coatings during thermal exposure

Chapter 6 is intended to be submitted as journal publication.

Y. Zhang, M. Bartosik, S. Brinckmann, U. Bansal, S. Lee and C. Kirchlechner,
Interplay of oxidation and void formation on degradation of fracture toughness of CrN coatings during thermal exposure

A detailed description of the contributions of all the researchers involved in experiments and interpretations can be found in the appendix.

6.1 Introduction

Nitride ceramic coatings, known for their high hardness and excellent wear resistance, are widely used in the manufacture of tools and components for harsh environments [1, 35, 199]. Despite their excellent properties, these coatings are often exposed to significant thermal and mechanical stresses during use, underlining the importance of understanding and tailoring the fracture behavior at high temperatures [1, 16]. Among these coatings, CrN stands out as a widely used nitride hard coating, making it an ideal material for studying the fracture toughness under elevated temperature conditions.

Determining the fracture toughness, i.e., the critical stress intensity (K_{IC}), in nitride ceramic coatings presents significant challenges, particularly due to the dimensional constraints associated with coating thickness [153]. One established method to measure the fracture toughness at the micron scale is the single cantilever bending test with a bridge notch [17, 153, 200]. This method effectively mitigates the impact of substrate-related residual stresses and FIB artifacts [29, 95, 123] and has been used to enhance the intrinsically poor toughness-related properties of hard coatings [89, 171, 201].

The influence of elevated temperature on the fracture toughness of nitride coatings has been investigated via micro-cantilever bending tests [31-33, 137, 202]. Buchinger et al. reported that the annealed TiN coatings exhibited a lower K_{IC} compared to the as-deposited coating, which results from the recovery of growth defects by the formation of voids at the grain boundary [31]. For the CrN hard coating, Riedl et al. demonstrated that its K_{IC} decreased from 3.80 MPa $m^{1/2}$ to 3.05 MPa $m^{1/2}$ after annealing [32]. However, different results were observed by Best et al., who reported that the fracture toughness of CrN films annealed at 500 °C under vacuum for a considerable duration did not change significantly by testing on a re-milling annealed sample [33]. Furthermore, they observed that annealing resulted in the emergence of a notable contrast on the surface of the samples, but this phenomenon has not been further investigated. Hence, there is a notable controversy on the temperature-dependent fracture properties of CrN coatings and a lack of a mechanistic understanding of their performance. The reported differences in the performance

of hard coatings after annealing [33] may stem from changes in the annealed microstructure of the samples and the influence of Ga ions – factors that have not been completely investigated so far.

In this study, the effect of annealing and Ga ions stemming from the FIB-based cantilever manufacture on the temperature dependent fracture toughness of CrN coatings was investigated *in situ*, using a series of bridge notch micro-cantilevers fabricated by FIB milling and tested over a temperature range from room temperature (RT) to 600 °C in a SEM. The mechanical data is correlated to microstructural changes – specifically the formation of new phases and voids, and their dependence on residual stress.

6.2 Experiment

6.2.1 Hard coating synthesis

Monolithic CrN coatings were prepared on Si (100) substrates using unbalanced reactive magnetron sputtering techniques (see Table 6.1). The deposition was conducted in an AJA ATC-1800 ultra-high vacuum deposition system, equipped with a Cr target of three-inch diameter and 99.99% purity. The target was powered in pulsed DC mode at a frequency of 100 kHz with a 1 μs pause and a time-averaged power of 300 W. The coatings were grown in a mixed N_2/Ar gas (a flow rate of 12 sccm / 8 sccm) with a total gas pressure of 0.2 Pa. To obtain a dense coating morphology, a DC bias voltage of -70 V was applied to the substrates during coating growth. During deposition, the substrates rotated constantly with a frequency of about 0.5 Hz.

Table 6.1. The properties of two CrN coatings.

No.	Sample	Material	Substrate	Thickness [μm]	Hardness [GPa]	Young's modulus [GPa]
C1	S1, S2, S3	CrN	Si	1.9	21.9 ± 0.7	312 ± 11
C2	S4	CrN	Si	1.5	21.7 ± 0.9	309 ± 10

Before deposition, the Si (100) substrates underwent a pre-cleaning process in an ultrasonic bath filled with acetone and ethanol for 5 min, respectively. The substrates were then clamped on the substrate holder and transferred to the vacuum chamber using a load-lock system. The base pressure within the vacuum chamber was kept below 3 x 10^{-6} mbar. Thermal cleaning of the substrates was conducted at 550 °C for 30 min, followed by ion etching at 500 °C for 5–10 min in a pure Ar atmosphere.

6.2.2 Micro-cantilevers preparation

Before preparing the cantilevers for *in situ* SEM high-temperature fracture testing, the Si substrates of CrN hard coating (sample S1) were etched using a 30 wt.% potassium hydroxide (KOH) solution at 60 °C for 30 min to acquire 20 μm lengths of free-standing film segments as

used in [89, 203]. Afterwards, all cantilevers were fabricated by FIB milling (Crossbeam 550L, Zeiss) at 30 kV: coarse milling was performed at 15 nA, intermittent steps at 3 nA, 700 pA, and 300 pA, and fine milling at 50 pA probe current. During the post-mortem analysis, some cantilevers on the annealed sample required substrate removal by bottom milling under the same series of milling currents.

The notches were milled using a 20 pA current and a 1.0 µs dwell time, resulting in the formation of a sharp notch. A bridge notch, which retains two ligaments on both sides, was employed instead of a straight through-thickness notch. The objective of this cantilever configuration is to initiate a natural sharp crack that arrests at the material bridge, finally resulting in a catastrophic fracture at the newly formed crack tip [29, 123, 204]. The nominal dimensions of the bridge notch cantilevers were prepared, as shown in Figure 3.2. *L* is the distance between the loading position and the notch, *W* is the thickness of the cantilever, *B* is the width of the cantilever, *b* is the width of the notch, and *a* is the depth of the notch. The measured notch depth was 0.63 ± 0.02 µm, corresponding to a very consistent geometry across all specimens, and the bridge width was kept as thin as possible to increase the stress concentration at the bridge, thus promoting bridge failure and subsequent crack arrest. The nominal widths *B* and thickness *W* of the cantilevers were about 1.9 µm for the CrN hard coatings. The nominal ratio of *L*:*W*:*B* was kept constant at 5:1:1, throughout all the cantilevers.

6.2.3 *in situ* bridge notch micro-cantilever bending test

Micromechanical fracture experiments were conducted at high temperatures (HT) *in situ* SEM (Merlin Gemini II, Zeiss) using a high-temperature setup (Hysitron PI-89, Bruker) equipped with a 10 µm wide diamond wedge tip (Synton-MDP AG) and a water-cooling system. All *in situ* SEM tests were operated in a displacement-controlled mode at a rate of 5 nm/s and a SEM chamber vacuum of about 10^{-5} mbar. A high-load transducer with a maximum load of 0.5 N and an intrinsic noise floor of 5 µN was used.

The fracture toughness K_{IC} was obtained using Matoy´s approach [29]:

$$K_{IC} = \frac{F_C L}{B W^{3/2}} f\left(\frac{a}{W}\right) \tag{6.1}$$

$$f\left(\frac{a}{W}\right) = 1.46 + 24.36(a/W) - 47.21(a/W)^2 + 75.18(a/W)^3 \tag{6.2}$$

where, F_c is the load at the final fracture, and $f\left(\frac{a}{W}\right)$ is a geometry shape factor. It shall be noted that for high temperatures and the used high-load transducers, the sequence of crack initiation and arrest before final fracture could not be observed in this study; that´s why we used the formalism initially developed by Matoy et al. [29].

6.2.4 Measuring the temperature dependent fracture toughness of CrN

First, high-temperature experiments were performed, ranging from RT (pre-HT) to 600 °C, with increments of 100 °C. The heating rate was 5 °C/min. A holding interval of 60 min was used to

test 5 micro cantilevers at each temperature. The time between reaching the desired temperature (±0.1 °C) and the first experiment was conducted was kept constant at 20 min. After cooling down to RT, additional cantilevers – further denoted as post-HT – were tested. All micro fracture tests were conducted on the cantilevers with the protocol as described in Section 6.2.3. During these experiments, the surface of the thin film was frequently monitored.

6.2.5 Case studies on the influence of sample conditions

In addition, we have conducted three different test cases, i.e., different sample states, to separate the effects of high temperature, annealing, and Ga exposure as outlined in Figure 6.1.

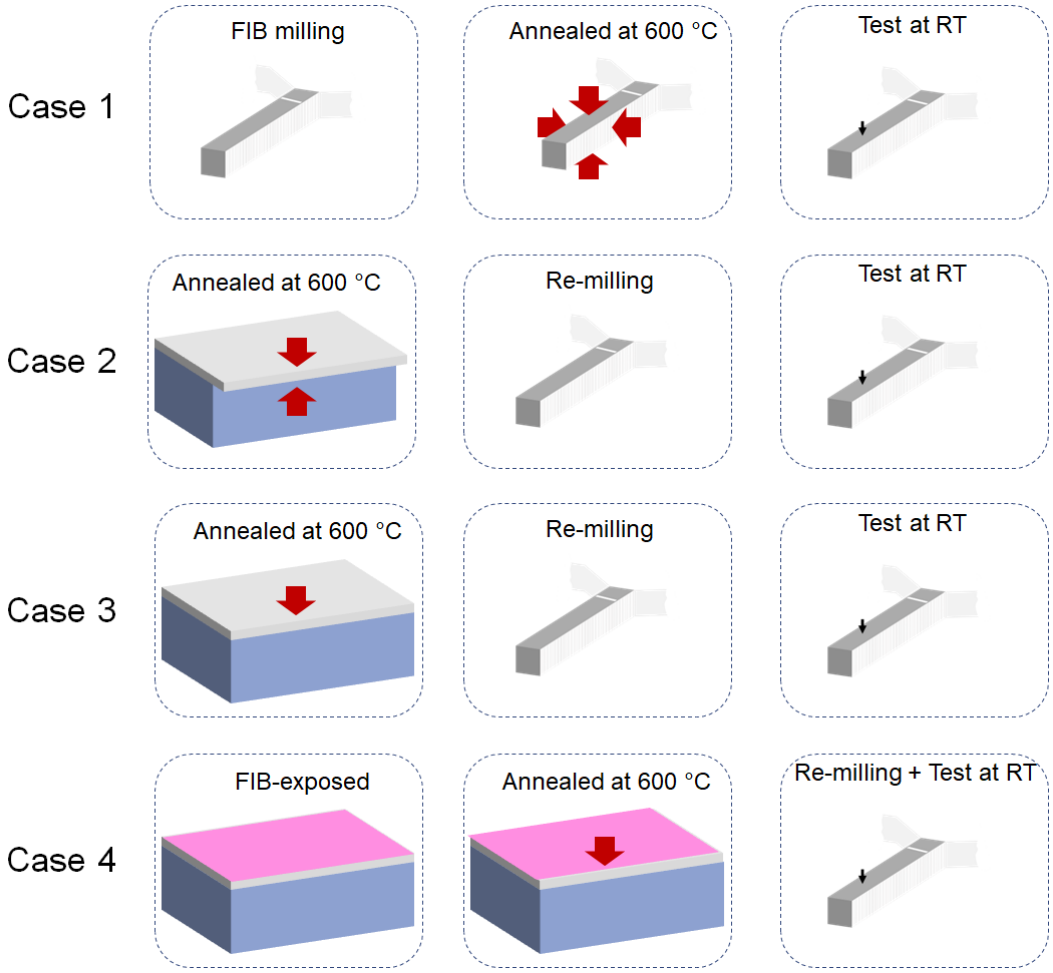

Figure 6.1. Four different case studies to decipher the role of microstructural changes during annealing

All four cases were heat-treated in the same way as the experiments described in Section 6.2.4. However, the sequence of annealing, Ga exposure for milling, and etching was changed to modify the boundary conditions during annealing. Cases 1, 2, and 3 were obtained from different regions of the same sample S1, which were annealed simultaneously in a single heat-treatment cycle.

In the first case, the cantilevers were milled and heat-treated – identically to the one presented in Sections 6.2.4 and 6.3.1. The aim of case 1 is to anneal the cantilevers in a fully unconstrained setup. The cantilever has four free surfaces "exposed" to the vacuum – as highlighted by the red arrows in Figure 6.1.

In the second case, a free-standing part of the coating was prepared by etching and subsequently annealed. Cantilevers were finally prepared by FIB and tested at RT from this free-standing portion. The aim of case 2 is to have a partially constrained annealing condition with stresses partially relaxed during etching. In this case, only two surfaces of the final cantilever had been exposed to vacuum during annealing.

In the third case, the coating was still attached to the substrate while annealing. Subsequently, cantilevers were milled from the annealed coating with the aim of an annealing treatment under constraint conditions, i.e., where stresses are still present. Note that this type of sample had only one free surface during annealing.

Finally, case four is comparable to case three. However, the attached coating was gently exposed to a de-focused FIB-beam with a current of 50 pA at 30 kV. The total scanning dose applied was 2 mC/cm², utilizing a pixel spacing of 2.25 nm, a dwell time of 1 µs, and a unidirectional scanning pattern in a back-and-forth mode in the NPVE® attached to the Zeiss Crossbeam. The coating (sample S2) was then annealed under the same vacuum conditions as experienced by sample S1, and finally, cantilevers were milled from this area. The aim of this case – in combination with the third case – is to decipher microstructural differences caused by Ga at elevated temperatures.

6.2.6 Characterization of microstructure and chemical composition

To mechanistically understand the observed drop in fracture toughness at high temperatures, the microstructure was investigated using SEM and TEM. Firstly, an electron-transparent cross-section was prepared by the standard FIB lift-out method on sample S1 annealed at 600 °C and on the as-deposited sample – denoted as sample S3.

The TEM investigations were performed on a field emission microscope (TITAN Themis 300, Thermo Fisher Scientific). The composition of CrN was obtained by EDS in STEM mode using a Super-X EDS detector in TITAN. For further chemical information, EELS experiments were conducted using a double aberration corrected TEM (Themis Z, Thermo Fisher make and equipped with a Gatan GIF Continuum 970 HighRes EELS spectrometer) operated at 300 kV.

6.3 Results and interpretation

6.3.1 The temperature dependence of the fracture toughness

A SEM image of a representative micro-cantilever before testing and a typical fracture cross-section of a micro-cantilever after failure and annealing are depicted in Figure 6.2a and b, respectively. Figure 6.2c presents examples of load-displacement curves from *in situ* SEM micro-cantilevers bending testing at pre-HT, 300 °C, and 600 °C, respectively. The pre-HT and 300 °C

data show a linear elastic response until catastrophic fracture. The cantilever tested at 600 °C slightly deviates from purely elastic behavior. A thorough examination of the images recorded during testing revealed that the deviation from elasticity corresponds to the gradual growth of the crack in the bridge before the fracture. The load at catastrophic failure is used as F_C in Equation (6.1).

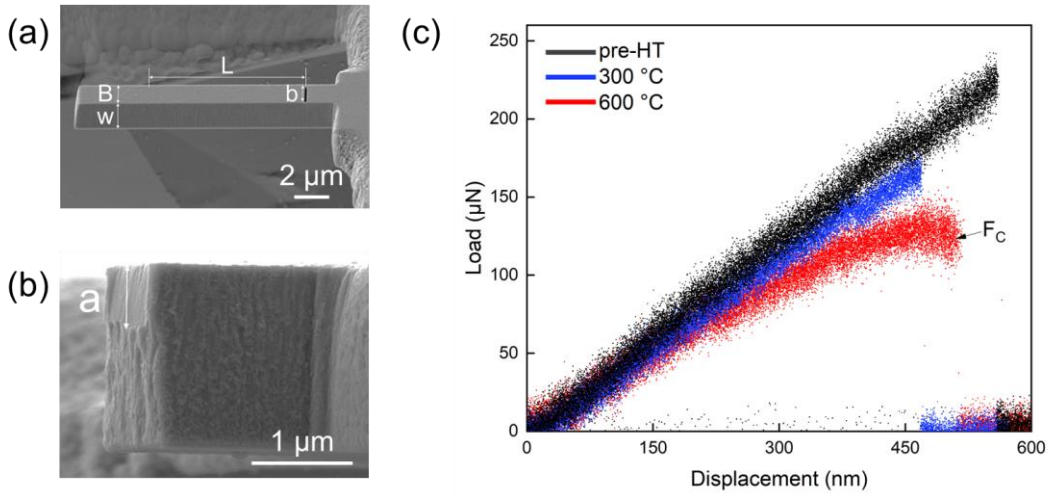

Figure 6.2. (a) Free-standing micro-cantilever on CrN hard coating. (b) Sample S1 tested at 600 °C after catastrophic failure imaged at RT. (c) Representative load-displacement curves of *in situ* SEM micro-cantilevers bending test.

The fracture toughness of the CrN coating shows a tremendous decrease with increasing temperature (see Figure 6.3). K_{Ic} decreases from 2.85 ± 0.12 MPa $m^{1/2}$ for cantilevers tested at room temperature – denoted as pre-HT – to 2.17 ± 0.12 MPa $m^{1/2}$ at 600 °C. The decline is not linear, but is more pronounced when the deposition temperature (T_{dep} = 500 °C) is reached. Finally, upon cooling back to RT, a further decrease to 1.88 ± 0.08 MPa $m^{1/2}$ (post-HT).

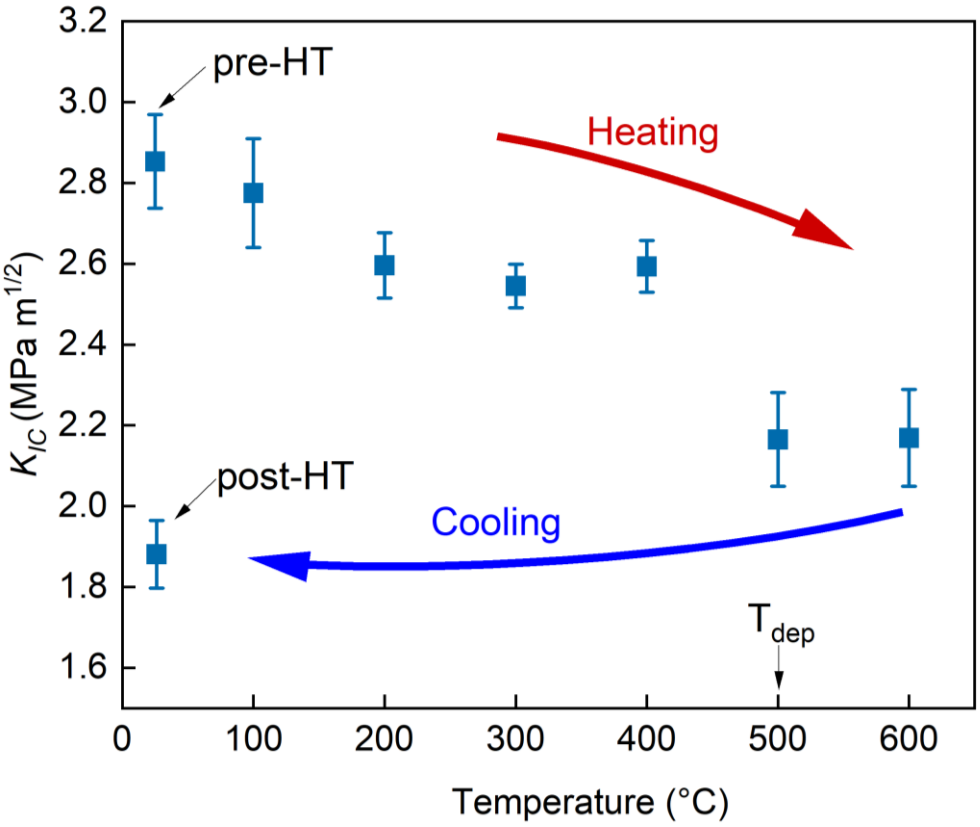

Figure 6.3. The temperature dependence of the fracture toughness K_{IC} of sample S1. The scatter band indicates the standard error of the mean. The individual values are provided in Table 6.2.

Table 6.2. Fracture toughness K_{IC} at different temperature on CrN hard coating.

T/°C	pre-HT	100	200	300	400	500	600	post-HT
K_{IC}/MPa m$^{1/2}$	2.85	2.78	2.60	2.55	2.59	2.17	2.17	1.88
	± 0.12	± 0.14	± 0.08	± 0.05	± 0.06	± 0.12	± 0.12	± 0.08

6.3.2 Influence of constrained annealing on fracture toughness

The fracture toughness after annealing is in all cases lower than in the pre-HT case (see Figure 6.4a). K_{IC} of Case 1 – where FIB-milled cantilevers were annealed – is lowest (1.88 ± 0.08 MPa m$^{1/2}$), followed by Case 2 investigating the freestanding CrN films (2.24 ± 0.11 MPa m$^{1/2}$). Finally, Case 3, where the film was still attached to the substrate, exhibits the highest fracture toughness (2.46 ± 0.07 MPa m$^{1/2}$). Obviously, the sequence of FIB-milling, etching, and annealing influences the fracture toughness, even though intergranular fracture was found in all cases (see Figure 6.4b–e).

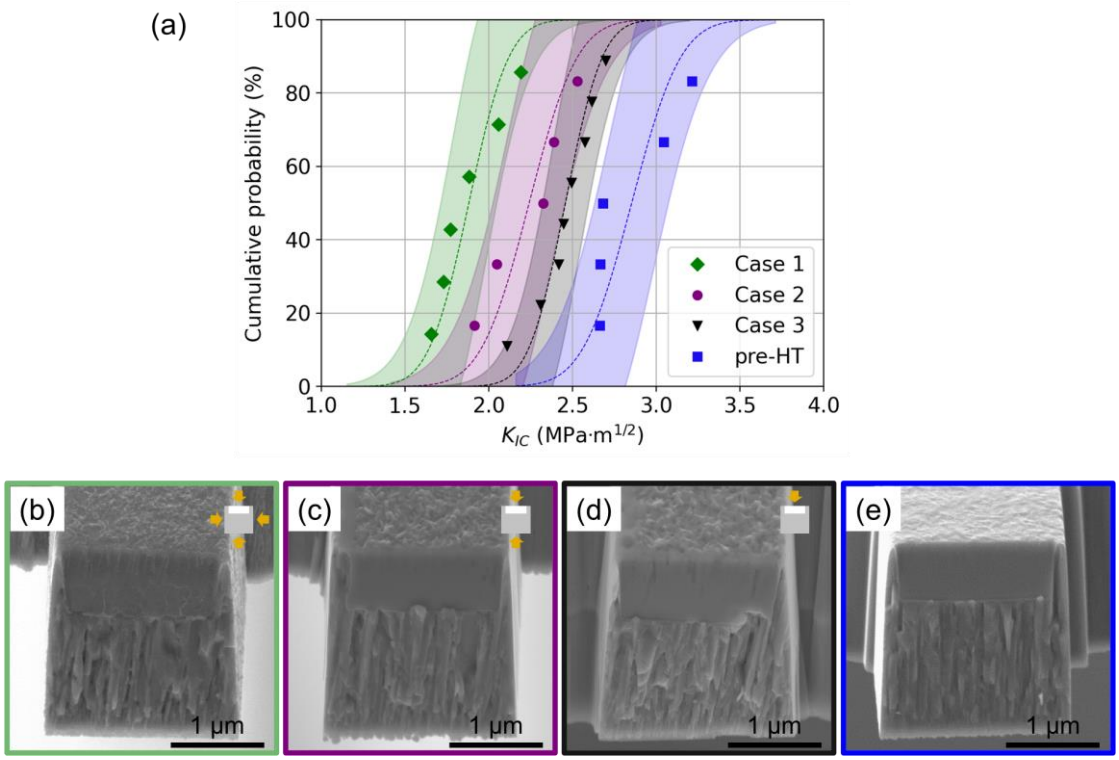

Figure 6.4. (a) Fracture toughness of three cases compared to the as-deposited sample measured at RT. Fracture surface after the testing of (b) Case 1, (c) Case 2, (d) Case 3, and (e) pre-HT.

Cross-sections of the cantilevers after annealing exhibit a considerable number of voids. Their dependence on the distance to the surface was statistically analyzed (see Figure 6.5). It is noteworthy that the distribution of voids in Case 1 is relatively uniform, and Cases 2 and 3 exhibit a distinctive pattern in Figure 6.5. In Case 2, the voids are concentrated at the top and bottom, in proximity to the free surface during annealing. In Case 3, most of the voids are situated in the upper portion of the coating, which corresponds to the top surface being the only free surface during annealing. The density of voids in cases 1, 2, and 3 can be calculated based on the area of voids and the corresponding total area of the cross-section. which is 21.8 ± 0.9‰, 12.0 ± 1.5‰, and 8.7 ± 1.2‰, respectively.

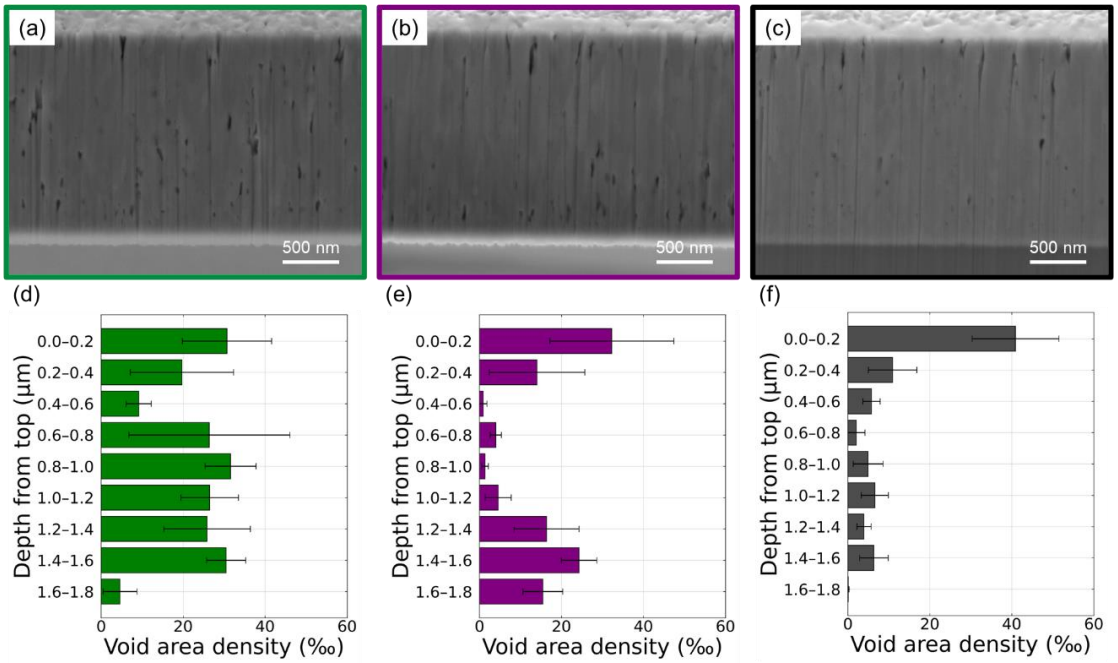

Figure 6.5. The cross-section of (a) Case 1, (b) Case 2, and (c) Case 3 after testing. The area distribution of voids along the thickness direction in (d) Case 1, (e) Case 2, (f) Case 3.

The analysis presented in Figure 6.5 suggests a correlation between the distance to the closest free surface during annealing and the presence of voids in the sample. This is consistent with our observation of higher void densities in samples which had the highest number of free surfaces (void density of Case 1 > Case 2 > Case 3). The void density also correlates with the fracture toughness obtained for the different annealing conditions. Samples with higher void density exhibit lower fracture toughness, while samples with lower void density maintain higher fracture toughness.

6.3.3 The effect of Ga ions on the fracture toughness

To investigate the role of Ga being present during annealing, we compare Case 3 and Case 4, which both exhibit the same sequence of (i) annealing and (ii) cantilever milling; however, in Case 4, additionally, the sample was "washed" with a gentle Ga beam to provide Ga during annealing but to have the same constraint annealing conditions.

As shown by the cumulative probability plots presented in Figure 6.6, the presence of Ga during annealing does not alter the fracture toughness of CrN (compare 2.46 ± 0.07 MPa $m^{1/2}$ for Case 4 and 2.46 ± 0.07 MPa $m^{1/2}$ for Case 3). Consequently, it can be concluded that the observed decline in the K_{IC} of Case 1 – where the fully milled cantilever as annealed – can not be attributed to the diffusion of Ga ions to grain boundaries at elevated temperatures.

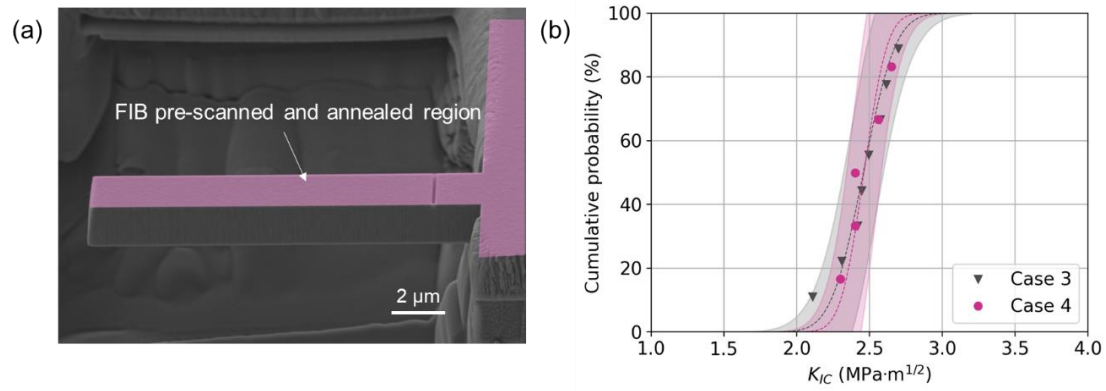

Figure 6.6. (a) Cantilever prepared on FIB pre-scanned and annealed region, (b) the fracture toughness of the FIB pre-scanned (Case 4) and unscanned regions (Case 3) after annealing

6.3.4 Microstructure and composition analysis

The morphology of the sample surface changes as the heating time increases, as shown in Figure 6.7. For instance, in the case of the test conducted at 500 °C and 600 °C, the surface of the last cantilever was observed to be rougher in comparison to the first cantilever.

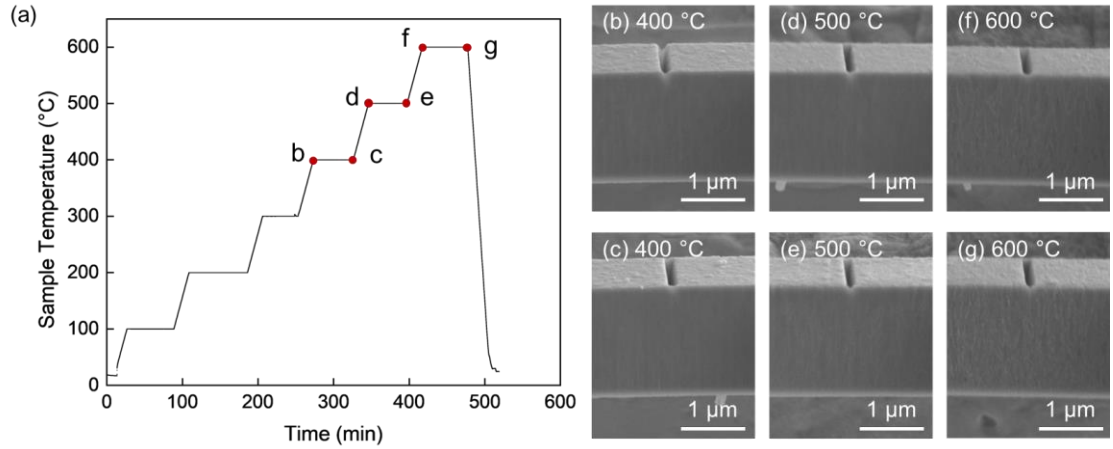

Figure 6.7. Video screenshots of the *in situ* HT bending tests: (a) (d) (c) the first cantilever tested at 400 °C, 500 °C, 600 °C, respectively; (b) (e) (g) the last cantilever tested at 400 °C, 500 °C, 600 °C, respectively.

The surface changes presented in Figure 6.7 are similar to the "beading" phenomenon previously demonstrated by Best et al. [33]. To unravel the beading phenomenon, we prepared TEM lamella samples of pre-HT and post-HT, respectively. The comparison of HAADF STEM imaging and EDS mapping on pre-HT and post-HT lamellas (in Figure 6.8) reveals that the surface of post-HT has a thin O-rich layer (~20 nm), which we attribute to a Cr_2O_3 layer based on selected area electron diffraction patterns (see Figure 6.8c and d). In addition, we noticed that voids were generated along the grain boundaries in the annealed sample, indicated as white arrows in Figure 6.8b.

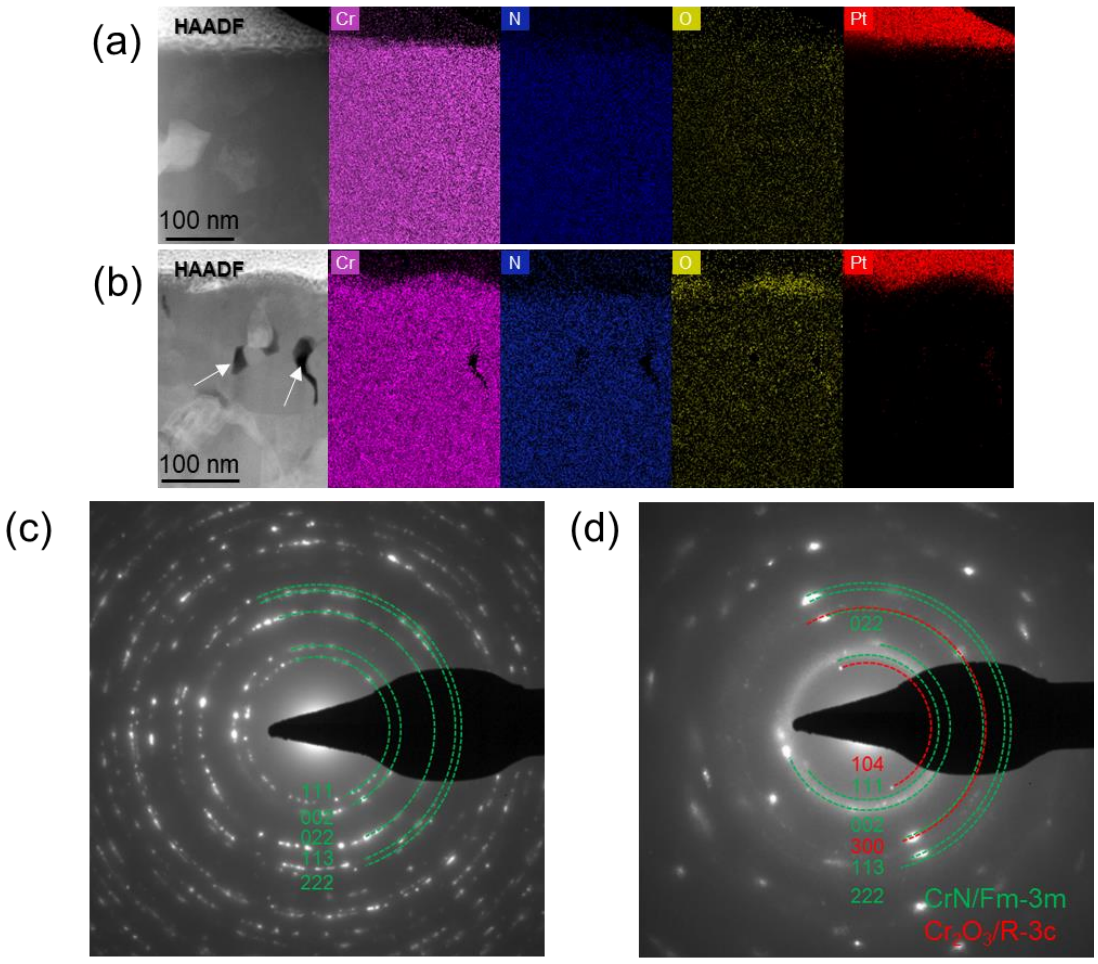

Figure 6.8. HAADF-STEM images and their corresponding EDS mappings of (a) as-deposited sample and (b) annealed sample. Selected area diffraction patterns from (c) as-deposited sample and (d) annealed sample near the surface.

Furthermore, EELS mapping and spectra were used to conduct a comprehensive elemental analysis at the void and grain boundary on the post-HT sample (Figure 6.9). The spectra were obtained from position P1 near the surface to position P5. It was also determined that there is Cr_2O_3 generation according to the peak of O-K and Cr-L [205], and the concentration of oxygen was higher near the void surface, sample surface, and grain boundary. Additionally, Cr and N diffusion were observed towards the surface of the sample, which was also demonstrated in the intensity change of the peak intensity of N and Cr shown in Figure 6.9b. However, it is difficult to determine the phase composition based on the energy loss of the Cr-N peak, as the Cr $L_{2,3}$ edges of Cr_2O_3, CrN, and Cr_2N are very close, and the Cr $L_{2,3}$ edges of CrN and Cr_2N only differ obviously in their L_3/L_2 ratio [206-209].

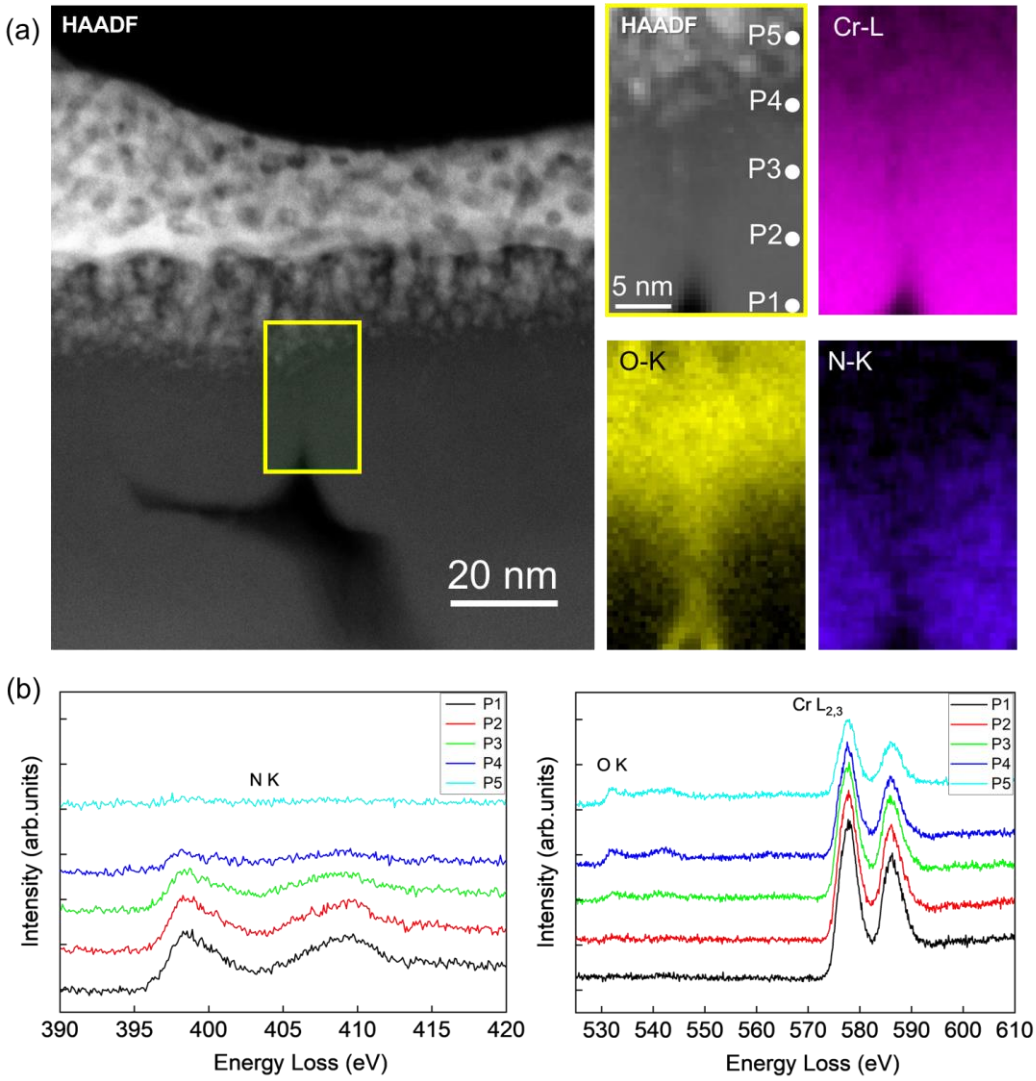

Figure 6.9. (a) HAADF-STEM images and EELS elemental mapping on the post-HT sample, (b) EELS spectra corresponding to different positions (P1-P5).

To identify the temperature at which voids are generated, we heated the film (sample S4) to 500 °C (see Figure 6.10) and held it for one hour, and cooled it back to room temperature (see Figure 6.11). The cross-section of sample S4 indicates that the samples were not yet porous at 500 °C (Figure 6.11c). In contrast, a significant amount of porosity was present in the samples heated up to 600 °C, as illustrated in Figure 6.11f. Furthermore, the sample annealed at 600 °C exhibited a considerable quantity of Cr_2O_3 oxide (Figure 6.11e), whereas a thin Cr_2O_3 oxide layer grows along the grain boundaries, as observed on the samples annealed at 500 °C (Figure 6.11b). This finding is also consistent with the contrast-enhanced observations reported by Best et al. [33].

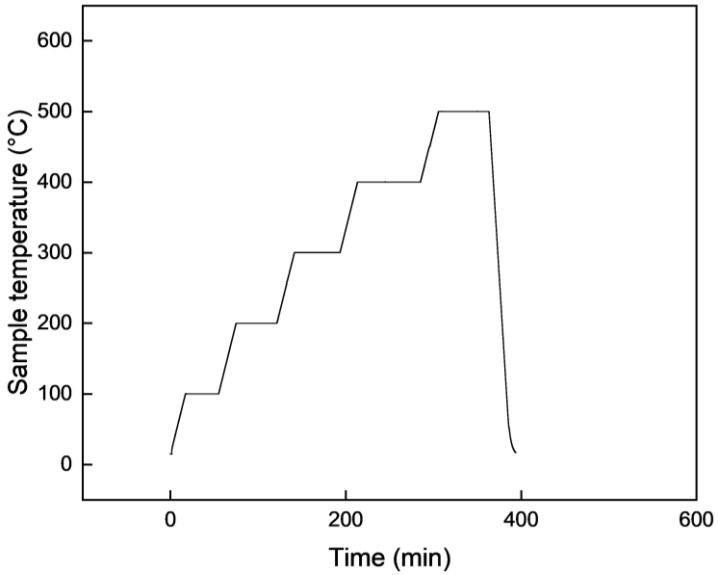

Figure 6.10. The heating curve of sample S4.

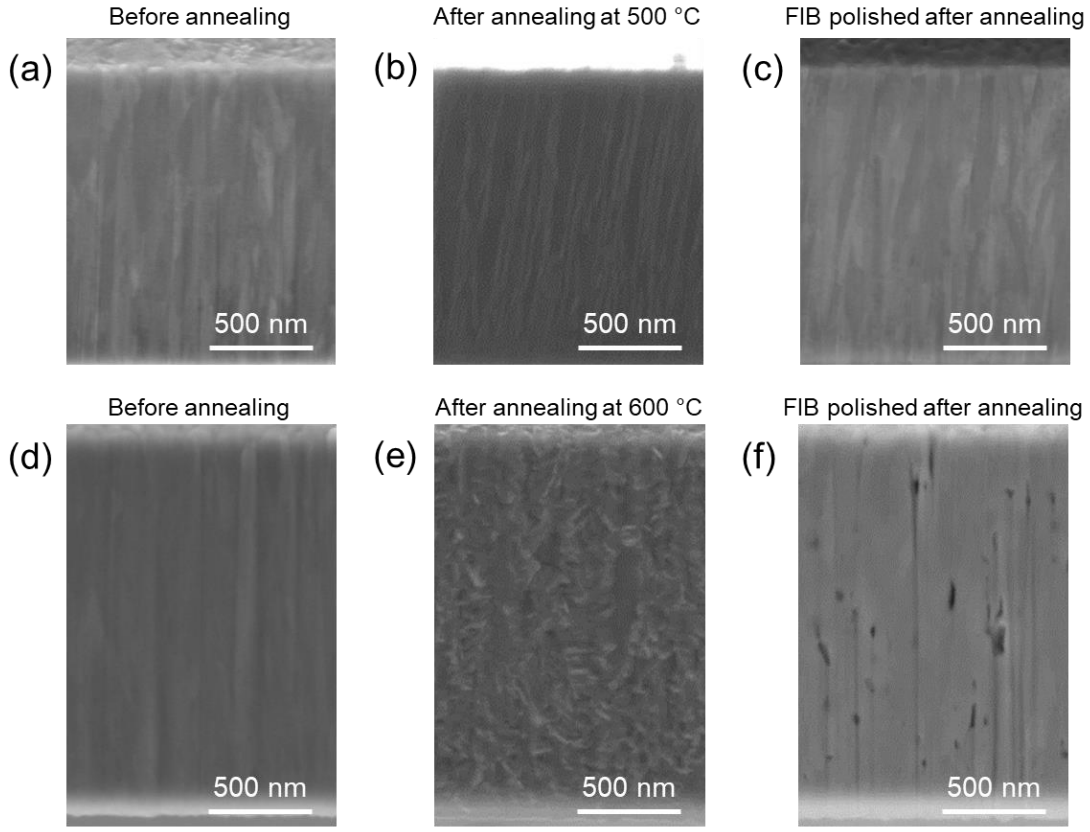

Figure 6.11. The cross-sections before annealing, after annealing, and FIB polished after annealing (a)–(c) at 500 °C; (d)–(f) at 600 °C.

6.4 Discussion

The fracture toughness shows a tremendous decrease with increasing temperature (see Figure 6.3), which does not recover upon cooling to room temperature. By applying 4 different case studies combined with microstructural investigations, we identified the root cause of the mechanical degradation of CrN, which is discussed here.

6.4.1 The formation of voids and oxidation

The TEM micrographs presented in Figure 6.8 and Figure 6.9 document the formation of Cr_2O_3, which is generated at approximately 500 °C along the grain boundary shown in Figure 6.11b. Similarly, previously Cr_2O_3 was identified from X-ray photoelectron spectrometer results after heating at 500 °C for 2 h at a N_2 /H_2=9 atmosphere [210]. The oxidation reaction of CrN is as follows [150, 210]:

$$2CrN_{(s)} + \frac{3}{2}O_{2\,(g)} = Cr_2O_{3\,(s)} + N_{2\,(g)} \tag{6.3}$$

Based on the thermodynamic analysis, the corresponding Gibbs free energy change, ΔG, at 500 °C (773K) under 10^{-5} mbar is [211]:

$$\Delta G = \Delta G^0 + RT ln\left[(pN_2)/\left(pO_2{}^{3/2}\right)\right] = -748\ kJ/mol$$

where ΔG^0 is the change of standard Gibbs free energy, R is the gas constant, T is the absolute temperature, pN_2 is the partial nitrogen pressure, and pO_2 is the partial oxygen pressure. Therefore, this reaction proceeds spontaneously under these conditions. It is worth noting that the oxidation reaction of the coating is also expected to result in the release of nitrogen gas.

The formation of voids during high-temperature exposure (at 600 °C), shown in Figure 6.11f, can be understood through the following sequence, which outlines the key mechanism involved:

Firstly, the aggregation of vacancies play a significant role in the formation of voids. Buchinger et al. found the void formation at the grain boundaries of annealed TiN coatings, which was caused by the defect condensation and annihilation at the grain boundaries [31]. Similarly, the segregation of vacancies (or possible excess N) during annealing also caused the presence of voids at grain boundary triple points of Ti(C,N) coating [124, 212].

Secondly, the released gas during the annealing process also has an important influence on the formation of holes. According to Equation (6.3), there is a release of N_2 gas during the oxidation of CrN, which can lead to the formation of voids [147]. In addition to oxidation, the decomposition reaction of CrN has also been reported to release nitrogen gas [144, 151, 152, 211]. However, in the present study, Cr_2N was not detected after annealing, which is likely due to its eventual oxidation into the more stable Cr_2O_3.

An additional question is whether the compressive residual stress in Case 3 (approximately 3.4 GPa based on the radius of curvature R_c, see Table 6.3) plays any role in the formation of

voids. To isolate the effect of residual stress, a freestanding region with a 1.9 µm coating on top and a Si substrate of approximately 2 µm remaining on the bottom was prepared using FIB, thereby reducing the residual stress significantly compared to the fully constrained coating grown on the Si substrate. Subsequently, both regions on the coating (sample S2) were heated to 600 °C and cooled down to RT. Afterwards, the distribution and density of voids in these two regions with different compressive stresses were compared by preparing cross-sections using FIB, as shown in Figure 6.12. The measured area densities of voids were 6.3 ± 0.5‰ in the constrained region and 6.1 ± 0.7‰ in the freestanding region, and no significant difference is observed within the error bar. Although the residual compressive stresses have been proposed as a potential barrier to diffusion in Cr-N coatings [147], in this study, the small differences in void density cannot be attributed to the compressive stress effects.

Table 6.3. Residual stress of CrN coating.

Coating	R_c [µm]	E_s [GPa]	t_s [µm]	ν_s	t_f [µm]	σ_f [GPa]
CrN on Si	608678.4	130 [213]	362.9	0.28 [213, 214]	1.9	3.4

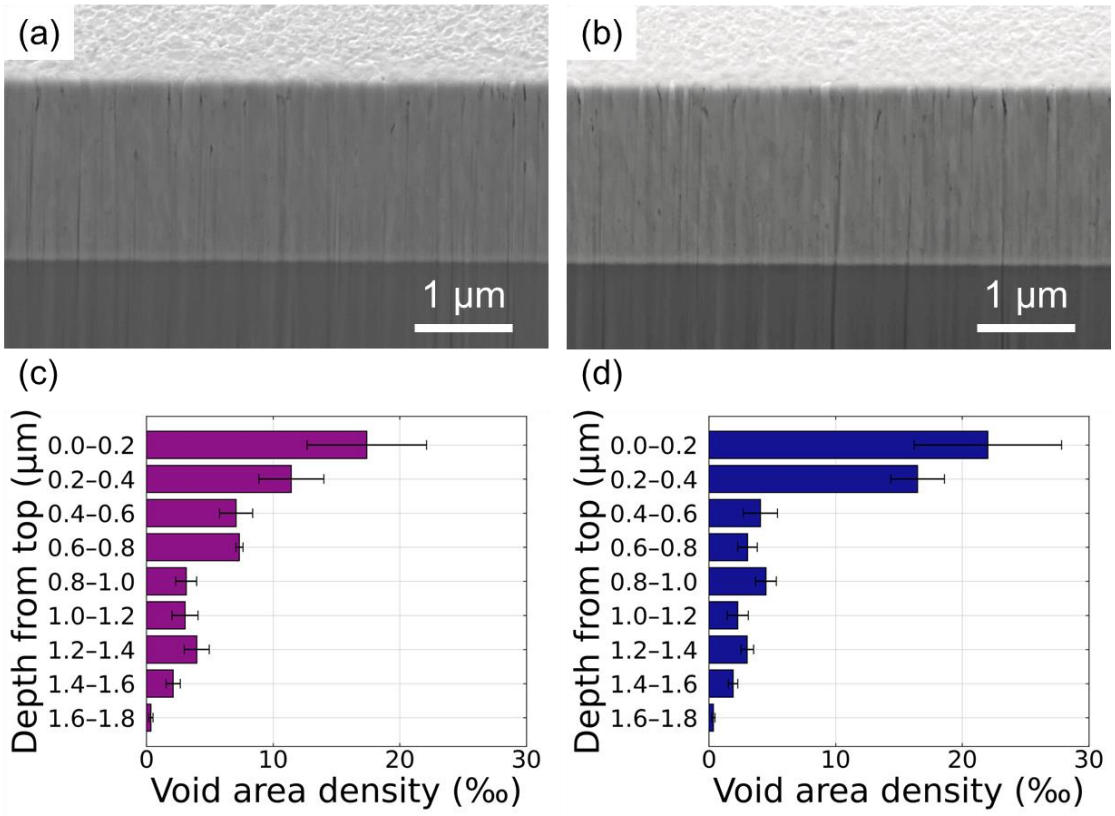

Figure 6.12. Cross-section and voids distribution along the thickness direction of (a), (c) freestanding region and (b), (d) constrained region after annealing at 600 °C.

Furthermore, it was found that the voids are mainly concentrated on the top and bottom surfaces of freestanding cantilevers in Case 2 (Figure 6.5), which is probably related to the concentration gradient of oxygen near the free surface. As the oxidation reaction occurs on the sample surface, the concentration gradient close to it is high [215, 216].

In summary, the formation of voids is likely due to the release of N in the form of nitrogen gas during the decomposition and oxidation of CrN. The aggregation of defects in the coating also promotes the generation of voids at the intersection point of grain boundaries. The grain boundaries are known as effective diffusion pathways, facilitating oxygen diffusion into the underlying microstructure, which subsequently forms a layer of oxidized material on the surface of the voids. Additionally, compressive residual stress does not affect the generation and diffusion of voids.

6.4.2 Role of voids on fracture toughness

The results presented in Section 6.3.2 show that the fracture toughness of the annealed coating decreases with an increasing number of vacuum-exposed free surfaces, while the corresponding void density in the microstructure increases. To clarify how these voids influence the fracture resistance of the coating, the void densities obtained in Figure 6.5 were correlated with the fracture toughness shown in Figure 6.4. The correlation is presented in Figure 6.13.

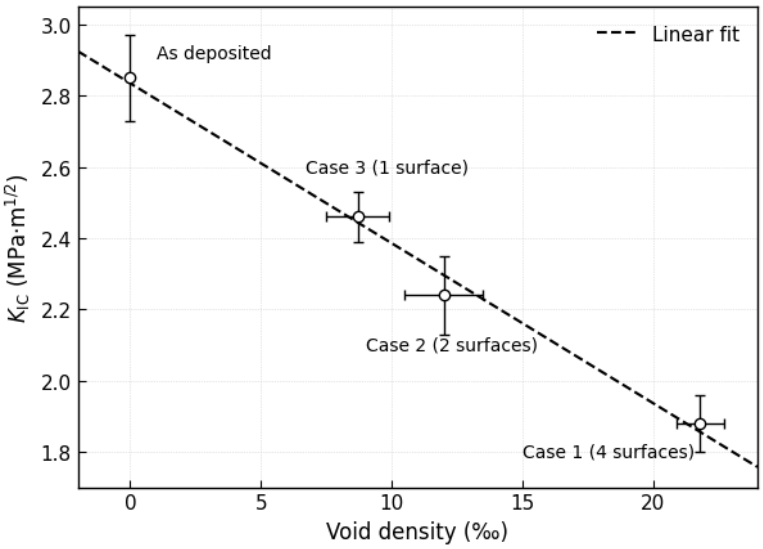

Figure 6.13. Linear decrease of fracture toughness with increasing void density for annealed cases.

A clear inverse relationship is observed between fracture toughness and void density. Samples containing higher void density exhibit lower K_{IC} values. This behavior can be explained by considering that voids act as microstructural defects, which reduce the effective load-bearing area and serve as stress concentration sites for crack initiation and propagation, thereby reducing fracture toughness [217-219].

6.5 Summary and conclusions

This study investigated the influence of annealing states and Ga ions on the fracture toughness of CrN coatings deposited on Si (100) substrates. Bridge notch micro-cantilevers fabricated by FIB were tested *in situ* SEM at a temperature range of RT to 600 °C. A reduction in K_{IC} was observed with increasing temperature, primarily due to time- and temperature-dependent oxidation processes that started around 500 °C and the formation of void occurring between 500 °C and 600 °C. The GBs likely served as diffusion pathways during high-temperature annealing, facilitating the generation of voids at the intersection of GBs and promoting the formation of Cr_2O_3 oxide on the sample surfaces and void surfaces. The residual stress was found not to affect the formation of voids in this system. Notably, comparisons among cantilevers revealed that K_{IC} severely decreases if free surfaces are present during annealing. However, Ga ions introduced during FIB scanning showed no significant impact on K_{IC} after annealing. These findings enhance the understanding of the fracture behavior of the CrN coating under high-temperature conditions, particularly regarding the role of annealing states and Ga ions.

7 Summary and outlook

7.1 Summary

This work aims to understand the effect of GBs on the fracture toughness of hard coatings using a bridge notch micro-cantilever method at both room and elevated temperatures, focusing on the impact of the presence and orientation of GBs at room temperature, and their role at high temperatures.

Prior to the systematic study of GBs, the factor affecting the experimental results during testing was investigated. The first experimental observation of cracking at the bridge notch during single cantilever bending test is presented, demonstrating the feasibility of the strategy of reducing FIB-induced artifacts by employing a bridge-notch geometry that promotes the formation of sharp natural cracks after bridge failure, instead of producing a relatively blunt FIB-milled notch. Additionally, using the measured loads at the bridge failure and final failure, up to three fracture toughness values can be obtained, thereby reducing data scatter.

Using the bridge notch micro-cantilever beam testing method at room temperature and elevated temperature, the effect of GBs on the fracture toughness of hard coatings was systematically studied. (1) The effect of the presence of GBs on the fracture toughness was studied. The reduction in fracture toughness due to the presence of grain boundaries was evaluated, i.e., from 4.1 ± 0.4 MPa $m^{1/2}$ for the epitaxial microstructure to 3.0 ± 0.3 MPa $m^{1/2}$ for the columnar grain structures, a decrease of about 30%. (2) The effect of the columnar GBs orientation was investigated. It was found that when the fracture direction was perpendicular to the growth direction of the coating, successive crack deflections along the grain boundaries occurred, leading to an enhancement of the fracture toughness of approximately 8% compared with test conducted parallel to the growth direction. (3) *In situ* micro-cantilever bending tests were performed on CrN coatings at temperatures ranging from room temperature to 600 °C. The measured K_{IC} values show that high-temperature annealing resulted in a significant reduction in the fracture toughness of the samples. The greater number of free surfaces exposed to vacuum leads to a greater decrease in fracture toughness, which correlates with an increase in void density. It is known that grain boundaries can act as diffusion channels, which may facilitate the formation of Cr_2O_3 oxide and voids at their junctions. These voids may act as stress concentration sites that promote crack initiation and propagation. Additionally, voids will reduce the effective load-bearing area of the material, thereby reducing the fracture toughness of the annealed coating.

7.2 Impact

This study achieved progress in two key aspects. First, it systematically demonstrates that the bridge notch micro-cantilever bending test is an effective fracture testing method at the micro scale that can significantly reduce the influence of FIB artifacts and improve the reliability of fracture toughness measurements. By directly observing crack initiation and arrest at bridges

before the final fracture for the first time, the formation of natural cracks after bridge failure was ensured, which effectively mitigates the impact of FIB artifacts. The fracture toughness obtained from bridge failures reduces the data scatter and provides a methodology for comparing the different microstructures at the right and left bridges within a single specimen. Furthermore, this study also guides the design of bridge-notched samples, ensuring that f_{corr} is less than 1, so that the bridge fracture precedes the final fracture during the experiment. Otherwise, the toughness values may be inaccurately evaluated, especially when the load resolution of the equipment is insufficient to recognize the load drop at the bridge failure. Overall, this work optimized an effective experimental method for the quantitative study of micro-scale fracture behavior.

Second, this investigation qualitatively and quantitatively reveals that grain boundaries are key factors affecting the fracture toughness of hard coatings at ambient temperature and elevated temperature. At room temperature, the presence of grain boundaries in the microstructure significantly weakens fracture toughness. By comparing the epitaxial microstructure and columnar-grained microstructure, the decrease in fracture toughness caused by grain boundaries was quantified. In addition, grain boundary orientation has a significant impact on the crack propagation paths. When the loading direction is perpendicular to the growth direction of the hard coating, the crack continuously deflects along the grain boundaries, thereby improving fracture toughness. This implies that, when grain boundary formation during the deposition process cannot be avoided, grain boundary engineering may represent an effective strategy for toughening hard coatings. At elevated temperature, grain boundaries known as diffusion pathways facilitate oxidation and void formation. The void density correlated with the decrease in fracture toughness by reducing the effective load-bearing area and introducing stress concentration. This result provides insight into understanding the fracture mechanism of hard coatings at high temperature.

7.3 Outlook

Although the *in situ* experimental method of bridge notch micro-cantilevers was optimized to avoid inaccurate evaluation of experimental test results. It should be noted that there is still significant potential for further research. Firstly, current research mainly focuses on micro-cantilever with rectangular cross-sections, while the application of the bridge notch in the micro-cantilevers with other cross-sections has not been studied, such as pentagonal, triangular cross-section. These structures have potential advantages in sample preparation at specific locations, e.g., at specific-oriented grain, or at specific GBs.

Furthermore, the influence of columnar GBs on the fracture toughness of nitride coatings was investigated in this work, but the morphology of GBs is not only columnar grain boundaries studied in this work, but also other forms, such as fine-grained, recrystallized-grained, fibrous-grained, etc. Future research can systematically investigate the influence of different grain boundary characteristics on fracture toughness by controlling grain size, orientation, and distribution. At high temperatures, this study primarily focuses on the CrN system; other nitride, carbide, and multilayer coating systems require further investigation. Additionally, the effect of GBs on the fracture properties of nitride coatings at high temperatures remains to be thoroughly investigated, including the comparison between the epitaxial samples and columnar-grained samples or other GB types of polycrystal samples. This would facilitate an analysis of whether

the fracture properties of the samples would be enhanced in the absence of grain boundaries, and allow for determining the quantitative impact of the presence of GBs on the fracture toughness of hard coatings at high temperature.

8 Appendix

8.1 Contribution of co-authors

Chapter 3: Direct observation of crack arrest after bridge notch failure: A strategy to increase statistics and reduce FIB-artifacts in micro-cantilever testing
Yinxia Zhang: Writing- Original draft preparation, Methodology, Investigation, Formal analysis, Data curation, Visualization.
Matthias Bartosik: Resources, Film deposition, Methodology, Writing- review & editing, Funding acquisition.
Steffen Brinckmann: Writing- review & editing, Funding acquisition, Conceptualization.
Subin Lee: Writing- review & editing, Supervision, Software, Project administration.
Christoph Kirchlechner: Writing- review & editing, Conceptualization, Supervision, Project administration, Funding acquisition.

Chapter 4: Columnar grain boundaries are the weakest link in hard coatings: Insights from micro-cantilever testing
Yinxia Zhang: Writing- Original draft preparation, Methodology, Investigation, Formal analysis, Data curation, Visualization.
Matthias Bartosik: Resources, Film deposition, Methodology, Writing- review & editing, Funding acquisition.
Steffen Brinckmann: Writing- review & editing, Funding acquisition.
Ujjval Bansal: Writing- review & editing, Investigation.
Subin Lee: Writing- review & editing, Supervision, Software, Project administration.
Christoph Kirchlechner: Writing- review & editing, Conceptualization, Supervision, Project administration, Funding acquisition.

Chapter 5: Toughening nitride hard coatings by deflecting cracks along grain boundaries
Yinxia Zhang: Writing- Original draft preparation, Methodology, Investigation, Formal analysis, Data curation, Visualization.
Matthias Bartosik: Resources, Film deposition, Methodology, Writing- review & editing, Funding acquisition.
Steffen Brinckmann: Writing- review & editing, Funding acquisition.
Subin Lee: Writing- review & editing, Supervision, Software, Project administration.
Christoph Kirchlechner: Writing- review & editing, Conceptualization, Supervision, Project administration, Funding acquisition.

Chapter 6: Interplay of oxidation and void formation on degradation of fracture toughness of CrN coatings during thermal exposure
Yinxia Zhang: Writing- Original draft preparation, Methodology, Investigation, Formal analysis, Data curation, Visualization.
Matthias Bartosik: Resources, Film deposition, Methodology, Writing- review & editing, Funding acquisition.

Steffen Brinckmann: Writing- review & editing, Funding acquisition.
Ujjval Bansal: Writing- review & editing, Investigation.
Subin Lee: Writing- review & editing, Supervision, Software, Project administration.
Christoph Kirchlechner: Writing- review & editing, Conceptualization, Supervision, Project administration, Funding acquisition.

8.2 List of publications

2025 **Y. Zhang**, M. Bartosik, S. Brinckmann, U. Bansal, S. Lee, C. Kirchlechner, “Interplay of oxidation and void formation on degradation of fracture toughness of CrN coatings during thermal exposure”, in preparation, 2026

2025 **Y. Zhang**, M. Bartosik, S. Brinckmann, S. Lee, C. Kirchlechner, “Toughening nitride hard coatings by deflecting cracks along grain boundaries”, Mater. Sci. Eng. A (2025) 148392.

2025 **Y. Zhang**, M. Bartosik, S. Brinckmann, U. Bansal, S. Lee, C. Kirchlechner, “Columnar grain boundaries are the weakest link in hard coatings: insights from micro-cantilever testing”, Mater. Res. Lett. (2025) 1-9.

2023 **Y. Zhang**, M. Bartosik, S. Brinckmann, S. Lee, C. Kirchlechner, “Direct observation of crack arrest after bridge notch failure: A strategy to increase statistics and reduce FIB-artifacts in micro-cantilever testing”, Mater. Des. 233 (2023) 112188.

8.3 Permission for reuse of published content

Listed below are the licenses allowing the use of previously published work in the current thesis Ref. [65, 84, 88, 102, 141]. No licenses was required for content use from Refs. [21, 22, 79, 86, 96, 121, 123, 193].

[65] G. Pharr, Measurement of mechanical properties by ultra-low load indentation, Mater. Sci. Eng. A 253(1-2) (1998) 151-159.

This Agreement between Yinxia Zhang ("You") and Elsevier ("Elsevier") consists of your license details and the terms and conditions provided by Elsevier and Copyright Clearance Center.	
License Number	6165301497281
License date	10-Dec-25
Licensed Content Publisher	Elsevier
Licensed Content Publication	Materials Science and Engineering: A
Licensed Content Title	Measurement of mechanical properties by ultra-low load indentation
Licensed Content Author	G.M. Pharr
Licensed Content Date	30-Sep-98
Licensed Content Volume	253
Licensed Content Issue	2-Jan
Licensed Content Pages	9
Type of Use	reuse in a thesis/dissertation
Portion	Figures/tables/illustrations
Number of Figures/tables/illustrations	1
Format	both print and electronic
Are you the author of this Elsevier article?	No
Will you be translating?	No
Title of new work	Dissertation-The effect of grain boundaries on the fracture toughness of hard coatings
Institution name	Karlsruhe Insitute of Technology
Expected presentation date	Mar-26
Portions	Figure 7 on page 156
The Requesting Person / Organization to Appear on the License	Yinxia Zhang
Requestor Location	Yinxia Zhang
	B696 Hermann-von-Helmholtz-Platz 1
	Eggenstein-Leopoldshafen, Not US or Canada 76344
	Germany
Publisher Tax ID	GB 494 6272 12
Total	**0.00 EUR**

[84] D. Sorensen, J. Pischlar, J. Stevick, E. Hintsala, D. Stauffer, J.C. Myers, T. Keenan, A. Ramirez, Investigation of a dissimilar vitreloy 105 to grade 2 titanium laser weld, Mater. Sci. Eng. A 742 (2019) 33-43.

This Agreement between Yinxia Zhang ("You") and Elsevier ("Elsevier") consists of your license details and the terms and conditions provided by Elsevier and Copyright Clearance Center.	
License Number	6165311072925
License date	10-Dec-25
Licensed Content Publisher	Elsevier
Licensed Content Publication	Materials Science and Engineering: A
Licensed Content Title	Investigation of a dissimilar vitreloy 105 to grade 2 titanium laser weld
Licensed Content Author	D. Sorensen,J. Pischlar,J. Stevick,E. Hintsala,D. Stauffer,J.C. Myers,T. Keenan,A.J. Ramirez
Licensed Content Date	10-Jan-19
Licensed Content Volume	742
Licensed Content Issue	n/a
Licensed Content Pages	11
Type of Use	reuse in a thesis/dissertation
Portion	Figures/tables/illustrations
Number of Figures/tables/illustrations	1
Format	both print and electronic
Are you the author of this Elsevier article?	No
Will you be translating?	No
Title of new work	Dissertation-The effect of grain boundaries on the fracture toughness of hard coatings
Institution name	Karlsruhe Insitute of Technology
Expected presentation date	Mar-26
Portions	Figure 5 on page 38
The Requesting Person / Organization to Appear on the License	Yinxia Zhang
Requestor Location	Yinxia Zhang
	B696 Hermann-von-Helmholtz-Platz 1
	Eggenstein-Leopoldshafen, Not US or Canada 76344
	Germany
Publisher Tax ID	GB 494 6272 12
Total	**0.00 EUR**

[88] A. Norton, S. Falco, N. Young, J. Severs, R. Todd, Microcantilever investigation of fracture toughness and subcritical crack growth on the scale of the microstructure in Al2O3, J. Eur. Ceram. Soc. 35(16) (2015) 4521-4533.

This Agreement between Yinxia Zhang ("You") and Elsevier ("Elsevier") consists of your license details and the terms and conditions provided by Elsevier and Copyright Clearance Center.	
License Number	6165311412308
License date	10-Dec-25
Licensed Content Publisher	Elsevier
Licensed Content Publication	Journal of the European Ceramic Society
Licensed Content Title	Microcantilever investigation of fracture toughness and subcritical crack growth on the scale of the microstructure in Al2O3
Licensed Content Author	A.D. Norton,S. Falco,N. Young,J. Severs,R.I. Todd
Licensed Content Date	1-Dec-15
Licensed Content Volume	35
Licensed Content Issue	16
Licensed Content Pages	13
Type of Use	reuse in a thesis/dissertation
Portion	Figures/tables/illustrations
Number of Figures/tables/illustrations	1
Format	both print and electronic
Are you the author of this Elsevier article?	No
Will you be translating?	No
Title of new work	Dissertation-The effect of grain boundaries on the fracture toughness of hard coatings
Institution name	Karlsruhe Insitute of Technology
Expected presentation date	Mar-26
Portions	Figure 9 on page 4527
The Requesting Person / Organization to Appear on the License	Yinxia Zhang
Requestor Location	Yinxia Zhang
	B696 Hermann-von-Helmholtz-Platz 1
	Eggenstein-Leopoldshafen, Not US or Canada 76344
	Germany
Publisher Tax ID	GB 494 6272 12
Total	**0.00 EUR**

[102] S. Liu, J.M. Wheeler, P.R. Howie, X.T. Zeng, J. Michler, W.J. Clegg, Measuring the fracture resistance of hard coatings, Applied Physics Letters 102(17) (2013) 171907.

This Agreement between Yinxia Zhang ("You") and AIP Publishing ("AIP Publishing") consists of your license details and the terms and conditions provided by AIP Publishing and Copyright Clearance Center.	
License Number	6165320083888
License date	10-Dec-25
Licensed Content Publisher	AIP Publishing
Licensed Content Publication	Applied Physics Letters
Licensed Content Title	Measuring the fracture resistance of hard coatings
Licensed Content Author	Liu, S.; Wheeler, J. M.
Licensed Content Date	1-May-13
Licensed Content Volume	102
Licensed Content Issue	17
Type of Use	Thesis/Dissertation
Requestor type	Student
Format	Print and electronic
Portion	Figure/Table
Number of Figures/tables	1
Will you be translating?	No
Title of new work	Dissertation-The effect of grain boundaries on the fracture toughness of hard coatings
Institution name	Karlsruhe Insitute of Technology
Expected presentation date	Mar-26
Portions	Figure 1 on page 102, 171907-1
The Requesting Person / Organization to Appear on the License	Yinxia Zhang
Requestor Location	Yinxia Zhang
	B696 Hermann-von-Helmholtz-Platz 1
	Eggenstein-Leopoldshafen, Not US or Canada 76344
	Germany
Billing Type	Invoice
Billing address	Karlsruher Institut für Technologie
	R224;B696 Hermann-von-Helmholtz-Platz 1
	Eggenstein-Leopoldshafen, Germany 76344
Total	**0.00 EUR**

[141] P.H. Mayrhofer, G. Tischler, C. Mitterer, Microstructure and mechanical/thermal properties of Cr–N coatings deposited by reactive unbalanced magnetron sputtering, Surf. Coat. Technol. 142 (2001) 78-84.

This Agreement between Yinxia Zhang ("You") and Elsevier ("Elsevier") consists of your license details and the terms and conditions provided by Elsevier and Copyright Clearance Center	
License Number	6165320251655
License date	10-Dec-25
Licensed Content Publisher	Elsevier
Licensed Content Publication	Surface and Coatings Technology
Licensed Content Title	Microstructure and mechanical/thermal properties of Cr–N coatings deposited by reactive unbalanced magnetron sputtering
Licensed Content Author	P.H. Mayrhofer,G. Tischler,C. Mitterer
Licensed Content Date	1-Jul-01
Licensed Content Volume	142
Licensed Content Issue	n/a
Licensed Content Pages	7
Type of Use	reuse in a thesis/dissertation
Portion	Figures/tables/illustrations
Number of Figures/tables/illustrations	1
Format	both print and electronic
Are you the author of this Elsevier article?	No
Will you be translating?	No
Title of new work	Dissertation-The effect of grain boundaries on the fracture toughness of hard coatings
Institution name	Karlsruhe Insitute of Technology
Expected presentation date	Mar-26
Portions	Figure 5 on page 81
The Requesting Person / Organization to Appear on the License	Yinxia Zhang
Requestor Location	Yinxia Zhang
	B696 Hermann-von-Helmholtz-Platz 1
	Eggenstein-Leopoldshafen, Not US or Canada 76344
	Germany
Publisher Tax ID	GB 494 6272 12
Total	**0.00 EUR**

8.4 List of prompts

I declare that AI assistance (DeepL Windows App (Version 25.11.4)) was only used for translation. A list of prompts is provided in this section.

Location 1: Kurzfassung Purpose: Translation Prompt: Tanslate the following sentence into german: Hard coatings are widely used under mechanical and thermal loading, where their fracture toughness is crucial for reliable performance. Grain boundaries (GBs) formed during deposition often act as preferred sites for crack initiation and propagation, making their influence on fracture toughness a key factor in coating reliability. To systematically quantify this effect, further development of *in situ* bridge notch micro-cantilever fracture testing is required. A rigid loading setup with high resolution and an in situ scanning electron microscope (SEM) were employed to observe the bridge failure which is widely assumed and predicted, and to determine whether focused ion beam (FIB) artifacts were mitigated by promoting the formation of a natural crack. Based on this developed methodology, the influence of GBs on the fracture toughness of nitride hard coatings was systematically investigated. First, to explore the impact of GB presence, a tailored hard coating was prepared, comprising a columnar-grained layer with GBs and an epitaxial layer without GBs. Second, to study the effect of GB orientation, micro-cantilevers were prepared from columnar-grained nitride coatings with notches oriented parallel or perpendicular to the growth direction of the coating. Third, the role of GBs at elevated temperatures was investigated between 25 °C and 600 °C. Furthermore, the effects of the annealing state of the coating and the Ga ions induced by FIB were studied by post-mortem analysis. This work presented the first experimental observation of bridge notch failure and crack arrest occurring before the fatal fracture of the newly formed through-thickness main notch. As a result, up to three corresponding fracture toughness values could be obtained from a single test, significantly reducing data scatter. The presence of GB leads to a significant reduction in fracture toughness, with a decrease of approximately 30% when comparing columnar-grained to epitaxial microstructures. In addition, When the load was applied perpendicularly to the growth direction of the columnar grains, a continuous crack deflection was observed, increasing in fracture toughness of about 8%, compared with the parallel test. At elevated temperatures, the fracture toughness decreased with increasing temperature. The greater the number of coating surfaces exposed to vacuum, the greater the reduction in fracture toughness. GBs are known to act as diffusion pathways that promote oxidation and void formation, which reduce the effective load-bearing area and introduce stress concentrations, thereby decreasing the fracture toughness of annealed coatings. This systematic investigation demonstrated that GBs significantly influence the fracture toughness of hard coatings at both ambient and elevated temperatures. Description of edition: I proofread and corrected errors.
Location 2: Chapter 2, Paragraph 1 and 2 Purpose: Translation Prompt: Tanslate the following sentence into english:近年来，防护硬质涂层体系的设计与开发取得了显著进展，在提升涂层机械强度、硬度和耐磨性等关键性能指标方面取得了突破性进展。此类硬质涂层的厚度仅为几微米，作为表面工程的核心功能材料，直接决定了部件在极端工况下的使用寿命。然而，值得注意的是，此类硬质涂层材料通常表现出典型的脆性断裂特征，其较低的断裂韧性易在循环载荷和温度作用下引发涂

层体系的裂纹萌生和扩展，最终导致体系整体失效。因此，建立可靠的断裂韧性表征方法，以优化涂层的断裂韧性，已成为提高硬质防护涂层工程性能的关键科学课题。关于脆硬涂层断裂行为的表征，LEFM 的理论框架表现出独特的适用性，使得平面应变断裂韧性的测量在物理上可靠，对工程指导具有价值。
Description of edition: I proofread and corrected errors.

Location 3: Chapter 2, Section 2.1, Paragraph 2–6
Purpose: Translation
Prompt: Tanslate the following sentence into english: LEFM 的起源可以追溯到 20 世纪初 Griffith 的开创性工作。基于先前的研究成果，Griffith 利用能量平衡方法解释了为什么材料会在远低于其理论强度的加载应力下发生断裂。根据 Griffith 的理论，裂纹的扩展取决于裂纹扩展过程中释放的能量是否超过形成新断裂面所需的能量。如果位于无限宽板内的贯穿厚度裂纹受到远场拉应力作用，则所需的断裂应力必须满足以下方程。
后续研究表明，当裂纹尖端发生塑性变形时，会产生相应的能量耗散。Irwin 和 Orowan 分别独立地修正了 Griffith 模型，以考虑单位面积表面产生的塑性功，新的方程如下。后来，Irwin 提出了能量释放率 G 的概念。临界能量释放率 (GC) 的引入包含了表面能和塑性功。
除了从能量的角度理解断裂过程外，Irwin 等人还通过引入应力强度因子来描述线弹性材料裂纹尖端附近的应力分布，从而超越了能量的概念。断裂模式有三种：I 型为张开型，裂纹表面彼此垂直移动；II 型和 III 型分别为滑动型和横向撕裂型。在各向同性线弹性材料中，裂纹尖端前方的应力场可表示如下：对于最常研究的 I 型断裂模式，当应力强度因子 KI 超过临界值时，就会发生断裂。KIC 是材料在平面应变条件下的固有属性。平面应变断裂韧性 KIC 被认为是材料的固有属性，可用于比较不同材料的断裂韧性。为确保有效的平面应变条件，试样尺寸必须满足以下标准。
I 型应力强度因子和断裂韧性的测定可通过标准化试验方法进行，例如紧凑拉伸试样、单边缺口弯曲试样、弯曲试样、圆盘试样和中等强度拉伸板。在每种情况下，试样中的裂纹都是由疲劳引起的，但不同标准的疲劳载荷要求有所不同。
Description of edition: I proofread and corrected errors.

Location 4: Chapter 2, Section 2.2, Paragraph 1 and 2
Purpose: Translation
Prompt: Tanslate the following sentence into english: 值得注意的是，目前尚无评估微/纳米尺度断裂韧性的标准化程序。传统的测试方法通常在宏观尺度上进行。然而，随着微型化材料的出现和材料研究的进步，当样品尺寸达到涂层厚度级别时，传统的拉伸和三点支撑试验方法将难以应用。此外，在微米尺度上，通过疲劳预裂纹获得原子级尖锐缺口的方法通常很有挑战。
先进加工设备和测试平台的发展使得制备微米级样品成为可能，从而促进了微观测试。目前，多种方法被用于评估小尺度下的断裂韧性。这些方法包括 Nanoindentation, pillar splitting, double cantilever bending test, clamped beam bending, single cantilever bending test。其中，单悬臂梁断裂试验因其制备几何形状明确的样品相对简单而成为最普遍的方法。
Description of edition: I proofread and corrected errors.

Location 5: Chapter 2, Section 2.2.1, Paragraph 1 and 2
Purpose: Translation
Prompt: Tanslate the following sentence into english: 在微观尺度上，纳米压痕技术的进步使得评估薄膜和微样品的断裂韧性成为可能。该方法基于通过尖锐压头引入并分析径向裂纹来估算材料的断裂韧性。最初的 LEM 模型是一项开创性工作，公式为。然而，该模型主要适用于脆性块状陶瓷材料，当裂纹几何形状偏离典型的半圆形裂纹时，LEM 模型的精度可能会受到影响。

一般来说，基于压痕的断裂韧性测试方法具有样品制备简单、测试速度快、研究通量高等优点，但也存在一定的局限性。这些局限性包括基体、残余应力、压头几何形状以及裂纹几何形状的多样性对测试结果精度的影响。因此，该方法被认为是一种半定量的材料断裂韧性评价方法，适用于不同材料断裂韧性的初步筛选和相对比较。 Description of edition: I proofread and corrected errors.
Location 6: Chapter 2, Section 2.2.1, Paragraph 1–3 Purpose: Translation Prompt: Tanslate the following sentence into english: 近年来，由于微悬臂梁易于制备且对不同材料具有广泛的适应性，因此在微断裂实验中发挥了重要作用。2005 年，Di Maio 和 Roberts 利用 FIB 技术在硅片上制备了带有凹槽的独立式微悬臂梁，并使用纳米压痕仪对其进行了测试。此后，该方法逐步扩展到对各种材料在不同几何形状和实验条件下的研究，从而获得了丰富的实验数据和理论框架。这些实验甚至与原位 SEM 相结合进行监测，从而可以精确观察裂纹扩展过程。除了 FIB 技术外，化学蚀刻、光刻和飞秒激光烧蚀等技术也被引入以提高加工效率。 FIB-SEM 仪器的灵活性使其能够在样品表面制备各种几何形状的微悬臂梁。其中，五边形和三角形截面等复杂几何形状为研究特定微观结构和界面提供了更多选择。另一方面，矩形梁因其制造简便而被广泛应用。只要试样尺寸满足小塑性变形区域，断裂韧性就可以直接从以下公式确定： 总之，单微悬臂梁断裂实验的发展不仅丰富了断裂力学研究的方法，而且为探索各种材料的微断裂行为提供了一种重要的工具。 Description of edition: I proofread and corrected errors.
Location 7: Chapter 2, Section 2.2.3, Paragraph 1 and 2 Purpose: Translation Prompt: Tanslate the following sentence into english: 近年来，Clamped beam bending 作为一种新型几何方法被应用于小尺寸断裂试验，最初用于研究 Pt,Ni,Al 的断裂韧性。与传统的三点弯曲试验相比，该方法通过夹紧梁的两端并在缺口处施加载荷，实现了纯 I 型加载和可控混合加载。这使得脆性材料中裂纹能够稳定扩展，从而为研究材料的断裂韧性和增韧机制提供了一种新的工具。该方法能够在精确控制加载条件的前提下，实现裂纹的分阶段扩展并在完全失效前停止，并且能够从 FIB 铣削加工的缺口尖端产生真实的裂纹；从而避免了有限缺口根部半径对测量结果的影响。此外，在不同 a/W 比值下获得的 KIC 值变化极小，表明 FIB 对缺口根部的损伤对结果的影响很小。 尽管夹紧梁弯曲试验具有诸多优势，但仍存在以下局限性。首先，残余应力的影响是一个挑战。梁的端部处于非自由状态，导致残余应力对断裂行为产生不可忽略的影响。因此，残余应力值需要独立的测量方法，并在有限元分析中加以考虑。虽然这一特性有助于深入了解材料的实际断裂过程，但不可避免地增加了试验的复杂性。此外，由于应力强度因子（KI）随 a/W 比值的变化并非单调，该方法缺乏解析公式。因此，目前需要通过有限元模拟来提取每次试验的 KI 值，从而增加了实验的计算成本。 Description of edition: I proofread and corrected errors.
Location 8: Chapter 2, Section 2.2.4, Paragraph 1 and 2 Purpose: Translation Prompt: Tanslate the following sentence into english: 传统的 DCB 通常在预裂纹条件下施加弯矩以促进裂纹稳定扩展，类似的原理也可应用于微观尺度研究。Liu 等人利用平冲头施加载荷，成功地研究了具有 DCB 几何结构的 CrN 基硬质涂层的微断裂力学[]。该设计需要满足特定的尺寸比和对称性要求。对称性在该几何结构中尤为关键，因为两个臂的宽度必须相等，并且平冲头压头表面必须完全平行，以确保加载过程符合 I 型加载要求。然而，在对脆性硅材料的测试中观察到，这种几何结构无法支持任何稳定的

裂纹扩展，所有样品在初始裂纹张开后均发生灾难性断裂。这种现象可能是由于裂纹扩展过程中压头中储存的能量自发释放，导致不稳定和灾难性失效。但 KIC 仍可根据最大断裂载荷计算，无需测量裂纹长度。 或者，可以使用 wedge tip 进行加载。然而，与平头相比，wedge tip 会带来更严重的摩擦问题，包括需要对冲头与两个悬臂梁侧壁接触产生的摩擦进行建模，这使得分析更加复杂。为了产生 I 型载荷，wedge tip 必须精确地位于两个悬臂梁的中心。相比之下，平冲头加载避免了摩擦效应引起的复杂分析，也无需确定加载点。 Description of edition: I proofread and corrected errors.
Location 9: Chapter 2, Section 2.2.5, Paragraph 1 Purpose: Translation Prompt: Tanslate the following sentence into english: Micropillar splitting 是一种由 Sebastiani 等人开发的小尺度断裂韧性测量技术，广泛应用于脆性材料的力学性能表征。该方法通过 FIB 制备纵横比大于 1 的微柱样品，并使用尖锐压头进行压入。随着载荷的增加，在临界载荷下裂纹在压头下方成核并扩展至柱表面，随后通过荷载-位移曲线确定临界劈裂荷载，结合柱半径和校准系数, 断裂韧性可通过以下公式来估算。 Description of edition: I proofread and corrected errors.
Location 10:Chapter 2, Section 2.3, Paragraph 1 Purpose: Translation Prompt: Tanslate the following sentence into english: 断裂力学研究中，为了可靠地确定平面应变断裂韧性 KIC，通常需要通过疲劳预裂纹形成原子级尖锐缺口。然而，这在微米长度尺度上难以实现。虽然疲劳预裂纹在宏观尺度上常用于实验，但其引入过程复杂且成功率低，因此微悬臂梁断裂测试中通常 FIB 铣削制作缺口，以实现高精度定位和高效率制备。但由于常用的 Ga 离子 FIB 容易导致 FIB artifacts。 为了减少这些 FIB artifacts，对应的开发出了多样的预凹槽形式，包括 V 形 notch，through notch 和 bridge notch。下面将对这三种形式的 notch 进行对比介绍。 Description of edition: I proofread and corrected errors.
Location 11:Chapter 2, Section 2.3.1, Paragraph 1 and 2 Purpose: Translation Prompt: Tanslate the following sentence into english: 在微尺度断裂测试中，through notch 因其几何形状简单且定义明确而成为一种常用设计，便于通过实验计算断裂韧性，并且适用于脆性和韧性材料。 通常，through notch 是通过在优化的 FIB 条件下沿目标区域进行铣削来制造的。然而，由于样品边缘处 FIB 铣削速率过高，可能导致 over fibbing，因此制造此类缺口极具挑战性。这种现象会导致缺口前沿弯曲而非笔直。反过来，这会增加实验数据的误差和分散性，并使缺口周围的应力场变得复杂。因此，需要高度专业化的技术，通过多步铣削来获得具有笔直裂纹前沿的理想 through notch。虽然 FIB 铣削可以在所需位置产生具有分辨率的尖锐缺口，但缺口尖端的根部半径仍然大于自然裂纹或疲劳裂纹的根部半径。 Description of edition: I proofread and corrected errors.
Location 12:Chapter 2, Section 2.3.2, Paragraph 1 and 2 Purpose: Translation Prompt: Tanslate the following sentence into english: 为了获得原子级的尖的预裂纹，Mueller 等人首次对 quartz 和氧化铝微悬臂梁断裂实验中的人字形缺口进行了系统研究。在这种几何结构中，缺口尖端起到应力集中点的作用，裂纹可以在较低载荷下稳定萌生和扩展，直至达到临界裂纹长度后发生断裂。这种缺口设计不仅能有效诱导尖锐预裂纹的形成，还能减少 FIB 加工引入的 artifacts。

由于其三角形韧带结构，人字形缺口无需在脆性材料的断裂韧性测试中进行疲劳预裂纹处理。然而，在 FIB 铣削过程中难以精确保持人字形缺口的对称性，这可能导致混合模式断裂韧性和裂纹扩展行为的复杂性。因此，在将人字形缺口应用于断裂韧性测试时，仍需充分考虑其局限性。
Description of edition: I proofread and corrected errors.

Location 13:Chapter 2, Section 2.3.3, Paragraph 1 and 2
Purpose: Translation
Prompt: Tanslate the following sentence into english: 为了简化加工工艺、降低制备难度，并有效减少 FIB artifacts，同时引入自然尖锐的预裂纹，Matoy 等人提出了一种创新的 bridge notch 的几何微悬臂梁。该设计通过在 through notch 的边缘保持材料来优化几何形状，如图所示。在加载过程中，由于应力强度因子较高，bridge notch 会首先失效，从而产生尖锐的原子级的预裂纹。这种预裂纹方法已被证明能有效减轻 FIB 加工引起的损伤，从而能够更精确地测量材料的固有特性。
Bridge notch 微悬臂梁已被广泛应用于多种材料体系，包括氮化物涂层、碳化物硬质涂层、氧化硅薄膜和金属间化合物。该设计成功缓解了与 through notch 过度弯曲效应和有限的根半径相关的实验误差，同时提高了加工便捷性并降低了实验分散性。理论上，bridge notch 的设计能够控制加载过程中裂纹的扩展，尤其适用于位移控制系统的测试。这种特性有助于产生自然裂纹，并防止微悬臂梁发生灾难性断裂。然而，bridge notch 微悬臂梁弯曲试验的可靠性取决于缺口几何形状的优化。不合适的几何参数可能导致没有 bridge notch 的预先失效，而立即发生完全的断裂，从而导致断裂韧性的误判。因此，为了确保试验结果的可靠性，有必要进一步研究如何确保 bridge notch 失效发生在最终断裂之前，从而在最终断裂之前引入自然预裂纹。第三章将对此问题进行深入研究和分析。
Description of edition: I proofread and corrected errors.

Location 14:Chapter 2, Section 2.4, Paragraph 1 and 2
Purpose: Translation
Prompt: Tanslate the following sentence into english: 氮化物涂层是一种高性能表面保护材料，具有诸多显著优势，其中最主要的是其优异的机械性能和耐腐蚀性，使其在多个工业领域得到实际应用，例如半导体技术中的扩散阻挡层、切削刀具和机械部件上的耐磨层。值得注意的是，此类保护涂层通常需要承受复杂的机械载荷，并在高温环境下长期保持稳定的使用性能。
然而，采用物理气相沉积技术制备的氮化物涂层通常具有热力学不稳定的微观结构，包含点缺陷、位错和亚晶粒。在高温环境下，这些不稳定的微观结构会通过点缺陷迁移、位错 annihilation 和晶界迁移等动态过程耗散能量，从而引起涂层体系的微观结构演变，例如回复、晶粒长大和再结晶行为。此外，氮化物涂层的热稳定性还涉及氧化和相分解反应等关键过程。近期研究表明，硬质涂层体系在高温下的力学性能与其微观结构的演变以及化学成分在高温下的稳定性之间存在显著相关性。这些发现强调了研究氮化物涂层热稳定机制的必要性，这对于提高涂层材料在极端条件下的可靠性具有重要意义。
Description of edition: I proofread and corrected errors.

Location 15:Chapter 2, Section 2.4.1, Paragraph 1 and 2
Purpose: Translation
Prompt: Tanslate the following sentence into english: 作为涂层热处理的初始过程，回复是指在新的无应力晶粒出现之前发生的一系列退火现象。这些现象包括点缺陷的迁移和合并、位错的重排和 annihilation 以及亚晶粒的生长和聚合。回复过程的主要驱动力是涂层内部的温度和应力。回复效应的研究通常通过原位测量高温下的应力来实现。研

究发现，热处理过程中发生的应力松弛与涂层在沉积态下的双轴应力呈线性关系，如图所示。 涂层中固有残余应力的状态会显著影响其在退火或回复过程中的行为。涂层因沉积过程中形成的空隙或空位缺陷而产生拉应力时.。离子轰击可以用于致密化，并引入压应力。此外，这种拉应力不仅不会在退火过程中释放，反而可能由于回复效应而进一步增加。这是因为热能会诱导晶格中的点缺陷迁移到晶界或其他缺陷聚集区域，缺陷的累积会导致局部体积收缩，进而引发涂层整体拉应力的增加。相反，回复过程通常可以显著降低涂层中原本处于压应力状态的压应力。回复促进应力释放和原子重排，从而有效降低压应力。因此，涂层中初始残余应力的类型不仅决定了其在沉积和后处理过程中的力学响应，而且直接影响其后续的稳定性和使用性能。了解和控制这种固有的残余应力是优化涂层微观结构和力学性能的重要途径。 Description of edition: I proofread and corrected errors.
Location 16:Chapter 2, Section 2.4.2, Paragraph 1 Purpose: Translation Prompt: Tanslate the following sentence into english: 再结晶是指在微观结构的特定区域形成新的几乎无应力晶粒的过程。这些晶粒随后生长并取代含有缺陷的区域，其动力学过程类似于相变，其中形核标志着新晶粒的初始形成，而生长则取代原始晶粒。再结晶需要足够的热激活和驱动力。对于硬质涂层，再结晶行为差异很大。例如，CrN 涂层稳定性极差，通常在相对较低的温度（400-550℃）下以等轴 Cr_2N 晶粒的形式再结晶。相反，TiAlN 涂层表现出很高的稳定性，在 900℃退火 2 小时后未检测到再结晶。DSC 是精确测定再结晶起始温度的有效方法。然而，对于晶粒尺寸较大的单相涂层，其再结晶和晶粒生长所释放的能量，用 DSC 无法充分量化。 Description of edition: I proofread and corrected errors.
Location 17:Chapter 2, Section 2.4.3, Paragraph 1 Purpose: Translation Prompt: Tanslate the following sentence into english: 在大多数物理气相沉积工艺中，低能离子辐照被广泛用于控制薄膜生长过程中的微观结构和化学成分。然而，尽管离子轰击对致密化和成分控制具有积极作用，但它也可能带来一些潜在的不利影响，包括产生点缺陷、掺杂惰性气体以及引入过量的氮。这些缺陷和杂质会导致涂层处于强烈的非平衡状态，并促进亚稳相或非平衡结构特征的形成。这种非平衡结构会诱导扩散驱动力，进一步影响材料的稳定性和性能。此外，氮化物中的杂质或晶格点缺陷会因合成所用的沉积工艺而异。这些特性预计会显著影响金属或氮物种在氮化物中的扩散率。然而，氮化物陶瓷的高熔点使扩散测量变得复杂，并且常常限制了合适的放射性示踪剂的可用性。通常，Cr-N 涂层中的微观和宏观应力会影响 Cr 的体扩散。沉积过程中形成的缺陷通常会引起拉应力，从而降低扩散势垒，促进 Cr 原子在氮化物基体中的迁移。相反，某些缺陷会促进压应力的形成，阻碍晶格原子的运动，从而抑制 Cr 的体扩散。至于氮，其扩散速率远高于金属原子，这与其较小的原子半径密切相关。 Description of edition: I proofread and corrected errors.
Location 18:Chapter 2, Section 2.4.4, Paragraph 1 Purpose: Translation Prompt: Tanslate the following sentence into english: 氮化物涂层的氧化行为已被广泛研究。例如，Cr-N 涂层在高达 1000℃的氧化气氛中的氧化行为和机理一直是众多研究的重点。氧与 CrN 和 Cr2N 相的一般反应如下：Mayrhofer 等人在氧化气氛下，采用动态和等温 TGA 研究了 Cr-N 涂层的抗氧化性能和氧化动力学，测量了不同阶段氧化反应的活化能，并发现其氧化行为与其双轴宏观应力、化学成分和材料固有性质有关。此

外，许多因素也会影响氮化物涂层的氧化动力学，例如吸附、成核、晶体生长、化学吸附等。
Description of edition: I proofread and corrected errors.

Location 19:Chapter 2, Section 2.4.5, Paragraph 1–4
Purpose: Translation
Prompt: Tanslate the following sentence into english: 氮化物涂层在高温下也容易发生热分解，其分解受气氛、沉积方法和加热过程的影响。Ernst 等人在氩气气氛下，利用 TGA-DTA 技术研究了 CrN 涂层，结果表明，CrN 涂层在室温至 1440℃ 的温度范围内经历了两个分解过程（步骤 1：CrN → Cr2N，步骤 2：Cr2N → Cr）。第一步的分解温度范围为 925℃至 1118℃，加热速率和沉积方法是影响该温度的主要因素。然而，第二步的分解温度高于 1200℃，且与沉积方法无关，仅对加热速率敏感。
此外，Almer 等人采用 XRD 研究了在氩气气氛中不同温度下 CrN 涂层的相组成，结果表明在约 400℃处出现了 Cr2N300 峰。相比之下，Wu 等人发现，Cr2N 涂层在炉中于 900℃下暴露 5 小时后，会生成 CrN 相。他们提出了一种假设，即存在从 Cr2N 到 CrN 的相变，相关反应如式所示，Mayrhofer 等人也观察到了这一现象：
根据热力学原理，Cr2N 和 CrN 的稳定性受温度和氮气分压的影响。这解释了为什么 Cr-N 涂层在不同气氛下的稳定性不同，以及为什么在 Ar 气氛下高温时可以在 CrN 涂层中观察到 Cr2N 相。
本节所介绍的概念与机制为本研究提供了必要的理论与方法论基础。LEFM 构建了微悬臂梁断裂分析的整体框架；对多种微尺度测试方法的介绍明确了各自的优势与局限性，说明单微悬臂梁弯曲测试在微尺度力学研究中具有广泛适用性。对不同缺口类型的回顾表明，桥式缺口在减少 FIB artifacts 并实现自然裂纹生成方面具有显著优势，但仍需进一步研究以确保桥失效能够在最终断裂发生前可靠地引入自然预裂纹。此外，关于氮化物涂层热稳定性的讨论为理解本研究中晶界在高温条件下对断裂行为的影响提供了关键背景支撑。
Description of edition: I proofread and corrected errors.

References

[1] M. Tkadletz, N. Schalk, R. Daniel, J. Keckes, C. Czettl, C. Mitterer, Advanced characterization methods for wear resistant hard coatings: a review on recent progress, Surf. Coat. Technol. 285 (2016) 31-46.
[2] A. Iost, R. Bigot, Hardness of coatings, Surf. Coat. Technol. 80(1-2) (1996) 117-120.
[3] T. Hoornaert, Z. Hua, J. Zhang, Hard wear-resistant coatings: A review, Advanced Tribology: Proceedings of CIST2008 & ITS-IFToMM2008 (2010) 774-779.
[4] C. Mitterer, P. Mayrhofer, J. Musil, Thermal stability of PVD hard coatings, Vacuum 71(1-2) (2003) 279-284.
[5] K. Bobzin, High-performance coatings for cutting tools, CIRP J. Manuf. Sci. Technol. 18 (2017) 1-9.
[6] K.-D. Bouzakis, N. Michailidis, G. Skordaris, E. Bouzakis, D. Biermann, R. M'Saoubi, Cutting with coated tools: Coating technologies, characterization methods and performance optimization, CIRP annals 61(2) (2012) 703-723.
[7] O. Fayomi, O. Agboola, I. Akande, A. Emmanuel, Challenges of coatings in aerospace, automobile and marine industries, AIP Conference Proceedings, AIP Publishing, 2020.
[8] P. Visser, H. Terryn, J.M.C. Mol, Aerospace Coatings, in: J.M.C.M. A.E. Hughes, M.L. Zheludkevich, R.G. Buchheit (Ed.), Active Protective Coatings, Springer, Dordrecht, 2016, pp. 315-372.
[9] J.A. Stewart, D.E. Spearot, Phase-field simulations of microstructure evolution during physical vapor deposition of single-phase thin films, Comput. Mater. Sci. 131 (2017) 170-177.
[10] J.A. Thornton, High rate thick film growth, Annu. Rev. Mater. Sci. 7(1) (1977) 239-260.
[11] D. Rickerby, S. Bull, Engineering with surface coatings: The role of coating microstructure, Surf. Coat. Technol. 39 (1989) 315-328.
[12] A. Raveh, I. Zukerman, R. Shneck, R. Avni, I. Fried, Thermal stability of nanostructured superhard coatings: a review, Surf. Coat. Technol. 201(13) (2007) 6136-6142.
[13] J. Musil, Hard nanocomposite coatings: Thermal stability, oxidation resistance and toughness, Surf. Coat. Technol. 207 (2012) 50-65.
[14] C. Starling, J. Branco, Thermal fatigue of hot work tool steel with hard coatings, Thin Solid Films 308 (1997) 436-442.
[15] T. Wang, X. Zha, F. Chen, J. Wang, Y. Li, F. Jiang, Mechanical impact test methods for hard coatings of cutting tools: a review, The International Journal of Advanced Manufacturing Technology 115 (2021) 1367-1385.
[16] S. Bose, High temperature coatings, Butterworth-Heinemann2017.
[17] J. Ast, M. Ghidelli, K. Durst, M. Göken, M. Sebastiani, A.M. Korsunsky, A review of experimental approaches to fracture toughness evaluation at the micro-scale, Mater. Des. 173 (2019) 107762.
[18] R. Pippan, S. Wurster, D. Kiener, Fracture mechanics of micro samples: Fundamental considerations, Mater. Des. 159 (2018) 252-267.
[19] J. Ast, J. Schwiedrzik, N. Rohbeck, X. Maeder, J. Michler, Novel micro-scale specimens for mode-dependent fracture testing of brittle materials: A case study on GaAs single crystals, Mater. Des. 193 (2020) 108765.
[20] K.I. Schiffmann, Determination of fracture toughness of bulk materials and thin films by nanoindentation: comparison of different models, Philosophical Magazine 91(7-9) (2011) 1163-1178.
[21] M. Sebastiani, K.E. Johanns, E.G. Herbert, F. Carassiti, G.M. Pharr, A novel pillar indentation splitting test for measuring fracture toughness of thin ceramic coatings, Philosophical Magazine 95(16-18) (2015) 1928-1944.

[22] N. Jaya B, V. Jayaram, S.K. Biswas, A new method for fracture toughness determination of graded (Pt,Ni)Al bond coats by microbeam bend tests, Philosophical Magazine 92(25-27) (2012) 3326-3345.
[23] B. Lawn, Fracture of Brittle Solids, second ed., Cambridge University Press, Cambridge, 1993.
[24] D. Di Maio, S.G. Roberts, Measuring fracture toughness of coatings using focused-ion-beam-machined microbeams, J. Mater. Res. 20(2) (2005) 299-302.
[25] J. Schaufler, C. Schmid, K. Durst, M. Göken, Determination of the interfacial strength and fracture toughness of aC: H coatings by in-situ microcantilever bending, Thin Solid Films 522 (2012) 480-484.
[26] S. Rajsiri, B.W. Kempshall, S.M. Schwarz, L.A. Giannuzzi, FIB Damage in Silicon: Amorphization or Redeposition?, Microsc. Microanal. 8(S02) (2002) 50-51.
[27] R. Hugo, R. Hoagland, Gallium penetration of aluminum: in-situ TEM observations at the penetration front, Scr. Mater. 41(12) (1999) 1341-1346.
[28] J.P. Best, J. Zechner, I. Shorubalko, J.V. Oboňa, J. Wehrs, M. Morstein, J. Michler, A comparison of three different notching ions for small-scale fracture toughness measurement, Scr. Mater. 112 (2016) 71-74.
[29] K. Matoy, H. Schönherr, T. Detzel, T. Schöberl, R. Pippan, C. Motz, G. Dehm, A comparative micro-cantilever study of the mechanical behavior of silicon based passivation films, Thin Solid Films 518(1) (2009) 247-256.
[30] Y. Xiao, Y. Zou, H. Ma, A.S. Sologubenko, X. Maeder, R. Spolenak, J.M. Wheeler, Nanostructured NbMoTaW high entropy alloy thin films: High strength and enhanced fracture toughness, Scr. Mater. 168 (2019) 51-55.
[31] J. Buchinger, L. Löfler, J. Ast, A. Wagner, Z. Chen, J. Michler, Z. Zhang, P.H. Mayrhofer, D. Holec, M. Bartosik, Fracture properties of thin film TiN at elevated temperatures, Mater. Des. 194 (2020) 108885.
[32] A. Riedl, R. Daniel, M. Stefenelli, T. Schöberl, O. Kolednik, C. Mitterer, J. Keckes, A novel approach for determining fracture toughness of hard coatings on the micrometer scale, Scr. Mater. 67(7-8) (2012) 708-711.
[33] J.P. Best, J. Zechner, J.M. Wheeler, R. Schoeppner, M. Morstein, J. Michler, Small-scale fracture toughness of ceramic thin films: the effects of specimen geometry, ion beam notching and high temperature on chromium nitride toughness evaluation, Philosophical Magazine 96(32-34) (2016) 3552-3569.
[34] S. Zhang, D. Sun, Y. Fu, H. Du, Toughening of hard nanostructural thin films: a critical review, Surf. Coat. Technol. 198(1-3) (2005) 2-8.
[35] P.H. Mayrhofer, C. Mitterer, L. Hultman, H. Clemens, Microstructural design of hard coatings, Progress in Materials Science 51(8) (2006) 1032-1114.
[36] N. Schalk, M. Tkadletz, C. Mitterer, Hard coatings for cutting applications: Physical vs. chemical vapor deposition and future challenges for the coatings community, Surf. Coat. Technol. 429 (2022) 127949.
[37] M.F. Montemor, Functional and smart coatings for corrosion protection: A review of recent advances, Surf. Coat. Technol. 258 (2014) 17-37.
[38] A.M. Merlo, The contribution of surface engineering to the product performance in the automotive industry, Surf. Coat. Technol. 174 (2003) 21-26.
[39] R.O. Ritchie, The conflicts between strength and toughness, Nat. Mater. 10(11) (2011) 817-822.
[40] Y.X. Wang, S. Zhang, Toward hard yet tough ceramic coatings, Surf. Coat. Technol. 258 (2014) 1-16.
[41] B.R. Lawn, D.B. Marshall, Brittle solids: from physics and chemistry to materials applications, Annual Review of Materials Research 52(1) (2022) 441-471.

[42] K.-D. Bouzakis, A. Siganos, T. Leyendecker, G. Erkens, Thin hard coatings fracture propagation during the impact test, Thin Solid Films 460(1-2) (2004) 181-189.
[43] L.P. Pook, Linear elastic fracture mechanics for engineers: theory and applications, WIT press2000.
[44] C.E. Inglis, Stresses in a plate due to the presence of cracks and sharp corners, Trans Inst Naval Archit 55 (1913) 219-241.
[45] J.W. Gibbs, On the equilibrium of heterogeneous substances, (1879).
[46] A.A. Griffith, The phenomena of rupture and flow in solids, Philosophical transactions of the royal society of london. Series A, containing papers of a mathematical or physical character 221(582-593) (1921) 163-198.
[47] G.R. Irwin, Fracture dynamics, Fracturing of Metals. American Society of Metals, Fracturing of Metals, American Society for Metals, Cleveland, OH, 1948, pp. 147-166.
[48] E. Orowan, Fracture and strength of solids, Rep. Prog. Phys. 12(1) (1949) 185.
[49] T.L. Anderson, Fracture mechanics: fundamentals and applications, third ed., CRC Press, Boca Raton, 2005.
[50] G.R. Irwin, The historical development of our understanding of fracture, JOM-WARRENDALE- 49 (1997) 38-41.
[51] G.R. Irwin, Onset of fast crack propagation in high strength steel and aluminum alloys, Sagamore Research Conference Proceedings 2 (1956) 289–305.
[52] G.R. Irwin, Analysis of Stresses and Strains Near the End of a Crack Traversing a Plate, J. Appl. Mech. 24(3) (1957) 361-364.
[53] H.M. Westergaard, Bearing Pressures and Cracks: Bearing Pressures Through a Slightly Waved Surface or Through a Nearly Flat Part of a Cylinder, and Related Problems of Cracks, J. Appl. Mech. 6(2) (1939) A49-A53.
[54] I.N. Sneddon, The distribution of stress in the neighbourhood of a crack in an elastic solid, Proceedings of the Royal Society of London. Series A. Mathematical and Physical Sciences 187(1009) (1946) 229-260.
[55] M.L. Williams, On the Stress Distribution at the Base of a Stationary Crack, J. Appl. Mech. 24(1) (1957) 109-114.
[56] ASTM E399-90 Standard test method for plane-strain fracture toughness of metallic materials, Annual book of ASTM standards1997.
[57] S. Suresh, L. Ewart, M. Maden, W. Slaughter, M. Nguyen, Fracture toughness measurements in ceramics: pre-cracking in cyclic compression, Journal of materials science 22 (1987) 1271-1276.
[58] K. Taguchi, K. Nakadate, S. Matsuo, K. Tokunaga, H. Kurishita, Fatigue pre-cracking and fracture toughness in polycrystalline tungsten and molybdenum, J. Nucl. Mater. 498 (2018) 445-457.
[59] J. Luksch, A. Lambai, G. Mohanty, F. Schaefer, C. Motz, Bridging macro to micro-scale fatigue crack growth by advanced fracture mechanical testing on the meso-scale, Mater. Sci. Eng. A 884 (2023) 145452.
[60] K. Takashima, S. Koyama, K. Nakai, Y. Higo, Development of fatigue pre-cracking method into micro-sized specimens for measuring Fracture Toughness, MRS Online Proceedings Library (OPL) 741 (2002) J3. 3.
[61] B.N. Jaya, V. Jayaram, Fracture testing at small-length scales: from plasticity in Si to brittleness in Pt, JOM 68 (2016) 94-108.
[62] D. Harding, W. Oliver, G. Pharr, Cracking during nanoindentation and its use in the measurement of fracture toughness, MRS Online Proceedings Library (OPL) 356 (1994) 663.
[63] G. Anstis, P. Chantikul, B.R. Lawn, D. Marshall, A critical evaluation of indentation techniques for measuring fracture toughness: I, direct crack measurements, J. Am. Ceram. Soc. 64(9) (1981) 533-538.

[64] P. Peralta, S. Maloy, F. Chu, J. Petrovic, T. Mitchell, Mechanical properties of monocrystalline $C11_b$ $MoSi_2$ with small aluminum additions, Scr. Mater. 37(10) (1997).
[65] G. Pharr, Measurement of mechanical properties by ultra-low load indentation, Mater. Sci. Eng. A 253(1-2) (1998) 151-159.
[66] N. Cuadrado, D. Casellas, M. Anglada, E. Jiménez-Piqué, Evaluation of fracture toughness of small volumes by means of cube-corner nanoindentation, Scr. Mater. 66(9) (2012) 670-673.
[67] R.D. Dukino, M.V. Swain, Comparative measurement of indentation fracture toughness with Berkovich and Vickers indenters, J. Am. Ceram. Soc. 75(12) (1992) 3299-3304.
[68] B. Lawn, R. Wilshaw, Indentation fracture: principles and applications, Journal of Materials Science 10(6) (1975) 1049-1081.
[69] A.G. Evans, E.A. Charles, Fracture Toughness Determinations by Indentation, J. Am. Ceram. Soc. 59(7-8) (1976) 371-372.
[70] D.B. Marshall, B.R. Lawn, Residual stress effects in sharp contact cracking, Journal of Materials Science 14(8) (1979) 2001-2012.
[71] B.R. Lawn, A.G. Evans, D.B. Marshall, Elastic/Plastic Indentation Damage in Ceramics: The Median/Radial Crack System, J. Am. Ceram. Soc. 63(9-10) (1980) 574-581.
[72] R.F. Cook, G.M. Pharr, Direct observation and analysis of indentation cracking in glasses and ceramics, J. Am. Ceram. Soc. 73(4) (1990) 787-817.
[73] M. Laugier, Palmqvist indentation toughness in WC-Co composites, J. Mater. Sci. Lett. 6 (1987) 897-900.
[74] J. Chen, Indentation-based methods to assess fracture toughness for thin coatings, J. Phys. D: Appl. Phys. 45(20) (2012) 203001.
[75] J.-i. Jang, G.M. Pharr, Influence of indenter angle on cracking in Si and Ge during nanoindentation, Acta Mater. 56(16) (2008) 4458-4469.
[76] E. Okotete, S. Mück, S. Lee, C. Kirchlechner, Evaluating neon ions as an alternative to gallium in micro cantilevers fracture testing, Scr. Mater. 258 (2025) 116509.
[77] M.J. Pfeifenberger, M. Mangang, S. Wurster, J. Reiser, A. Hohenwarter, W. Pfleging, D. Kiener, R. Pippan, The use of femtosecond laser ablation as a novel tool for rapid micro-mechanical sample preparation, Mater. Des. 121 (2017) 109-118.
[78] D. Sheeja, B.K. Tay, L. Yu, D.H. Chua, W. Milne, J. Miao, Y.Q. Fu, Fabrication of amorphous carbon cantilever structures by isotropic and anisotropic wet etching methods, Diamond Relat. Mater. 12(9) (2003) 1495-1499.
[79] B.S. Li, T.J. Marrow, S.G. Roberts, D.E.J. Armstrong, Evaluation of Fracture Toughness Measurements Using Chevron-Notched Silicon and Tungsten Microcantilevers, JOM 71(10) (2019) 3378-3389.
[80] D. Armstrong, A. Wilkinson, S. Roberts, Micro-mechanical measurements of fracture toughness of bismuth embrittled copper grain boundaries, Philos. Mag. Lett. 91(6) (2011) 394-400.
[81] J. Ast, B. Matthey, P. Herre, S. Höhn, M. Herrmann, S. Christiansen, Micro-cantilever testing of diamond-silicon carbide interfaces in silicon carbide bonded diamond materials produced by reactive silicon infiltration, Open Ceramics 8 (2021) 100176.
[82] Y. Deng, T. Hajilou, A. Barnoush, Hydrogen-enhanced cracking revealed by in situ micro-cantilever bending test inside environmental scanning electron microscope, Philosophical Transactions of the Royal Society A: Mathematical, Physical and Engineering Sciences 375(2098) (2017) 20170106.
[83] D. Sorensen, E. Hintsala, J. Stevick, J. Pischlar, B. Li, D. Kiener, J.C. Myers, H. Jin, J. Liu, D. Stauffer, Intrinsic toughness of the bulk-metallic glass Vitreloy 105 measured using micro-cantilever beams, Acta Mater. 183 (2020) 242-248.
[84] D. Sorensen, J. Pischlar, J. Stevick, E. Hintsala, D. Stauffer, J.C. Myers, T. Keenan, A. Ramirez, Investigation of a dissimilar vitreloy 105 to grade 2 titanium laser weld, Mater. Sci. Eng. A 742 (2019) 33-43.

[85] A. Alvaro, I.T. Jensen, N. Kheradmand, O. Løvvik, V. Olden, Hydrogen embrittlement in nickel, visited by first principles modeling, cohesive zone simulation and nanomechanical testing, Int. J. Hydrogen Energy 40(47) (2015) 16892-16900.
[86] M.G. Mueller, G. Žagar, A. Mortensen, Stable room-temperature micron-scale crack growth in single-crystalline silicon, J. Mater. Res. 32(19) (2017) 3617-3626.
[87] G. Žagar, V. Pejchal, M.G. Mueller, L. Michelet, A. Mortensen, Fracture toughness measurement in fused quartz using triangular chevron-notched micro-cantilevers, Scr. Mater. 112 (2016) 132-135.
[88] A. Norton, S. Falco, N. Young, J. Severs, R. Todd, Microcantilever investigation of fracture toughness and subcritical crack growth on the scale of the microstructure in Al2O3, J. Eur. Ceram. Soc. 35(16) (2015) 4521-4533.
[89] R. Soler, S. Gleich, C. Kirchlechner, C. Scheu, J.M. Schneider, G. Dehm, Fracture toughness of Mo2BC thin films: Intrinsic toughness versus system toughening, Mater. Des. 154 (2018) 20-27.
[90] B. Völker, B. Stelzer, S. Mráz, H. Rueß, R. Sahu, C. Kirchlechner, G. Dehm, J.M. Schneider, On the fracture behavior of Cr2AlC coatings, Mater. Des. 206 (2021) 109757.
[91] Y. Zou, P. Okle, H. Yu, T. Sumigawa, T. Kitamura, S. Maiti, W. Steurer, R. Spolenak, Fracture properties of a refractory high-entropy alloy: In situ micro-cantilever and atom probe tomography studies, Scr. Mater. 128 (2017) 95-99.
[92] R. Daniel, M. Meindlhumer, J. Zalesak, B. Sartory, A. Zeilinger, C. Mitterer, J. Keckes, Fracture toughness enhancement of brittle nanostructured materials by spatial heterogeneity: A micromechanical proof for CrN/Cr and TiN/SiOx multilayers, Mater. Des. 104 (2016) 227-234.
[93] S. Gabel, S. Giese, R.U. Webler, S. Neumeier, M. Göken, Micro‐cantilever fracture tests of α‐Cr containing NiAl bond coats, Adv. Eng. Mater. (2022).
[94] F. Iqbal, J. Ast, M. Göken, K. Durst, In situ micro-cantilever tests to study fracture properties of NiAl single crystals, Acta Mater. 60(3) (2012) 1193-1200.
[95] S. Brinckmann, K. Matoy, C. Kirchlechner, G. Dehm, On the influence of microcantilever pre-crack geometries on the apparent fracture toughness of brittle materials, Acta Mater. 136 (2017) 281-287.
[96] Y. Zhang, M. Bartosik, S. Brinckmann, U. Bansal, S. Lee, C. Kirchlechner, Columnar grain boundaries are the weakest link in hard coatings: insights from micro-cantilever testing, Mater. Res. Lett. (2025) 1-9.
[97] B.N. Jaya, V. Jayaram, Crack stability in edge-notched clamped beam specimens: modeling and experiments, International Journal of Fracture 188(2) (2014) 213-228.
[98] F.Y. Cui, R.P. Vinci, A chevron-notched bowtie micro-beam bend test for fracture toughness measurement of brittle materials, Scr. Mater. 132 (2017) 53-57.
[99] B.N. Jaya, C. Kirchlechner, G. Dehm, Can microscale fracture tests provide reliable fracture toughness values? A case study in silicon, J. Mater. Res. 30(5) (2015) 686-698.
[100] F.W. DelRio, S.J. Grutzik, W.M. Mook, S.M. Dickens, P.G. Kotula, E.D. Hintsala, D.D. Stauffer, B.L. Boyce, Eliciting stable nanoscale fracture in single-crystal silicon, Mater. Res. Lett. 10(11) (2022) 728-735.
[101] G. Sernicola, T. Giovannini, P. Patel, J.R. Kermode, D.S. Balint, T.B. Britton, F. Giuliani, In situ stable crack growth at the micron scale, Nature Communications 8(1) (2017).
[102] S. Liu, J.M. Wheeler, P.R. Howie, X.T. Zeng, J. Michler, W.J. Clegg, Measuring the fracture resistance of hard coatings, Appl. Phys. Lett. 102(17) (2013) 171907.
[103] L. Mei, X. Guo, K. Jin, Characterization of mechanical property degradation of ion-irradiated materials, Frontiers in Materials 9 (2022) 849209.
[104] M. Ghidelli, M. Sebastiani, K.E. Johanns, G.M. Pharr, Effects of indenter angle on micro‐scale fracture toughness measurement by pillar splitting, J. Am. Ceram. Soc. 100(12) (2017) 5731-5738.

[105] C.M. Lauener, L. Petho, M. Chen, Y. Xiao, J. Michler, J.M. Wheeler, Fracture of Silicon: Influence of rate, positioning accuracy, FIB machining, and elevated temperatures on toughness measured by pillar indentation splitting, Mater. Des. 142 (2018) 340-349.
[106] M.Z. Mughal, R. Moscatelli, H.-Y. Amanieu, M. Sebastiani, Effect of lithiation on micro-scale fracture toughness of LixMn2O4 cathode, Scr. Mater. 116 (2016) 62-66.
[107] J.P. Best, J. Wehrs, M. Polyakov, M. Morstein, J. Michler, High temperature fracture toughness of ceramic coatings evaluated using micro-pillar splitting, Scr. Mater. 162 (2019) 190-194.
[108] M. Sebastiani, K. Johanns, E.G. Herbert, G.M. Pharr, Measurement of fracture toughness by nanoindentation methods: Recent advances and future challenges, Curr. Opin. Solid State Mater. Sci. 19(6) (2015) 324-333.
[109] E. Okotete, Stable crack growth geometries as a strategy to circumvent FIB artefacts in small scale fracture testing, Karlsruher Institut für Technologie (KIT), 2024.
[110] J. Luksch, A. Lambai, G. Mohanty, C. Pauly, F. Schaefer, C. Motz, Size effects in fatigue crack growth in confined volumes: A microbending case study on nanocrystalline nickel, Mater. Des. 241 (2024) 112880.
[111] K. Takashima, Y. Higo, Fatigue and fracture of a Ni–P amorphous alloy thin film on the micrometer scale, Fatigue & fracture of engineering materials & structures 28(8) (2005) 703-710.
[112] E. Salvati, L. Brandt, C. Papadaki, H. Zhang, S. Mousavi, D. Wermeille, A. Korsunsky, Nanoscale structural damage due to focused ion beam milling of silicon with Ga ions, Mater. Lett. 213 (2018) 346-349.
[113] T.L. Matteson, S.W. Schwarz, E.C. Houge, B.W. Kempshall, L.A. Giannuzzi, Electron backscattering diffraction investigation of focused ion beam surfaces, J. Electron. Mater. 31(1) (2002) 33-39.
[114] S. Lee, J. Jeong, Y. Kim, S.M. Han, D. Kiener, S.H. Oh, FIB-induced dislocations in Al submicron pillars: Annihilation by thermal annealing and effects on deformation behavior, Acta Mater. 110 (2016) 283-294.
[115] D. Kiener, C. Motz, M. Rester, M. Jenko, G. Dehm, FIB damage of Cu and possible consequences for miniaturized mechanical tests, Mater. Sci. Eng. A 459(1-2) (2007) 262-272.
[116] Y. Liao, M. Gruber, H. Lukic, S. Chen, S. Megremis, Fracture toughness of zirconia with a nanometer size notch fabricated using focused ion beam milling, Journal of Biomedical Materials Research Part B: Applied Biomaterials 108(8) (2020) 3323-3330.
[117] S. Wurster, C. Motz, R. Pippan, Characterization of the fracture toughness of micro-sized tungsten single crystal notched specimens, Philosophical Magazine 92(14) (2012) 1803-1825.
[118] M. Mueller, V. Pejchal, G. Žagar, A. Singh, M. Cantoni, A. Mortensen, Fracture toughness testing of nanocrystalline alumina and fused quartz using chevron-notched microbeams, Acta Mater. 86 (2015) 385-395.
[119] L. Chao, D. Singh, D. Shetty, Effects of subcritical crack growth on fracture toughness of ceramics assessed in chevron-notched three-point bend tests, (1989).
[120] J. Underwood, S. Freiman, F. Baratta, A review of chevron-notched fracture specimens, Chevron-notched Specimens, Testing and Stress Analysis: A Symposium, ASTM International, 1984, p. 5.
[121] K. Kishida, T. Maruyama, T. Fukuyama, H. Inui, Micropillar compression deformation of single crystals of α-Nb5Si3 with the tetragonal D8 l structure, Science and Technology of Advanced Materials 21(1) (2020) 805-816.
[122] B. Philippi, K. Matoy, J. Zechner, C. Kirchlechner, G. Dehm, Fracture toughness of intermetallic Cu6Sn5 in lead-free solder microelectronics, Scr. Mater. 123 (2016) 38-41.
[123] Y. Zhang, M. Bartosik, S. Brinckmann, S. Lee, C. Kirchlechner, Direct observation of crack arrest after bridge notch failure: A strategy to increase statistics and reduce FIB-artifacts in micro-cantilever testing, Mater. Des. 233 (2023) 112188.
[124] L. Hultman, Thermal stability of nitride thin films, Vacuum 57(1) (2000) 1-30.

[125] J. Jagielski, A. Khanna, J. Kucinski, D. Mishra, P. Racolta, P. Sioshansi, E. Tobin, J. Thereska, V. Uglov, T. Vilaithong, Effect of chromium nitride coating on the corrosion and wear resistance of stainless steel, Appl. Surf. Sci. 156(1-4) (2000) 47-64.
[126] L. Rocha, E. Ariza, J. Ferreira, F. Vaz, E. Ribeiro, L. Rebouta, E. Alves, A. Ramos, P. Goudeau, J. Rivière, Structural and corrosion behaviour of stoichiometric and substoichiometric TiN thin films, Surf. Coat. Technol. 180 (2004) 158-163.
[127] C. Mitterer, F. Holler, F. Üstel, D. Heim, Application of hard coatings in aluminium die casting—soldering, erosion and thermal fatigue behaviour, Surf. Coat. Technol. 125(1-3) (2000) 233-239.
[128] H. Schulz, J. Dörr, I. Rass, M. Schulze, T. Leyendecker, G. Erkens, Performance of oxide PVD-coatings in dry cutting operations, Surf. Coat. Technol. 146 (2001) 480-485.
[129] C. Kirchlechner, K. Martinschitz, R. Daniel, M. Klaus, C. Genzel, C. Mitterer, J. Keckes, Residual stresses and thermal fatigue in CrN hard coatings characterized by high-temperature synchrotron X-ray diffraction, Thin Solid Films 518(8) (2010) 2090-2096.
[130] P.H. Mayrhofer, C. Mitterer, Structure/property relations in PVD hard coatings, in: S.G. Pandalai (Ed.), Recent Research Developments in Vacuum Science & Technology, Transworld research network, Trivandrum, 2003, pp. 71-97.
[131] P. Mayrhofer, F. Kunc, J. Musil, C. Mitterer, A comparative study on reactive and non-reactive unbalanced magnetron sputter deposition of TiN coatings, Thin Solid Films 415(1-2) (2002) 151-159.
[132] J. Wheeler, R. Raghavan, V. Chawla, M. Morstein, J. Michler, Deformation of hard coatings at elevated temperatures, Surf. Coat. Technol. 254 (2014) 382-387.
[133] S.-K. Tien, J.-G. Duh, Effect of heat treatment on mechanical properties and microstructure of CrN/AlN multilayer coatings, Thin Solid Films 494(1-2) (2006) 173-178.
[134] C. Tang, M. Steinbrück, M. Grosse, S. Ulrich, M. Stüber, The Effect of Annealing Temperature on the Microstructure and Properties of Cr–C–Al Coatings on Zircaloy-4 for Accident-Tolerant Fuel (ATF) Applications, Coatings 12(2) (2022) 167.
[135] W. Herr, E. Broszeit, The influence of a heat treatment on the microstructure and mechanical properties of sputtered coatings, Surf. Coat. Technol. 97(1-3) (1997) 335-340.
[136] R. Hahn, M. Bartosik, M. Arndt, P. Polcik, P.H. Mayrhofer, Annealing effect on the fracture toughness of CrN/TiN superlattices, Int. J. Refract. Met. Hard Mater. 71 (2018) 352-356.
[137] A. Drnovšek, H.T. Vo, M.R. de Figueiredo, S. Kolozsvári, P. Hosemann, R. Franz, High temperature fracture toughness of single-layer CrAlN and CrAlSiN hard coatings, Surf. Coat. Technol. 409 (2021) 126909.
[138] M. Monclús, L. Yang, I. López-Cabañas, M. Castillo-Rodríguez, A. Zaman, J. Wang, E. Meletis, R. González-Arrabal, J. Llorca, J. Molina-Aldareguía, High temperature mechanical properties and microstructure of hard TaSiN coatings, Mater. Sci. Eng. A 797 (2020) 139976.
[139] J.D. Verhoeven, Fundamentals of physical metallurgy, Wiley, New York, 1975.
[140] W.D. Nix, Mechanical properties of thin films, Metall. Trans. A 20 (1989) 2217-2245.
[141] P.H. Mayrhofer, G. Tischler, C. Mitterer, Microstructure and mechanical/thermal properties of Cr–N coatings deposited by reactive unbalanced magnetron sputtering, Surf. Coat. Technol. 142 (2001) 78-84.
[142] E. Machlin, Materials Science in Microelectronics, Giro Press1995.
[143] F.J. Humphreys, M. Hatherly, Recrystallization and related annealing phenomena, elsevier2012.
[144] J. Almer, M. Odén, L. Hultman, G. Håkansson, Microstructural evolution during tempering of arc-evaporated Cr–N coatings, J. Vac. Sci. Technol. A 18(1) (2000) 121-130.
[145] R. Andrievski, I. Anisimova, V. Anisimov, V. Makarov, V. Popova, Grain size and recrystallization of TiN, ZrN, NbN, and CrN alloyed and multilayer films, Thin Solid Films 261(1-2) (1995) 83-86.

[146] K. Detert, Secondary recrystallization, in: F. Haessner (Ed.), Recrystallization of metallic materials, Dr. Riederer Verlag GmbH, Stuttgart, 1978, pp. 97-109.
[147] P. Mayrhofer, H. Willmann, C. Mitterer, Oxidation kinetics of sputtered Cr–N hard coatings, Surf. Coat. Technol. 146 (2001) 222-228.
[148] H. Matzke, Diffusion in Carbides and Nitrides: Unsolved Problems, Defect and Diffusion Forum 83 (1992) 111-130.
[149] S. Hofmann, H. Jehn, Oxidation behavior of CrNx and (Cr, Al) Nx hard coatings, Mater. Corros. 41(12) (1990) 756-760.
[150] J. Wu, M. Shen, W. Wang, Y. Wang, Y. Cheng, S. Zhu, Insight into oxidation difference between Cr2N and CrN coatings, Surfaces and Interfaces (2024) 104626.
[151] W. Ernst, J. Neidhardt, H. Willmann, B. Sartory, P.H. Mayrhofer, C. Mitterer, Thermal decomposition routes of CrN hard coatings synthesized by reactive arc evaporation and magnetron sputtering, Thin Solid Films 517(2) (2008) 568-574.
[152] H.-Y. Chen, F.-H. Lu, Phase transformation in chromium nitride films, J. Vac. Sci. Technol. A 21(3) (2003) 695-700.
[153] G. Dehm, B.N. Jaya, R. Raghavan, C. Kirchlechner, Overview on micro-and nanomechanical testing: New insights in interface plasticity and fracture at small length scales, Acta Mater. 142 (2018) 248-282.
[154] D. Di Maio, S. Roberts, Measuring fracture toughness of coatings using focused-ion-beam-machined microbeams, Journal of materials research 20(2) (2005) 299-302.
[155] K. Kishida, T. Maruyama, H. Matsunoshita, T. Fukuyama, H. Inui, Micropillar compression deformation of single crystals of Mo5SiB2 with the tetragonal D8l structure, Acta Mater. 159 (2018) 416-428.
[156] S. Gabel, B. Merle, E. Bitzek, M. Göken, A new method for microscale cyclic crack growth characterization from notched microcantilevers and application to single crystalline tungsten and a metallic glass, J. Mater. Res. 37(12) (2022) 2061–2072.
[157] D. Cohen-Tanugi, N. Yao, Superior imaging resolution in scanning helium-ion microscopy: A look at beam-sample interactions, J. Appl. Phys. 104(6) (2008) 063504.
[158] H. Wu, L.A. Stern, D. Xia, D. Ferranti, B. Thompson, K.L. Klein, C.M. Gonzalez, P.D. Rack, Focused helium ion beam deposited low resistivity cobalt metal lines with 10 nm resolution: implications for advanced circuit editing, Journal of Materials Science: Materials in Electronics 25(2) (2014) 587-595.
[159] F.I. Allen, N.R. Velez, R.C. Thayer, N.H. Patel, M.A. Jones, G.F. Meyers, A.M. Minor, Gallium, neon and helium focused ion beam milling of thin films demonstrated for polymeric materials: study of implantation artifacts, Nanoscale 11(3) (2019) 1403-1409.
[160] R. Danzer, T. Lube, P. Supancic, R. Damani, Fracture of ceramics, Adv. Eng. Mater. 10(4) (2008) 275-298.
[161] K. Kanaya, K. Adachi, K. Yonehara, Y. Muranaka, H. Ishikawa, Quantitative analysis of knock-on and thermal damage of biological specimens by electron irradiation in transmission electron microscopy, Micron and microscopica acta 22(3) (1991) 223-237.
[162] P. Sidky, M. Hocking, Review of inorganic coatings and coating processes for reducing wear and corrosion, Br. Corros. J. 34(3) (1999) 171-183.
[163] P. Miller, J. Holladay, Friction and wear properties of titanium, Wear 2(2) (1958) 133-140.
[164] P.H. Mayrhofer, R. Rachbauer, D. Holec, F. Rovere, J. Schneider, Protective transition metal nitride coatings, in: S. Hashmi, G.F. Batalha, C.J.V. Tyne, B. Yilbas (Eds.), Comprehensive Materials Proceedings, Elsevier, Oxford, 2014, pp. 355-388.
[165] K.T. Faber, A.G. Evans, Crack deflection processes—I. Theory, Acta Metall. 31(4) (1983) 565-576.
[166] G.T. Hahn, The Influence of Microstructure on Brittle Fracture Toughness, Metall. Trans. A 15(6) (1984) 947-959.

[167] H. Gopalan, A. Marshal, M. Hans, D. Primetzhofer, N. Cautaerts, B. Breitbach, B. Völker, C. Kirchlechner, J.M. Schneider, G. Dehm, On the interplay between microstructure, residual stress and fracture toughness of (Hf-Nb-Ta-Zr) C multi-metal carbide hard coatings, Mater. Des. 224 (2022) 111323.
[168] M.R. Schoof, S. Karimi Aghda, C.F. Kusche, M. Hans, J.M. Schneider, S. Korte-Kerzel, J.S.K.L. Gibson, The influence of microstructural orientation on fracture toughness in (V, Al)N and (V, Al)(O, N) coatings as measured by microcantilever bending, J. Mater. Res. 38(16) (2023) 3950-3965.
[169] L. Liu, Q. Ruan, Z. Wu, T. Li, W. Zuo, C. Huang, Y. Wu, Z. Wu, R.K. Fu, P.K. Chu, Hard and tough CrN coatings strengthened by high-density distorted coherent grain boundaries, J. Alloy. Compd. 894 (2022) 162139.
[170] M. Meindlhumer, T. Ziegelwanger, J. Zalesak, M. Hans, L. Löfler, S. Spor, N. Jäger, A. Stark, H. Hruby, R. Daniel, Precipitation-based grain boundary design alters Inter-to Trans-granular Fracture in AlCrN Thin Films, Acta Mater. 237 (2022) 118156.
[171] R. Daniel, M. Meindlhumer, W. Baumegger, J. Zalesak, B. Sartory, M. Burghammer, C. Mitterer, J. Keckes, Grain boundary design of thin films: using tilted brittle interfaces for multiple crack deflection toughening, Acta Mater. 122 (2017) 130-137.
[172] Y. Zhang, M. Bartosik, S. Brinckmann, S. Lee, C. Kirchlechner, Toughening nitride hard coatings by deflecting cracks along grain boundaries, Materials Science and Engineering: A 935 (2025) 148392.
[173] T. Glechner, S. Lang, R. Hahn, M. Alfreider, V. Moraes, D. Primetzhofer, J. Ramm, S. Kolozsvári, D. Kiener, H. Riedl, Correlation between fracture characteristics and valence electron concentration of sputtered Hf-CN based thin films, Surf. Coat. Technol. 399 (2020) 126212.
[174] A.K. Mishra, H. Gopalan, M. Hans, C. Kirchlechner, J. Schneider, G. Dehm, B.N. Jaya, Strategies for damage tolerance enhancement in metal/ceramic thin films: Lessons learned from Ti/TiN, Acta Mater. 228 (2022) 117777.
[175] J.S.-L. Gibson, S. Rezaei, H. Rueß, M. Hans, D. Music, S. Wulfinghoff, J.M. Schneider, S. Reese, S. Korte-Kerzel, From quantum to continuum mechanics: studying the fracture toughness of transition metal nitrides and oxynitrides, Mater. Res. Lett. 6(2) (2018) 142-151.
[176] N.G. Mathews, A. Lambai, G. Mohanty, N. Venkataramani, G. Dehm, B.N. Jaya, Effect of stiff substrates on enhancing the fracture resistance of Barium Titanate thin films, Mater. Des. 235 (2023) 112440.
[177] R. Henry, N. Le Roux, I. Zacharie-Aubrun, J.-M. Gatt, C. Langlois, S. Meille, Indentation cracking in mono and polycrystalline cubic zirconia: Methodology of an apparent fracture toughness evaluation, Mater. Sci. Eng. A 860 (2022) 144261.
[178] F. Konstantiniuk, M. Tkadletz, C. Kainz, C. Czettl, N. Schalk, Mechanical properties of single and polycrystalline α-Al2O3 coatings grown by chemical vapor deposition, Surf. Coat. Technol. 410 (2021) 126959.
[179] A. Baptista, F. Silva, J. Porteiro, J. Míguez, G. Pinto, Sputtering physical vapour deposition (PVD) coatings: A critical review on process improvement and market trend demands, Coatings 8(11) (2018) 402.
[180] E. Okotete, A. Muslija, J.K. Hohmann, M. Kohl, S. Brinckmann, S. Lee, C. Kirchlechner, Enhanced crack stability in micro scale fracture testing via optimized bridge notches, Materials Science and Engineering: A 939 (2025) 148479.
[181] J. Delage, E. Saiz, N. Al Nasiri, Fracture behaviour of SiC/SiC ceramic matrix composite at room temperature, J. Eur. Ceram. Soc. 42(7) (2022) 3156-3167.
[182] C. Gilbert, J. Cao, L. De Jonghe, R. Ritchie, Crack‐growth resistance‐curve behavior in silicon carbide: small versus long cracks, J. Am. Ceram. Soc. 80(9) (1997) 2253-2261.
[183] Z. Gao, J. Buchinger, R. Hahn, Z. Chen, Z.L. Zhang, N. Koutná, P.H. Mayrhofer, Bilayer period and ratio dependent structure and mechanical properties of TiN/MoN superlattices, Acta Materialia 279 (2024) 120313.

[184] M. Kuczyk, M. Zawischa, T. Krülle, J. Vollhüter, S. Zeiler, M. Leonhardt, J. Kaspar, O. Zimmer, M. Göken, C. Leyens, M. Zimmermann, In situ mechanical testing of hard yet tough high entropy nitride coatings deposited on compliant steel substrates, Thin Solid Films 787 (2023) 140137.
[185] P. Panjan, M. Čekada, M. Panjan, D. Kek-Merl, Growth defects in PVD hard coatings, Vacuum 84(1) (2009) 209-214.
[186] F. Konstantiniuk, M. Schiester, M. Tkadletz, C. Czettl, N. Schalk, Annealing activated substrate element diffusion and its influence on the microstructure and mechanical properties of CVD TiN/TiCN coatings, Surface and Coatings Technology 488 (2024) 131079.
[187] C. Tian, Y. Ma, A. Ghafarollahi, P. Patil, G. Dehm, E. Bitzek, M. Rasinski, J.P. Best, Segregation-enhanced grain boundary embrittlement of recrystallised tungsten evidenced by site-specific microcantilever fracture, Acta Mater. 259 (2023) 119256.
[188] R. Daniel, M. Meindlhumer, W. Baumegger, J. Todt, J. Zalesak, T. Ziegelwanger, C. Mitterer, J. Keckes, Anisotropy of fracture toughness in nanostructured ceramics controlled by grain boundary design, Mater. Des. 161 (2019) 80-85.
[189] R. Pippan, A. Hohenwarter, The importance of fracture toughness in ultrafine and nanocrystalline bulk materials, Mater. Res. Lett. 4(3) (2016) 127-136.
[190] M.-T. Becker, Synthesis and characterization of B1-AlN containing superlattice structures, Montanuniversitaet Leoben, 2022.
[191] M. Bartosik, D. Holec, D. Apel, M. Klaus, C. Genzel, J. Keckes, M. Arndt, P. Polcik, C.M. Koller, P.H. Mayrhofer, Thermal expansion of Ti-Al-N and Cr-Al-N coatings, Scripta Materialia 127 (2017) 182-185.
[192] W.C. Oliver, G.M. Pharr, An improved technique for determining hardness and elastic modulus using load and displacement sensing indentation experiments, J. Mater. Res. 7(6) (1992) 1564-1583.
[193] Y. Zhang, M. Bartosik, S. Brinckmann, S. Lee, C. Kirchlechner, Toughening nitride hard coatings by deflecting cracks along grain boundaries, Mater. Sci. Eng. A (2025) 148392.
[194] B.N. Jaya, Fracture in small-scale structures and confined volumes, MRS Bulletin 47(8) (2022) 832-838.
[195] Y. Zhang, M. Bartosik, S. Brinckmann, U. Bansal, S. Lee, C. Kirchlechner, Columnar grain boundaries are the weakest link in hard coatings: Insights from micro-cantilever testing with bridge notches, arXiv (2024).
[196] Z. Li, P. Munroe, Z.-t. Jiang, X. Zhao, J. Xu, Z.-f. Zhou, J.-q. Jiang, F. Fang, Z.-h. Xie, Designing superhard, self-toughening CrAlN coatings through grain boundary engineering, Acta Mater. 60(16) (2012) 5735-5744.
[197] M. Wurmshuber, S. Jakob, S. Doppermann, S. Wurster, R. Bodlos, L. Romaner, V. Maier-Kiener, D. Kiener, Tuning mechanical properties of ultrafine-grained tungsten by manipulating grain boundary chemistry, Acta Mater. 232 (2022) 117939.
[198] X. Min, Y. Kimura, T. Kimura, K. Tsuzaki, Delamination toughening assisted by phosphorus in medium-carbon low-alloy steels with ultrafine elongated grain structures, Mater. Sci. Eng. A 649 (2016) 135-145.
[199] L. Hultman, C. Mitterer, Thermal stability of advanced nanostructured wear-resistant coatings, Nanostructured coatings, Springer2006, pp. 464-510.
[200] J. Musil, F. Kunc, H. Zeman, H. Poláková, Relationships between hardness, Young's modulus and elastic recovery in hard nanocomposite coatings, Surf. Coat. Technol. 154(2-3) (2002) 304-313.
[201] J. Buchinger, N. Koutná, Z. Chen, Z. Zhang, P.H. Mayrhofer, D. Holec, M. Bartosik, Toughness enhancement in TiN/WN superlattice thin films, Acta Mater. 172 (2019) 18-29.
[202] M. Bartosik, C. Rumeau, R. Hahn, Z.L. Zhang, P.H. Mayrhofer, Fracture toughness and structural evolution in the TiAlN system upon annealing, Scientific Reports 7(1) (2017).

[203] M. Schlögl, C. Kirchlechner, J. Paulitsch, J. Keckes, P.H. Mayrhofer, Effects of structure and interfaces on fracture toughness of CrN/AlN multilayer coatings, Scr. Mater. 68(12) (2013) 917-920.
[204] E. Okotete, A. Muslija, J.K. Hohmann, M. Kohl, S. Brinckmann, S. Lee, C. Kirchlechner, Enhanced crack stability in micro scale fracture testing via optimized bridge notches, Mater. Sci. Eng. A (2025) 148479.
[205] A.M. Crainic, M. Callisti, A. Van Veelen, A. Michalik, J.A. Milton, M.R. Palmer, R.B. Cook, A comparative study on the physicochemical characteristics of nanoparticles released in vivo from CoCrMo tapers and cement–stem interfaces of total hip replacements, Journal of Biomedical Materials Research Part B: Applied Biomaterials 108(8) (2020) 3311-3322.
[206] Z. Zhang, R. Daniel, C. Mitterer, Atomic and electronic structures of a transition layer at the CrN/Cr interface, J. Appl. Phys. 110(4) (2011).
[207] T.C. Rojas, A. Caro, G. Lozano, J. Sánchez-López, High-temperature solar-selective coatings based on Cr (Al) N. Part 1: Microstructure and optical properties of CrNy and Cr1-xAlxNy films prepared by DC/HiPIMS, Sol. Energy Mater. Sol. Cells 223 (2021) 110951.
[208] T.C. Rojas, S. El Mrabet, S. Domínguez-Meister, M. Brizuela, A. García-Luis, J. Sánchez-López, Chemical and microstructural characterization of (Y or Zr)-doped CrAlN coatings, Surf. Coat. Technol. 211 (2012) 104-110.
[209] C. Mitterbauer, C. Hébert, G. Kothleitner, F. Hofer, P. Schattschneider, H.W. Zandbergen, Electron energy loss-near edge structure as a fingerprint for identifying chromium nitrides, Solid State Commun. 130(3-4) (2004) 209-213.
[210] F.-H. Lu, H.-Y. Chen, C.-H. Hung, Degradation of CrN films at high temperature under controlled atmosphere, Journal of Vacuum Science & Technology A: Vacuum, Surfaces, and Films 21(3) (2003) 671-675.
[211] I. Barin, G. Platzki, Thermochemical data of pure substances, VCh Weinheim1989.
[212] L. Karlsson, Arc evaporated titanium carbonitride coatings, Linköping University, 1999.
[213] M.A. Hopcroft, W.D. Nix, T.W. Kenny, What is the Young's Modulus of Silicon?, Journal of microelectromechanical systems 19(2) (2010) 229-238.
[214] J.-H. Zhao, T. Ryan, P.S. Ho, A.J. McKerrow, W.-Y. Shih, Measurement of elastic modulus, Poisson ratio, and coefficient of thermal expansion of on-wafer submicron films, J. Appl. Phys. 85(9) (1999) 6421-6424.
[215] C. Kittel, P. McEuen, Introduction to solid state physics, John Wiley & Sons2018.
[216] S. Veselkov, O. Samoilova, N. Shaburova, E. Trofimov, High-temperature oxidation of high-entropic alloys: A review, Materials 14(10) (2021) 2595.
[217] N. Biswas, J. Ding, Numerical study of the deformation and fracture behavior of porous Ti6Al4V alloy under static and dynamic loading, International Journal of Impact Engineering 82 (2015) 89-102.
[218] T. Davis, D. Healy, A. Bubeck, R. Walker, Stress concentrations around voids in three dimensions: The roots of failure, Journal of Structural Geology 102 (2017) 193-207.
[219] R.W. Rice, Limitations of pore-stress concentrations on the mechanical properties of porous materials, Journal of Materials Science 32(17) (1997) 4731-4736.